EPFL

Thèse n° 8287

Aqueous electrolytes for high-voltage batteries and supercapacitors

Présentée le 23 juillet 2020

à la Faculté des sciences et techniques de l'ingénieur
Unité de rattachement pour scientifiques IMX
Programme doctoral en science et génie des matériaux

pour l'obtention du grade de Docteur ès Sciences

par

David REBER

Acceptée sur proposition du jury

Prof. P. Hoffmann, président du jury
Prof. F. Nüesch, Dr C. Battaglia, directeurs de thèse
Dr K. Xu, rapporteur
Prof. P. Broekmann, rapporteur
Prof. S. Haussener, rapporteuse

École
polytechnique
fédérale
de Lausanne

2020

Abstract

Lithium-ion batteries are widely implemented as energy storage devices due to their high energy density and low cost. They enabled modern portable electronics and electric vehicles, and are key to manage the integration of intermittent renewable electricity sources, such as solar and wind, into the power grid and decentralized microgrids. The use of flammable organic electrolytes however raises safety concerns, particularly for large-scale stationary batteries. Furthermore, supply chain risks and the use of critical raw materials are a major challenge for the ongoing battery revolution.

Aqueous electrolytes offer promising properties, as they are inherently non-flammable and potentially more cost effective. Combined with electrode materials based on abundant raw materials, aqueous batteries are among the most promising candidates to replace current battery chemistries relying on critical cobalt and flammable organic electrolytes. However, due to the narrow electrochemical stability window of water (practically ca. 1.5 V), aqueous batteries have not yet met the energy density to be serious competitors to current lithium-ion battery technology.

The goal of this thesis was to develop aqueous electrolytes with enhanced electrochemical stability, thus enabling new high-voltage cell chemistries. Exploring aqueous electrolytes with high salt concentrations, so-called water-in-salt electrolytes, we significantly increased the electrochemical stability and developed highly stable 2 V class aqueous sodium-ion batteries. Operating near the solubility limit of the electrolyte salt, crystallization turned out to be a major challenge for water-in-salt electrolytes. In this thesis, we demonstrated that adding highly asymmetric anions into the solution can effectively suppress crystallization, allowing stable operation of saturated electrolytes at temperatures as low as -10 °C. We further examined the impact of anion asymmetry on the local solution structure and dynamics using molecular dynamics simulations, relating the enhanced supercooling to sustained rotational motion of the asymmetric anion.

Further, we demonstrate that the anion has a crucial impact on solution structure and cell performance. We establish that high salt concentration alone does not guarantee high-voltage stability and that due to the limited solubility of most sodium salts new approaches are needed. We provide guidelines for future work and the evaluation of experimental data in order to spur progress in the field of aqueous batteries.

Keywords: Aqueous electrolytes, water-in-salt, anion asymmetry, supercooling, anion-specific effects

Zusammenfassung

Lithium-Ionen-Batterien konnten sich dank ihrer hohen Energiedichte und der tiefen Kosten als gängige Energiespeicher etablieren. Sie ermöglichten den Durchbruch der mobilen Elektronik und elektrischer Autos und sind der Schlüssel zur erfolgreichen Integration von erneuerbaren Energien wie Wind- oder Solarkraft ins Übertragungsnetz und kleinere delokalisierte Netzwerke. Besonders für grosse Installationen aber ist die Nutzung brennbarer organischer Elektrolyte ein Sicherheitsrisiko und die Abhängigkeit von kritischen Rohmaterialien ist eine Herausforderung für die fortlaufende Batterierevolution.

Wässrige Elektrolyte haben vielversprechende Eigenschaften wie Nichtbrennbarkeit und potenziell tiefe Kosten. In Kombination mit häufig vorkommenden Elektrodenmaterialien gehören wässrige Batterien zu den erfolgversprechendsten Kandidaten um momentan gängige Batterien, die auf Kobalt und brennbaren Elektrolyten basieren, abzulösen. Bisher leiden wasser-basierte Batterien aufgrund des kleinen elektrochemischen Stabilitätsfensters wässriger Elektrolyte (in der Praxis ca. 1.5 V) aber unter zu tiefer Energiedichte um mit derzeitigen Batterien zu konkurrieren.

Das Ziel dieser Thesis war die Entwicklung von wässrigen Elektrolyten mit erhöhter elektrochemischer Stabilität um damit Zellchemien mit hoher Spannung zu ermöglichen. Mittels hochkonzentrierter, sogenannter Water-in-Salt Elektrolyte konnten wir die Spannungstoleranz deutlich erhöhen und wässrige Natriumbatterien in der 2 V Klasse entwickeln. Das Auskristallisieren dieser gesättigten Elektrolyte stellte sich als eine der grössten Herausforderungen während dieses Projekts heraus. Mittels asymmetrischer Anionen konnten wir die Kristallisierung unterdrücken und so Batterien bei Temperaturen unter null Grad betreiben. Mittels Molekulardynamik-Simulationen konnten wir das Unterkühlungsverhalten der Elektrolyte mit anhaltender Bewegung der Anionen-Seitenketten erklären.

Für den Einfluss der Anionen auf die Lösungsstruktur konzentrierter Elektrolyte und damit die Stabilität der Batterien konnten wir klare Richtlinien entwickeln. Wir zeigen auf, dass hohe Salzkonzentration nicht zwangsläufig hohe elektrochemische Stabilität garantiert und besprechen Möglichkeiten für weitere Forschungsarbeiten sowie einen Leitfaden zur Auswertung gängiger Experimente.

Stichwörter: Wässrige Elektrolyte, Water-in-Salt, Anionen-Asymmetrie, Unterkühlung, Anionen-spezifische Effekte

Acknowledgments

This thesis was conducted in the Laboratory Materials for Energy Conversion at Empa, the Swiss Federal Laboratories for Materials Science & Technology under the supervision of head of laboratory Dr. Corsin Battaglia. Prof. Frank Nüesch acted as academic supervisor at EPFL in the Department Materials Science and Engineering. I would like to thank them for the opportunity to do this work and their guidance and support over the past four years. I am very grateful to Dr. Corsin Battaglia for the valuable discussions, particularly on how to present and convey my results, and the freedom to explore what seemed interesting at any point. I highly appreciate the opportunities given to me to foster my network at conferences, workshops, and my stay in Tokyo, as well as the chance to take responsibilities for equipment and the battery-testing lab. Further, I am especially grateful to Dr. Ruben-Simon Kühnel who taught me the tricks of the trade and closely advised me. His extensive knowledge about electrochemistry, specifically applied to electrochemical energy storage and electrolytes, has made this thesis possible.

I would like to thank all the team members, Zivis, Bachelor- and Master students at Empa for the good times, with special thanks going to the first generation of 501-PhDs, Léo, Francesco, Marie-Claude, thank you for the warm welcome, and Ryo, Daniel and Max, who were great additions to our crew. We should have gone to Sicily earlier.

Thank you to Prof. Atsuo Yamada for welcoming me in his laboratory at the University of Tokyo, and Dr. Norio Takenaka for teaching me as much as possible in this short time. It was an enriching experience and I greatly enjoyed my stay.

I would also like to thank Prof. Patrik Hoffmann, Dr. Kang Xu, Prof. Sophia Haussener, and Prof. Peter Broekmann for taking the time to review and evaluate my PhD thesis.

Finally, thank you to my friends and family for the great support, especially to my partner in crime Nathalie.

Abbreviations

AC	Activated carbon
BETI	Bis(pentafluoroethanesulfonyl)imide
CE	Counter electrode
CV	Cyclic voltammetry
DSC	Differential scanning calorimetry
ESW	Electrochemical stability window
FSI	Bis(fluorosulfonyl)imide
FTFSI	(fluorosulfonyl)(trifluoromethanesulfonyl)imide
GCPL	Galvanostatic cycling with potential limitations
HCF	Hexacyanoferrate
HER	Hydrogen evolution reaction
LIB	Lithium-ion battery
LSV	Linear sweep voltammetry
MD	Molecular dynamics
NIB	Sodium-ion battery
NMP	*N*-methyl-2-pyrrolidone
NTP	$NaTi_2(PO_4)_3$
NVPOF	$Na_3(VOPO_4)_2F$
OER	Oxygen evolution reaction
OTf	Trifluoromethanesulfonate
PTFSI	(pentafluoroethanesulfonyl)(trifluoromethanesulfonyl)imide
RDF	Radial distribution function
RE	Reference electrode
RT	Room temperature
SEI	Solid-electrolyte interphase
SHE	Standard hydrogen electrode
SS	Stainless steel
TFSI	Bis(trifluoromethanesulfonyl)imide
T_L	Liquidus temperature
WE	Working electrode

Contents

1 Introduction

Over the past decades, global energy consumption has increased rapidly and sustainable electricity generation and storage have become pervasive topics in our daily life. The energy transition, moving away from fossil and nuclear fuels towards renewables, and the electric vehicle revolution, replacing combustion engines in cars with battery-powered electric motors, are among the top issues discussed in politics and media. Quality of life and sustainability go hand in hand with clean, cheap energy, which is summarized in a statement by Nobel Laureate Richard Smalley in his list of top ten problems of humanity for the next 50 years: *In short, energy is the single most important factor that impacts the prosperity of any society*.[1]

With ever-increasing efficiencies and lower cost of renewables, mostly solar and wind, more sustainable sources of energy are installed every year, which is a great step towards independence from fossil fuels. However, the intermittence of renewable sources, i.e. the mismatch between production and demand, remains a major challenge for temporal and spatial balancing of energy supply and consumption. Additional challenges arise from short-term disruptions, e.g. clouds passing over solar farms or fluctuations in wind speed, temporarily reducing the output of renewable-energy power plants. This results in short grid instabilities that have to be compensated to ensure smooth integration of electricity produced by decentralized photovoltaic or wind turbine installations.[2-5]

To date there is not one single technology that can address all timescales of storage that are needed. An overview of some of the most important technologies with their corresponding power and timescales is shown in **Figure 1-1**.[6-8] Peak shifting from noon to nighttime requires large amounts of energy to be stored and released on a timeframe of several hours and is classically provided by pumped hydropower and in recent years also by stationary batteries. Compensating fluctuations in wind speed or cloud coverage requires less energy but a quicker response within several minutes or seconds, often provided by flywheels or compressed air. Here, the fast response time makes up for the low energy density. For seasonal storage, conversion of excess electric power, e.g. from solar production in summer, into chemical fuels like hydrogen and other synthetic fuels is under development. [2-7]

Lithium-ion batteries have emerged as a key technology for portable electronic applications and due to massively improved performance over the past five years are enabling today the widespread deployment of electric vehicles. Due to fast response time, proven reliability, high energy efficiency, and low operating cost, this mature technology also attracted significant interest for grid-scale applications in the timescale of minutes to days.[2-5] For electric vehicles, state-of-the-art lithium-ion batteries provide sufficient energy density and adequate

lifetime and most research efforts now focus on reducing the content of critical raw materials like cobalt, improving their rate capability, and developing next generation solid-state batteries. Additionally, cycle-life, energy density, and safety are continuously being improved.[2, 3, 6-8] Note that high-power batteries with long lifetimes but lower energy density, often based on lithium titanate anodes, are also mature and deployed in e.g. electric busses and ferries. Lead-acid batteries dominate the market for uninterrupted power supplies and starter batteries in cars. However, they are under pressure in Europe as the European Chemicals Agency made recommendations to ban lead oxides used in their production.[9] Further drawbacks are low energy density and the use of corrosive sulfuric acid as electrolyte.[4, 5, 10-13] Flow batteries are another type of battery well positioned for large-scale deployment. Their decoupling of power and energy density allows flexible and scalable layouts but operating costs are high due to the complex plumbing and pumping requirements of flow batteries.[5, 11]

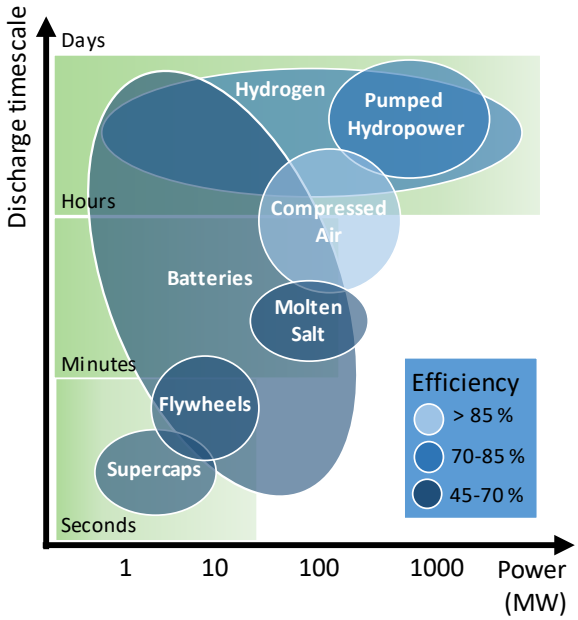

Figure 1-1 Overview of the size (power) and discharge timescales of the most important storage technologies on installed systems level. Note that this is not the specific power density of the individual technologies (e.g. W/kg). Adapted from [6-8]

With lithium-ion battery technology having matured and growing relevance of large-scale stationary battery storage on the market, the supply chain risks and safety issues due to the use of flammable electrolytes become more relevant, and significant research efforts are devoted to developing safer and greener alternatives. Under appropriate conditions, lithium-ion batteries are very safe to operate. However, mechanical abuse (e.g. deformation and road accidents), electrical abuse (e.g. overcharge), and/or thermal abuse (overheating), can lead to Ohmic heating and internal side reactions, mainly due to short circuits. This can result in thermal runaway, the uncontrolled propagation of heat generation, and ignition as the energy stored in the anode and cathode materials is released in an uncontrolled way.[14-16] Besides

the heat and fire hazard, emission of highly toxic gasses, e.g. large amounts of hydrogen fluoride, from ruptured cells is a significant risk, especially in confined spaces, for firefighting personnel.[17]

One approach is to eliminate the flammability of the electrolyte, for example by using aqueous electrolytes. Such batteries are known since the 19th century but suffer from low operating voltages due to the narrow electrochemical stability window of water. This leads to roughly one fifth in energy density compared to state-of-the-art lithium-ion batteries.[18] Consequently, the main motivation of this thesis is the development and theoretical understanding of aqueous electrolytes with improved electrochemical stability. The following chapter gives a brief overview of the current state of battery technology.

1.1 Lithium-ion Batteries

The working principle of a classic lithium-ion battery (LIB) is illustrated in **Figure 1-2**. The cell consists of a cathode, an anode, a separator preventing electrical contact (short circuit) of the electrodes, and the electrolyte. The electrode materials are coated on metallic current collectors, e.g. aluminum or copper foils. Typically, layered transition metal oxides like lithium cobalt oxide, and graphite are employed as the cathode and anode active material respectively. The electrolyte is an organic carbonate mixture in which a fluorinated lithium salt is dissolved. In the battery community, the positive electrode is called the cathode, whereas the negative electrode is termed the anode. Note that, the use of these terms is only correct during discharge of the cell where the cathode is reduced (cations intercalate into the material and e.g. transition metal atoms are reduced by taking up electrons from the external circuit) and the anode is oxidized (cations deintercalate and electrons are given to the external circuit). Electrons flowing through the external circuit then compensate the charge. Upon initial charging, the electrolyte partially decomposes on the anode surface and forms a stable lithium-ion conductive layer called the solid-electrolyte interphase, which prevents further electrolyte decomposition and therefore enhances cycling stability of the full cell. Batteries using this back-and-forth intercalation mechanism are also called rocking-chair batteries and are firmly based on concepts pioneered by Whittingham and further developed by Goodenough.[19, 20] Together with Yoshino, who combined a lithium cobalt oxide cathode with a graphite anode[21] leading to the first commercialization of a lithium-ion battery by Sony, they were awarded the 2019 Nobel Prize in Chemistry for the development of the lithium-ion battery.

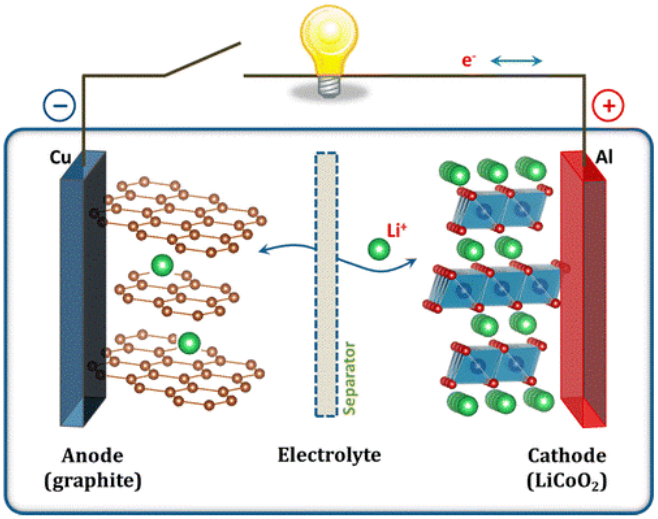

Figure 1-2 Schematic illustration of the archetypal lithium-ion battery based on a graphite anode, organic electrolyte, and an $LiCoO_2$ cathode. Taken from ref. [22]

The high energy density of modern lithium-ion batteries of up to 250 Wh kg^{-1} on the cell level, which translates to a specific capacity of ca. 450 Wh kg^{-1} on the electrode materials level, has enabled the widespread development of portable electronics. The volumetric energy density, particularly important for electric vehicles, of up to 650 Wh L^{-1} on the cell level is also very high. They not only dominate the market for portable electronic devices which use battery packs in the range of 10 to 100 Wh, but are also implemented as the technology of choice for electric vehicles where larger modules up to 100 kWh are needed. In addition, grid-scale stationary storage in the MWh range using LIBs is rapidly developing. Overall, the lithium-ion battery market is projected to grow massively with estimates as high as ca. 250 billion euro by 2025 in Europe alone.[23-25]

The massive increase in battery production over the past years resulted in an astounding decrease in prices on battery pack level, from ca. 1000$ kWh^{-1} in 2010 to less than 200$ kWh^{-1} in 2019. Nevertheless, this also comes with some major challenges. Limited availability of lithium is often considered a major problem for future battery demand, with uneven distribution of raw materials resulting in significant price fluctuations.[26] In fact, the availability of cobalt and natural graphite, both classified as critical raw materials by the European Commission, is a more serious concern. Among other reasons because global reserves are concentrated in few distinct areas. China for example currently provides 49 percent of the global supply of critical raw materials and the Democratic Republic of Congo (DRC) supplies almost 65% of the world's cobalt, often through Chinese intermediaries. This illustrates the link between geopolitics, economy and research.[26-28] In addition, environmental and societal impacts are not to be neglected. Cobalt mining in the DRC is criticized for terrible working conditions and child labor, and mining for lithium in Chile is depleting local groundwater reserves, destroying whole ecosystems.[28] Major consumers of LIBs, such as electric vehicle or mobile

electronics manufacturers, seek to source all their raw material needs from controlled mines but often struggle, stating that they are not able to fully map their supply chain due to its complex nature.[29] In fact, in a recent class action lawsuit, for the first time, several large companies were directly sued for knowingly benefitting from the use of children to mine cobalt in the DRC.[30]

As the projected growth in electric vehicles from ca. 1.2 million cars in 2015 to 965 million in 2050 goes hand in hand with a tremendous increase in mineral needs, also for electricity production (solar, wind), the transition towards a low-carbon future will be a challenge across many industries and supply chains, highlighting the need for alternative battery chemistries.[28] The growing demand of resources for low-carbon technologies is summarized in a statement by the World Bank: *The clean energy transition will be significantly mineral intensive*.[31]

So-called post-lithium chemistries, exploring alternative alkali metals like sodium and potassium or multivalent cations such as aluminum, magnesium, calcium, and zinc, are a very active field of research, promising for example cost effective sodium-ion batteries (NIB).[32-34] Compared to LIBs, NIBs come with a lower energy density, mainly because current sodium cathode materials cannot compete with corresponding high-capacity and high-voltage lithium cathodes.[35] However, their working principle is not drastically different, which should allow easy upscaling of manufacturing with existing infrastructure. Furthermore, many of the best-performing electrodes for NIBs do not rely on cobalt, which is crucial in the rapidly expanding battery market, even though their capacity cannot yet compete with e.g. layered lithium nickel manganese cobalt oxides. In addition, hard carbon, which is cheaper to produce than synthetic graphite but operates at a ca. 300 mV higher potential, can be used in NIBs. A detailed cost analysis showed that, on a materials cost level, replacing lithium with sodium does not have a significant impact on the cost of the battery. The maybe most important feature however is that aluminum instead of copper can be used as a current collector on the anode side, because compared to lithium, sodium does not alloy with aluminum at low potentials.[32-34] In a hypothetical cell, the replacement of copper by aluminum and lithium by sodium results in a total cost reduction of 4.3%, with the current collector exchange having a 2.3 times greater impact than the lithium sodium exchange. However, in case of lithium and cobalt shortages and associated price fluctuations, using sodium can yield reduced supply risks and cost advantages.[26]

For the next five to ten years however, the industry's focus will remain on improving the current lithium-ion technology by reducing the cobalt content of layered oxide cathodes and partial replacement of graphite in the anode by silicon, which has a very high capacity but

suffers from rapid capacity fading upon cycling due to large volume changes. This third generation of LIBs targeting 350 Wh kg^{-1} and 750 Wh L^{-1} on cell level is currently entering the market. The fourth generation is envisioned to rely on solid-state electrolytes and metal anodes or conversion materials, resulting in energy densities of up to 500 Wh kg^{-1} and 1000 Wh L^{-1}.[36, 37]

1.2 Supercapacitors and the Electrochemical Double Layer

In a supercapacitor, schematically shown in **Figure 1-3**, the ions do not intercalate into the electrode but, upon polarization, accumulate on its surface to form an electrochemical double layer. To increase the stored energy by enlarging the surface available for sorption, porous high surface area materials such as activated carbons are most widely used. The very fast nature of this sorption-based storage of charge leads to very high power performance and nearly unlimited cycle life as no chemical reaction that degrades the electrode material is taking place. The energy density however, is much lower than for batteries (on materials level typically below 10 Wh kg^{-1}). Acetonitrile based electrolytes with high ionic conductivities, which is crucial for high power performance, of about 50 mS cm^{-1} are commonly used for supercapacitors. Usually no solid electrolyte interphase is formed.[13, 38-41]

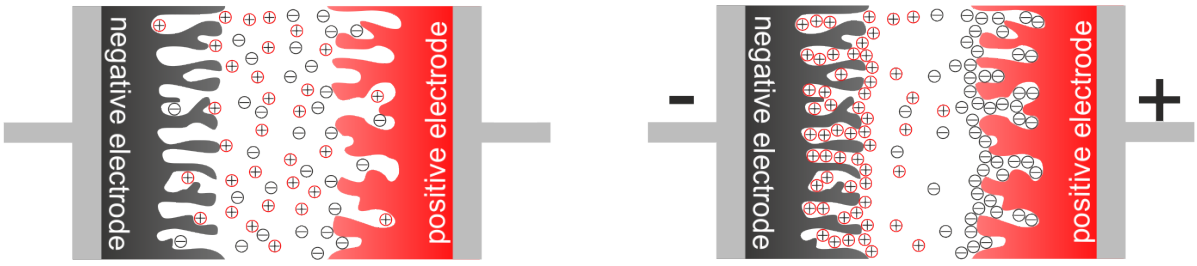

Figure 1-3 Schematic illustration of a typical supercapacitor in the (left) uncharged and (right) charged state using two high surface area porous electrodes.

The electrochemical double layer that is formed on any surface in contact with a fluid was first described by Hermann von Helmholtz who observed that ions are attracted towards the surface of an oppositely charged electrode, thereby forming two correspondingly charged layers at this interface.[42] One is the surface of the electrode itself, the other being the so-called compact layer of counter ions accumulated on the surface. In principle this corresponds to a plate capacitor where charge is stored electrostatically in between the two plates i.e. layers. This model neglected the diffusion of ions or the possibility of adsorption. Gouy and Chapman later introduced a diffuse layer in which the concentration of e.g. cations on the negative electrode decays exponentially with increasing distance from the electrode surface.[43, 44] These models were combined by Stern and complemented with the possibility of specific adsorption of neutral molecules and oriented dipoles by Grahame as illustrated in **Figure 1-4**.[45, 46]

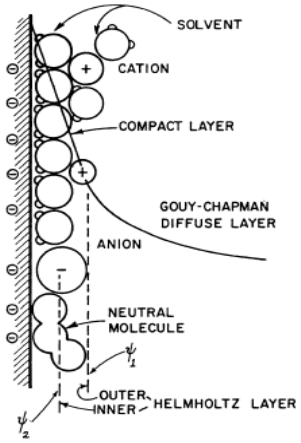

Figure 1-4 Illustration of the double layer forming at a negatively polarized metal electrode. Taken from ref.[39]

The space in between each double layer corresponds to an extremely thin dielectric in a plate capacitor. The capacitance *C* of one electrode can be described by $C = \frac{A\varepsilon}{d}$ where *A* is the electrode area, *ε* the permittivity of the dielectric and *d* the distance between the two plates. Therefore such an electrochemical double layer capacitor, where the separation between the two quasi plates is extremely small (below one nanometer) and the surface area of the electrodes is very high, achieves a much higher capacitance than a classical plate capacitor.[13, 39-41] The energy stored in the double layer *E* is proportional to the cell voltage squared: $E = \frac{1}{2} CV^2$ which highlights the need for highly stable electrolytes that allow high cell voltages without detrimental side reactions such as electrolyte decomposition.[13, 40] In an actual device with two electrodes there is one double layer formed at each electrode resulting in a device that in principle corresponds to two capacitors connected in series. One way of improving the energy density is using pseudocapacitive materials, which are materials that undergo fast, reversible redox reactions that do not involve phase changes of the electrode materials.[39, 40, 47] Another possibility is to add redox active molecules to the electrolyte, which undergo reversible redox reactions after specific adsorption to the electrode surface, thus contributing to the energy density of the device. Here the electrolyte becomes an active participant in the pseudocapacitive charge storage, i.e. an active material. Therefore its weight should be considered when reporting capacitance, or better, due to the battery like character of such a device (charge does not scale proportionally with voltage), capacity.[48]

1.3 Aqueous Electrolytes

Using water as a solvent instead of organic carbonates presents two major advantages: Increased safety and reduced cost. The inherent non-flammability of water significantly reduces the risk of thermal runaway and subsequent ignition of the cell that exists for current LIB technologies. Lower costs are expected due to the fact that no controlled atmosphere (low humidity) is needed during the whole cell production.[49, 50] If combined with abundant materials, for example sodium instead of lithium and cobalt free electrodes, aqueous electrolytes are one of the most promising, cost efficient, and environmentally benign technologies for large-scale battery applications. In addition, aqueous electrolytes typically have high ionic conductivities that improve the fast-charging capabilities of aqueous batteries. This is related to the high dielectric constant of water that efficiently shields the charges of solvated ions, contributing to their high mobility. This conception breaks down at high salt concentrations as discussed in **chapters 1.4**, **2.2**, **3**, and **5**.[51]

So far aqueous batteries only provide rather low energy densities limited by their low operating voltage resulting from the narrow thermodynamic electrochemical stability of 1.23 V of water (at 25 °C).[47] In a battery, energy density scales linearly with voltage and a wide stability window is crucial in order to use high voltage cathode and low voltage anode materials, maximizing the overall cell voltage. To narrow the performance gap between aqueous and organic electrolytes, the stability window of aqueous electrolytes has to be increased by imposing overpotentials for the oxygen and hydrogen evolution reactions.

Outside of the stability window of water, the hydrogen evolution reaction (HER) occurs at low potentials, whereas the oxygen evolution reaction (OER) sets in at high potentials, the corresponding reactions are indicated in **Figure 1-5** along with a Pourbaix diagram giving the electrochemical stability window of pure water as a function of pH. The decomposition of aqueous electrolytes impedes the cell's cycle life and is accompanied by pH changes, which can promote detrimental reactions such as current collector corrosion or active material dissolution from the electrode. Also cell rupture due to the evolving gases can be an issue.[52]

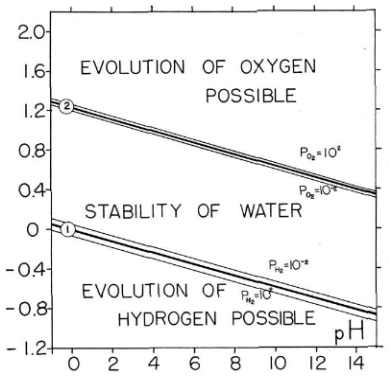

Oxygen evolution reaction (OER)

$2H_2O \leftrightarrow O_2 + 4H^+ + 4e^-$

$4OH^- \leftrightarrow O_2 + 2H_2O + 4e^-$

Hydrogen evolution reaction (HER)

$2H^+ + 2e^- \leftrightarrow H_2$

$2H_2O + 2e^- \leftrightarrow H_2 + 2OH^-$

Figure 1-5 Pourbaix diagram of pure water showing the pH-dependent stability window of 1.23 V[53]. The shift for the HER towards lower potentials with higher pH and higher values for the OER with lower pH, respectively, is indicated by the inclined lines. The corresponding reactions are shown on the right-hand side.

Although the onset potentials for HER and OER can be shifted to a certain degree by varying the pH values according to the Nernst equation (-59 mV per unit of pH at 25 °C, see **Figure 1-5**), the overall window of thermodynamically 1.23 V at 25 °C stays the same. This equation relates the reduction potential of an electrochemical reaction *E* to its standard potential E_0, the temperature *T*, and the activities of the species involved $a_{ox/red}$. *R* is the ideal gas constant, *z* the number of electrons transferred, and *F* the Faraday constant:

$$E = E^0 + \frac{RT}{zF} ln \frac{a_{ox}}{a_{red}} \approx E^0 + \frac{0.059\,V}{z} log \frac{a_{ox}}{a_{red}}$$

The activities can be approximated by the concentration in dilute systems.[53] At low pH, a high concentration of hydronium ions is given, therefore hydrogen evolution can readily take place, as an excess of reagents is available. On the other hand, high pH values, corresponding to high concentration of hydroxide ions, facilitate the oxidation of water.

Using aqueous electrolytes with neutral pH imposes overpotentials for both reactions due to the low concentration of both hydroxide and hydronium ions available in the solution. Following this strategy, apparent stability windows of up to 1.6 V have been reported on activated carbon electrodes.[54-56] The stability window was extended further by using two separate electrolytes with different pH values for the two electrodes. 6M KOH (pH=14) was employed on the negative electrode, therefore pushing HER towards lower potentials, whereas 1M H_2SO_4 (pH=0) was used on the positive side, imposing a large overpotential for the OER. This enabled an electrochemical stability window of 2.1 V. However the quite costly assembly of the cells due to the need of an ion-selective membrane was highlighted as a major drawback of such a system.[57]

There have been numerous further approaches to increase the stability of aqueous electrolytes. The use of buffered solutions is one approach to address local pH changes occurring right next to the electrode surface. This is also beneficial as pH-dependent dissolution of active

material can be limited. Manganese dioxide for example has shown superior performance in phosphate-, carbonate-, and borate-buffered electrolytes where, in addition to the pH buffering, protective phosphate, carbonate, or borate layers are formed that improve cycling stability.[58] The addition of propane-1,3-disulfonate to a phosphate-buffered solution reportedly allowed the operation of a high voltage $LiNi_{0.5}Mn_{1.5}O_4$ cathode (>4.5 V vs. Li^+/Li) in aqueous electrolyte.[59, 60] The increased oxidative stability of the electrolyte is explained by accumulation of the bulky anions on the surface of the positive electrode with increasing potential, thus hindering water molecules from accessing the oxidative surface. However, the reported stability can be questioned, as after only five cycles the system already fails.[59, 60] In organic media this accumulation was also reported to be the case for other bulky anions like TFSI or PF_6.[61] In a similar approach sodium dodecyl sulfate (SDS) has been shown to impose overpotentials on both HER and OER. SDS is adsorbed on the surface of the electrodes with its charged hydrophilic group facing the electrode and its hydrophobic tail facing the bulk electrolyte, therefore hampering the access of water molecules to the electrode surface. Overall a $Na_2MnFe(CN)_6$ cathode was much more stable in such a modified electrolyte.[62] Also *n*-alkanethiols as additives have proven to reduce the rate of hydrogen evolution by formation of rather compact monolayers on the electrode surface.[63, 64] Another example of a surface blocker is succinic acid on zinc oxide electrodes where HER is suppressed. Dendrite formation on zinc anodes was also found to be reduced.[65] An important factor to keep in mind is the catalytic activity of the electrode material towards HER or OER. Lead for example is a poor catalyst for HER and OER, which enables stable operation of 2 V lead-acid batteries. Therefore, the poor catalytic activity of zinc towards HER may have contributed to the apparent HER suppression.[66, 67]

1.4 Highly Concentrated Aqueous Electrolytes

Another strategy to increase the electrochemical stability window is the use of highly concentrated electrolytes using highly soluble perfluorinated sulfonimides. An aqueous 21m (moles of salt per kilogram of solvent) lithium bis(trifluoromethanesulfonyl)imide (LiTFSI) electrolyte was reported in 2015 and demonstrated an apparent stability window of ca. 3 V while retaining an ionic conductivity comparable to organic electrolytes (ca. 10 mS cm^{-1}).[68] This system was designated “water-in-salt”, as at such concentrations the salt outnumbers the water by weight and volume. At a concentration of 21m, the 2.6 water molecules per cation cannot sufficiently shield its formal charge anymore, leading to the incorporation of TFSI anions into the primary solvation sheath, as illustrated in **Figure 1-6**. The water molecules are trapped in the solvation shell of the cations and very little free water molecules are left in the bulk of

the solution. This makes it less likely for them to reach the electrodes to undergo electrolysis, imposing kinetic overpotentials towards HER and OER.

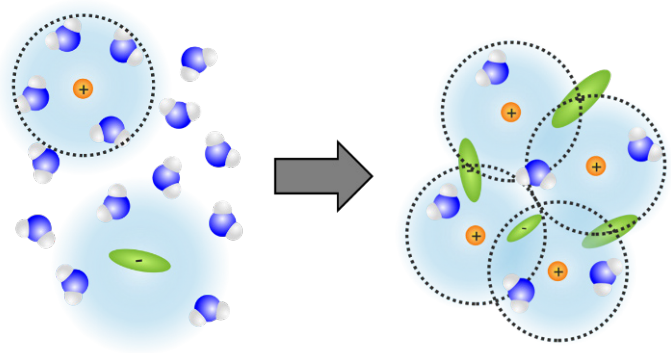

Figure 1-6 Schematic illustration of the change in solution structure from a dilute to a highly concentrated electrolyte.

In addition, the resulting high probability of TFSI at the anode surface, brought along by the anion-solvated cations, leads to an interphasial chemistry dominated by the reduction of the anion. Additionally, the strong interaction with cations stabilizes the transferred electron during reduction, therefore reducing the reductive stability of TFSI. This leads to premature decomposition of Li_2(TFSI) aggregates before water hydrolysis which in turn results in the formation of a mainly anion derived solid-electrolyte interphase (SEI) at the anode.[68-71]

An alternative pathway for SEI formation involving hydroxide catalyzed reduction of the anions was suggested in 2018.[72] The SEI acts as an electron barrier that prevents further water reduction, while allowing lithium ions to migrate to the electrode. In combination with the reduced activity of water and additional kinetic stabilization due to water exclusion from the interfacial layer at the positive electrode, this electrolyte allowed stable cycling of a 2.3 V aqueous LIB.[68, 69] Further studies revealed that the SEI mainly consists of LiF generated from reduction/decomposition of fluorine-rich TFSI, but also Li_2O and Li_2CO_3 originating from the reduction of dissolved oxygen and CO_2.[73] LiF formation is facilitated by the preferential adsorption of CF_3-groups of TFSI at the negative electrode surface.**[69]** The necessity for continuous presence of the highly concentrated electrolyte was demonstrated by cycling an electrode with preformed SEI in a dilute electrolyte. The increased solubility of SEI constituents in the dilute electrolyte led to dissolution and pronounced water reduction.[73] As a result, a stable SEI cannot form at low concentrations as the adhesion of possible anion decomposition products is prevented by hydrogen gas bubble formation.[73] Furthermore, it was shown that the formation of a stable SEI depends on the catalytic activity towards HER of the electrode materials.[70]

Similar to highly concentrated organic electrolytes[61, 74], we also demonstrated reduced anodic dissolution of aluminum current collectors in the 21m LiTFSI electrolyte.[75] Later, two

ca. 28m aqueous lithium electrolytes based on LiTFSI and lithium bis(pentafluoroethanesulfonyl)imide LiBETI ("hydrate-melt")[76], or LiTFSI and lithium trifluoromethanesulfonate (LiOTf) ("water-in-bisalt")[77], respectively, were reported, both showing further improvement in terms of electrochemical stability and full cell cycling performance of high-voltage cells. Recently, concentrations above 30m up to 55m have been achieved.[78, 79] However, only limited improvement of reductive stability is observed when increasing the concentration above 21m. This can in part be explained by water-rich nanodomains at the electrode surface that are formed at strongly-negative potentials.[69] On the positive electrode, water oxidation is hindered by the high concentration of bulky anions and thus water exclusion from the electrode surface.[69] It was shown by differential electrochemical mass spectrometry that already for 21m LiTFSI the oxygen evolution is almost completely suppressed.[73]

The hydrate-melt system allowed operating a 3 V battery employing commercial $Li_4Ti_5O_{12}$ as an anode and $LiNi_{0.5}Mn_{1.5}O_4$ as a cathode at rather high rates which promote stability.[76] Further reports on such highly concentrated electrolytes propose the $LiMn_2O_4/Mo_6S_8$ (2.3 V)[68], $LiMn_2O_4/TiO_2$ (2.5 V)[77], $LiFePO_4/Mo_6S_8$ (1.6 V, highlighting low cost and safety)[80], or $LiMn_{0.8}Fe_{0.2}PO_4$/Zn (1.8 V)[81] couples. Often maximum cell voltages are highlighted, but the average discharge voltages are generally significantly lower. For the $LiMn_2O_4/TiO_2$ couple for example, the average discharge potential is 2.1 V.

Adding a highly-fluorinated ether to a water-in-salt electrolyte as a sacrificial additive allowed formation of a dense SEI in the first charging cycle on both graphite and lithium, opening the path towards 4 V aqueous lithium-ion batteries.[82] Mixing a highly concentrated aqueous electrolyte with dimethyl carbonate or acetonitrile combined the advantages of both aqueous and organic electrolytes.[83, 84] The aqueous portion introduced high safety, whereas the presence of an organic solvent improved the SEI quality, thus increasing the electrochemical stability of the system.

The main drawback of the described highly concentrated electrolytes is the still narrow electrochemical stability window, leading to a low energy density for cells based on water-in-salt electrolytes. Further issues are the high material cost due to the large amounts of salts needed, high density of the electrolyte, and ionic conductivities below 10 mS cm^{-1} at room temperature due to pronounced ion pairing and agglomeration, which limits the power performance. Note that the electrolyte in a state-of-the-art cell only accounts for ca. 13% of the cells weight and 10% of its volume (excl. casing).[85] Therefore, the high density of water-in-salt electrolytes (> 1.7 g/cm^3 vs. ~1.3 g/cm^3 for a standard organic electrolyte) has a marginal impact on the overall cell density and is not such a critical issue.

1.5 Aim of the Thesis

Aqueous electrolytes are inherently non-flammable, which alleviates concerns about thermal runaway and ignition of batteries. Combined with abundant materials, such as sodium instead of lithium, and iron or manganese instead of cobalt, novel aqueous batteries are among the most promising candidates to replace e.g. highly toxic and corrosive lead-acid chemistries and lithium-ion batteries in certain applications. However, the narrow electrochemical stability window of water has so far stood in the way of safe and highly energy-dense high-voltage aqueous batteries. Therefore, water electrolysis has to be suppressed, which was previously achieved by catalytically inactive electrode coatings or variations of the pH of the electrolyte. In this thesis, we aspired to manipulate not only the electrode-electrolyte interface but also the water molecules themselves. Using highly concentrated solutions of carefully selected salts, we immobilize most water molecules in the solvation shell of the cation and generate anion-rich interfaces at the electrode surfaces. The reduced mobility of water and the anion-dominated interfacial chemistry impose kinetic overpotentials towards water decomposition and enable the formation of a protective solid-electrolyte interphase, resulting in higher electrochemical stability. Eventually, we were able to implement some of the highest-voltage cathode materials into 2 V class aqueous sodium-ion batteries.

Limiting the applicability of such saturated electrolytes, crystallization turned out to be a major challenge during this project. Studying the solution structure and coordination environment of ions in saturated electrolytes containing asymmetric anions, we discovered that sustained local motion of such asymmetric molecules can enhance supercooling, thereby significantly improving the low temperature performance of our batteries.

Although the water-cation interaction seems most important in these electrolytes, we noticed that at high concentrations also the anion becomes critically relevant as it influences the solution structure, distribution of water, and formation of protective interphases. Therefore, we derived guidelines for anion-suitability in water-in-salt electrolytes.

Overall, this thesis focuses on the development and improved understanding of highly concentrated aqueous electrolytes and their implementation into high-performance, lab-scale prototype batteries. The structure of the thesis is outlined below as a guide to the reader.

Chapter 2 briefly summarizes the most important methods and techniques used in this thesis. Preparation of aqueous electrolytes and characterization methods are described, followed by a short explanation of the electrochemical techniques employed in this thesis as well as the principles of classical molecular dynamics simulations.

In **chapter 3**, we examine the influence of the alkali cation on key physicochemical properties of water-in-salt electrolytes, recognize the low solubility of suitable sodium salts, and

scrutinize a protocol to determine the electrochemical stability window on high surface area electrodes. We then develop a 1.8 V supercapacitor based on a saturated 8m NaTFSI aqueous electrolyte.

The limited solubility, and eventually lower electrochemical stability, of aqueous sodium electrolytes compared to lithium-based systems is addressed in **chapter 4**. We identify NaFSI as a promising salt for water-in-salt electrolytes due to its very high solubility and report a stability window of ca. 2.6 V for a saturated solution.

In **chapter 5**, we discuss the susceptibility of the FSI anion towards hydrolysis. We find that the kinetics of the anion decomposition are highly cation- and concentration-dependent and report increased chemical stability for NaFSI based aqueous electrolytes compared to LiFSI analogues.

In **chapter 6**, we show that a key factor limiting the applicability of water-in-salt electrolytes is their tendency to crystallize near room temperature, leading to cell failure. We report the use of asymmetric FTFSI anions as solution to suppress the crystallization of NaFSI based aqueous electrolytes and demonstrate this approach with a 2 V class aqueous sodium-ion battery with excellent cycling stability from -10 to 30 °C.

The suppressed crystallization of electrolytes based on the asymmetric FTFSI anion is examined in **chapter 7**. Based on classical molecular dynamics simulations and Raman spectroscopy, we hypothesize that different anion-cation coordination geometries and subsequent intramolecular bond rotations lie at the heart of the phenomenon.

In **Chapter 8**, we demonstrate the effects different anions have on solution structure and develop guidelines for anion-suitability in water-in-salt electrolytes. We show that high salt concentration alone does not guarantee desirable performance and lay out the challenges for purely aqueous sodium-ion batteries and discuss several promising alternative approaches.

Chapter 9 provides a perspective on the electrochemical stability of water-in-salt electrolytes and highlights the disconnect between reported and practical values. We discuss parameters that influence the measurement of stability windows and provide some guidelines for future work.

Finally, **chapter 10** concludes this thesis and provides an outlook for future work on aqueous batteries.

References

1. Smalley, R.E., *Future global energy prosperity: the terawatt challenge.* Mrs Bulletin, 2005. **30**(6): p. 412-417.
2. Tarascon, J.-M. and M. Armand, *Issues and challenges facing rechargeable lithium batteries.* Nature, 2001. **414**(6861): p. 359-367.
3. Dunn, B., H. Kamath, and J.-M. Tarascon, *Electrical energy storage for the grid: a battery of choices.* Science, 2011. **334**(6058): p. 928-935.
4. Posada, J.O.G., et al., *Aqueous batteries as grid scale energy storage solutions.* Renewable and Sustainable Energy Reviews, 2017. **68**: p. 1174-1182.
5. Yang, Z., et al., *Electrochemical energy storage for green grid.* Chemical reviews, 2011. **111**(5): p. 3577-3613.
6. Akhil, A.A., et al., *DOE/EPRI electricity storage handbook in collaboration with NRECA.* Sandia National Laboratories, 2015.
7. Mooney, D., *Large-Scale Energy Storage* Stanford University Global Climate & Energy Project Tutorial Series, 2015.
8. *Electricity Storage FactBook.* SBC Energy Institute, 2013.
9. *Recommendation of the European Chemicals Agency for the inclusion of substances in Annex XIV to REACH.*
10. Leadbetter, J. and L.G. Swan, *Selection of battery technology to support grid-integrated renewable electricity.* Journal of Power Sources, 2012. **216**: p. 376-386.
11. Soloveichik, G.L., *Battery technologies for large-scale stationary energy storage.* Annual review of chemical and biomolecular engineering, 2011. **2**: p. 503-527.
12. May, G.J., A. Davidson, and B. Monahov, *Lead batteries for utility energy storage: A review.* Journal of Energy Storage, 2018. **15**: p. 145-157.
13. Winter, M. and R.J. Brodd, *What Are Batteries, Fuel Cells, and Supercapacitors?* Chemical Reviews, 2004. **104**(10): p. 4245-4270.
14. Wang, Q., et al., *Thermal runaway caused fire and explosion of lithium ion battery.* Journal of power sources, 2012. **208**: p. 210-224.
15. Feng, X., et al., *Thermal runaway mechanism of lithium ion battery for electric vehicles: A review.* Energy Storage Materials, 2018. **10**: p. 246-267.
16. Wen, J., Y. Yu, and C. Chen, *A review on lithium-ion batteries safety issues: existing problems and possible solutions.* Materials express, 2012. **2**(3): p. 197-212.
17. Larsson, F., et al., *Toxic fluoride gas emissions from lithium-ion battery fires.* Scientific reports, 2017. **7**(1): p. 1-13.
18. Beck, F. and P. Rüetschi, *Rechargeable batteries with aqueous electrolytes.* Electrochimica Acta, 2000. **45**(15-16): p. 2467-2482.
19. Whittingham, M.S., *Electrical energy storage and intercalation chemistry.* Science, 1976. **192**(4244): p. 1126-1127.
20. Mizushima, K., et al., *LixCoO2 (0< x<-1): A new cathode material for batteries of high energy density.* Materials Research Bulletin, 1980. **15**(6): p. 783-789.
21. Yoshino, A., K. Sanechika, and T. Nakajima, *Secondary battery*. 1987, Google Patents.

22. Goodenough, J.B. and K.-S. Park, *The Li-ion rechargeable battery: a perspective.* Journal of the American Chemical Society, 2013. **135**(4): p. 1167-1176.

23. Placke, T., et al., *Lithium ion, lithium metal, and alternative rechargeable battery technologies: the odyssey for high energy density.* Journal of Solid State Electrochemistry, 2017. **21**(7): p. 1939-1964.

24. Pillot, C. *The rechargeable battery market and main trends 2014–2025*. in *31st International Battery Seminar & Exhibit*. 2015.

25. Šefčovič, M., *Speech at the Industry Days Forum on the Industry-led initiative on batteries / the EU Battery Alliance.*

26. Vaalma, C., et al., *A cost and resource analysis of sodium-ion batteries.* Nature Reviews Materials, 2018. **3**(4): p. 1-11.

27. Commission, E., *Report on Critical Raw materials for the EU.* Retrieved April, 2014. **30**: p. 2015.

28. Sovacool, B.K., et al., *Sustainable minerals and metals for a low-carbon future.* Science, 2020. **367**(6473): p. 30-33.

29. CNN. *Cobalt - Dirty Energy*. 2018; Available from: https://edition.cnn.com/interactive/2018/05/africa/congo-cobalt-dirty-energy-intl/.

30. International-Rights-Advocates. *Cobalt DRC Case*. 2020; Available from: http://www.iradvocates.org/sites/iradvocates.org/files/12.16.19%20FINAL%20Cobalt%20Complaint.pdf.

31. World-Bank. *Climate-Smart Mining: Minerals for Climate Action*. 2018; Available from: https://www.worldbank.org/en/topic/extractiveindustries/brief/climate-smart-mining-minerals-for-climate-action.

32. Slater, M.D., et al., *Sodium-ion batteries.* Advanced Functional Materials, 2013. **23**(8): p. 947-958.

33. Kundu, D., et al., *The emerging chemistry of sodium ion batteries for electrochemical energy storage.* Angewandte Chemie International Edition, 2015. **54**(11): p. 3431-3448.

34. Choi, J.W. and D. Aurbach, *Promise and reality of post-lithium-ion batteries with high energy densities.* Nature Reviews Materials, 2016. **1**(4): p. 1-16.

35. Schneider, S.F., et al., *A modeling framework to assess specific energy, costs and environmental impacts of Li-ion and Na-ion batteries.* Sustainable Energy & Fuels, 2019. **3**(11): p. 3061-3070.

36. Elektromobilität, N.P., *Roadmap integrierte Zell-und Batterieproduktion Deutschland.* Herausgeber: Gemeinsame Geschäftsstelle Elektromobilität der Bundesregierung (GGEMO). Berlin: GGEMO, 2016.

37. Steen, M., et al., *EU competitiveness in advanced Li-ion batteries for E-mobility and stationary storage applications–opportunities and actions.* JRC Science for Policy Report 2017.

38. F. Béguin, E.F., *(eds): Supercapacitors–Materials, Systems, and Applications*. 2015, Springer.

39. Conway, B.E., *Electrochemical supercapacitors: scientific fundamentals and technological applications*. 2013: Springer Science & Business Media.

40. Simon, P. and Y. Gogotsi, *Materials for electrochemical capacitors.* Nature materials, 2008. **7**(11): p. 845-854.

41. Béguin, F., et al., *Carbons and electrolytes for advanced supercapacitors.* Adv Mater, 2014. **26**(14): p. 2219-51, 2283.

42. Helmholtz, H.v., *Ueber einige Gesetze der Vertheilung elektrischer Ströme in körperlichen Leitern mit Anwendung auf die thierisch-elektrischen Versuche.* Annalen der Physik, 1853. **165**(6): p. 211-233.

43. Gouy, M., *Sur la constitution de la charge électrique à la surface d'un électrolyte.* J. Phys. Theor. Appl., 1910. **9**(1): p. 457-468.

44. Chapman, D.L., *LI. A contribution to the theory of electrocapillarity.* The London, Edinburgh, and Dublin philosophical magazine and journal of science, 1913. **25**(148): p. 475-481.

45. Stern, O., *Zur theorie der elektrolytischen doppelschicht.* Berichte der Bunsengesellschaft für physikalische Chemie, 1924. **30**(21-22): p. 508-516.

46. Grahame, D.C., *The electrical double layer and the theory of electrocapillarity.* Chemical reviews, 1947. **41**(3): p. 441-501.

47. Conway, B. and W. Pell, *Double-layer and pseudocapacitance types of electrochemical capacitors and their applications to the development of hybrid devices.* Journal of Solid State Electrochemistry, 2003. **7**(9): p. 637-644.

48. Balducci, A., et al., *Perspective—a guideline for reporting performance metrics with electrochemical capacitors: from electrode materials to full devices.* Journal of The Electrochemical Society, 2017. **164**(7): p. A1487-A1488.

49. Ahmed, S., P.A. Nelson, and D.W. Dees, *Study of a dry room in a battery manufacturing plant using a process model.* Journal of Power Sources, 2016. **326**: p. 490-497.

50. Chu, S., Y. Cui, and N. Liu, *The path towards sustainable energy.* Nature Materials, 2017. **16**(1): p. 16-22.

51. Gavish, N. and K. Promislow, *Dependence of the dielectric constant of electrolyte solutions on ionic concentration: A microfield approach.* Physical review E, 2016. **94**(1): p. 012611.

52. Zhong, C., et al., *A review of electrolyte materials and compositions for electrochemical supercapacitors.* Chem Soc Rev, 2015. **44**(21): p. 7484-539.

53. Delahay, P., M. Pourbaix, and P. Van Rysselberghe, *Potential-pH diagrams.* J. chem. Educ, 1950. **27**(12): p. 683.

54. Abbas, Q. and F. Béguin, *High voltage AC/AC electrochemical capacitor operating at low temperature in salt aqueous electrolyte.* Journal of Power Sources, 2016. **318**: p. 235-241.

55. Abbas, Q., et al., *Strategies to Improve the Performance of Carbon/Carbon Capacitors in Salt Aqueous Electrolytes.* Journal of the Electrochemical Society, 2015. **162**(5): p. A5148-A5157.

56. Abbas, Q., et al., *Sustainable AC/AC hybrid electrochemical capacitors in aqueous electrolyte approaching the performance of organic systems.* Journal of Power Sources, 2016. **326**: p. 652-659.

57. Fic, K., et al., *Around the thermodynamic limitations of supercapacitors operating in aqueous electrolytes.* Electrochimica Acta, 2016. **206**: p. 496-503.

58. Komaba, S., et al., *Efficient Electrolyte Additives of Phosphate, Carbonate, and Borate to Improve Redox Capacitor Performance of Manganese Oxide Electrodes.* Journal of the Electrochemical Society, 2013. **160**(11): p. A1952-A1961.

59. Miyazaki, K., et al., *Enhanced resistance to oxidative decomposition of aqueous electrolytes for aqueous lithium-ion batteries.* Chem Commun (Camb), 2016. **52**(28): p. 4979-82.

60. Vatamanu, J., et al., *Molecular dynamics simulation study of the interfacial structure and differential capacitance of alkylimidazolium bis (trifluoromethanesulfonyl) imide [C n mim][TFSI] ionic liquids at graphite electrodes.* The Journal of Physical Chemistry C, 2012. **116**(14): p. 7940-7951.

61. McOwen, D.W., et al., *Concentrated electrolytes: decrypting electrolyte properties and reassessing Al corrosion mechanisms.* Energy & Environmental Science, 2014. **7**(1): p. 416-426.

62. Hou, Z., et al., *Surfactant widens the electrochemical window of an aqueous electrolyte for better rechargeable aqueous sodium/zinc battery.* Journal of Materials Chemistry A, 2017. **5**(2): p. 730-738.

63. Malkhandi, S., et al., *Self-assembled monolayers of n-alkanethiols suppress hydrogen evolution and increase the efficiency of rechargeable iron battery electrodes.* J Am Chem Soc, 2013. **135**(1): p. 347-53.

64. Yang, B., et al., *Organo-sulfur molecules enable iron-based battery electrodes to meet the challenges of large-scale electrical energy storage.* Energy & Environmental Science, 2014. **7**(8): p. 2753.

65. Lee, C.W., et al. *Studies on suppression of hydrogen evolution reaction for zinc/air fuel cell*. in *Materials science forum*. 2007. Trans Tech Publ.

66. Trasatti, S., *Work function, electronegativity, and electrochemical behaviour of metals: III. Electrolytic hydrogen evolution in acid solutions.* Journal of Electroanalytical Chemistry and Interfacial Electrochemistry, 1972. **39**(1): p. 163-184.

67. Roger, I., M.A. Shipman, and M.D. Symes, *Earth-abundant catalysts for electrochemical and photoelectrochemical water splitting.* Nature Reviews Chemistry, 2017. **1**: p. 0003.

68. Suo, L., et al., *"Water-in-salt" electrolyte enables high-voltage aqueous lithium-ion chemistries.* Science, 2015. **350**(6263): p. 938-43.

69. Vatamanu, J. and O. Borodin, *Ramifications of water-in-salt interfacial structure at charged electrodes for electrolyte electrochemical stability.* J. Phys. Chem. Lett., 2017. **8**(18): p. 4362-4367.

70. Ko, S., Y. Yamada, and A. Yamada, *Formation of a Solid Electrolyte Interphase in Hydrate-Melt Electrolytes.* ACS applied materials & interfaces, 2019. **11**(49): p. 45554-45560.

71. Miyazaki, K., et al., *First-Principles Study on the Peculiar Water Environment in a Hydrate-Melt Electrolyte.* The journal of physical chemistry letters, 2019. **10**(20): p. 6301-6305.

72. Dubouis, N., et al., *The role of the hydrogen evolution reaction in the solid–electrolyte interphase formation mechanism for "Water-in-Salt" electrolytes.* Energy & Environmental Science, 2018.

73. Suo, L., et al., *How solid-electrolyte interphase forms in aqueous electrolytes.* J. Am. Chem. Soc., 2017. **139**(51): p. 18670-18680.

74. Yamada, Y., et al., *Corrosion Prevention Mechanism of Aluminum Metal in Superconcentrated Electrolytes.* ChemElectroChem, 2015. **2**(11): p. 1687-1694.

75. Kühnel, R.-S., et al., *"Water-in-salt" electrolytes enable the use of cost-effective aluminum current collectors for aqueous high-voltage batteries.* Chem Commun (Camb), 2016. **52**(68): p. 10435-8.

76. Yamada, Y., et al., *Hydrate-melt electrolytes for high-energy-density aqueous batteries.* Nat. Energy, 2016. **1**: p. 16129.

77. Suo, L., et al., *Advanced High-Voltage Aqueous Lithium-Ion Battery Enabled by "Water-in-Bisalt" Electrolyte.* Angew. Chem., 2016. **55**(25): p. 7136-41.

78. Ko, S., et al., *Lithium-salt monohydrate melt: A stable electrolyte for aqueous lithium-ion batteries.* Electrochemistry Communications, 2019. **104**: p. 106488.

79. Forero-Saboya, J., et al., *Water-in-Bisalt Electrolyte with Record Salt Concentration and Widened Electrochemical Stability Window.* The journal of physical chemistry letters, 2019. **10**(17): p. 4942-4946.

80. Suo, L., et al., *"Water-in-Salt" electrolytes enable green and safe Li-ion batteries for large scale electric energy storage applications.* J. Mater. Chem. A., 2016. **4**(17): p. 6639-6644.

81. Zhao, J., et al., *High-voltage Zn/LiMn0.8Fe0.2PO4 aqueous rechargeable battery by virtue of "water-in-salt" electrolyte.* Electrochemistry Communications, 2016. **69**: p. 6-10.

82. Yang, C., et al., *4.0 V Aqueous Li-Ion Batteries.* Joule, 2017. **1**(1): p. 122-132.

83. Wang, F., et al., *Hybrid aqueous/non-aqueous electrolyte for safe and high-energy Li-ion batteries.* Joule, 2018. **2**(5): p. 927-937.

84. Chen, J., et al., *Improving Electrochemical Stability and Low-Temperature Performance with Water/Acetonitrile Hybrid Electrolytes.* Advanced Energy Materials, 2020. **10**(3): p. 1902654.

85. Betz, J., et al., *Theoretical versus practical energy: a plea for more transparency in the energy calculation of different rechargeable battery systems.* Advanced Energy Materials, 2019. **9**(6): p. 1803170.

2 Methods

The principles of the experimental and theoretical techniques used in this thesis are described in this chapter. Technical details such as the type of instrument used or exact experimental parameters are provided in detail in the corresponding articles, see **chapters 3-9**. For practical reasons, molality (mol of solute per kilogram of solvent) instead of molarity (mol of solute per liter of final solution) is used to measure the concentration of the electrolytes in this thesis. This leads to concentrations that may seem very high to readers not used to the concept of molality.

2.1 Electrochemical Measurements

2.1.1 Voltammetric Methods

Voltammetry is an electroanalytical method where, in two-electrode setup or full-cell, a potential is applied or scanned between a working electrode (WE) and a counter electrode (CE) that compensates the charge of any reactions taking place at the WE in order to maintain charge neutrality. The resulting current is then measured. In a three-electrode setup or half-cell, the potential is controlled between the working electrode and a reference electrode (RE) with a well-defined potential and ideally no resistance. In aqueous environments silver/silver-chloride, used in this thesis, and calomel references are very common, whereas in organic electrolytes most references have solvent-dependent potentials.[1] Although not perfect, due to polarizability, lithium and sodium metal disks are commonly employed as a reference in the battery community.[2] This allows comparison of materials over different systems, i.e. versus different references. An example is the potential of a battery electrode material versus sodium metal in an organic electrolyte or versus a silver-silver chloride RE in an aqueous electrolyte. In this thesis, the counter electrode typically consisted of a large lithium or sodium disk for measurements in organic electrolytes, or a thick activated carbon pellet with high capacitance. A pellet with a capacitance of 36 Farad for example can compensate one milliampere hour per centimeter square of charge while only moving 100 mV. The goal is to keep the potential of the counter electrode nearly constant, so one can exclude reactions at the CE from influencing the WE under study.

In linear sweep voltammetry (LSV) the voltage is altered up or down to a cutoff potential at a constant scan rate. In this thesis and throughout literature, this method is used to estimate the electrochemical stability windows of electrolytes: As long as the electrolyte is stable, no reactions take place and only very small currents from double layer capacitance (small due

to small surface area of the flat usually metallic electrodes) are measured. As soon as decomposition reactions start to take place, the current increases often exponentially with increasing potential according to the Butler-Volmer equation. A current cut-off is then usually chosen to define the stability limits. The stability window itself represents the voltage range within which the operating potentials of electrode materials have to lie. Reported stability windows in literature tend to be massively overstated and there is certain disconnect between practical and reported stability windows. Furthermore, the surface area and catalytic properties of the substrate towards water decomposition reactions have a significant influence on the resulting stability window. This issue is discussed in detail in **chapters 3** and **9**. Generally speaking, substrates and scan rates (slow) relevant to the target application should be used.

In addition, cyclic voltammetry (CV) is a commonly employed method to define the stability limits. Here the potential is scanned back and forth for many cycles. The application of CV to the stability window measurement is discussed in detail in **chapter 3**. CV is also a crucial tool to characterize the activity of battery electrode materials and rapidly provides information on the redox potential of electroactive species and reversibility of a reaction.

2.1.2 Galvanostatic Methods

Complementary to voltammetry, galvanostatic methods are used to study the voltage response of a system to an applied constant current. The most common application, galvanostatic cycling with potential limitations (GCPL), is used to characterize the charge/discharge behavior of a battery within a certain potential window. A constant current is applied to charge the battery to a predefined cut-off voltage, and then a current of opposite sign is drawn to discharge the cell. This corresponds to a typical charge-discharge cycle and is repeated hundreds of times to study the cycle life and potential evolution over time of a device. The voltage response is characteristic of the studied electrode materials. Practical cell voltages often deviate from theoretical considerations due to resistances, called overpotentials or polarizations, related to the various processes occurring in the cell during operation. The activation overpotential (η_{act}), concentration overpotential (η_{conc}), and ohmic losses (η_{ohm}) typically make up the cells internal resistance. η_{act} is related to the charge transfer kinetics of a reaction and its associated resistances at the solid-electrolyte interface (e.g. surface area). η_{conc} is related to mass transfer limitations and depends on diffusional properties of the electrolyte, the electrodes, and also the separator. Finally, η_{ohm} mostly depends on the ionic resistivity of the electrolyte and the electronic resistance of the electrodes and current collectors. It scales linearly with the applied current according to Ohm's law. The voltage of the cell can then be summarized as follows: $V = E - (\eta_{aoa} + \eta_{aoc}) - (\eta_{coa} + \eta_{coc}) - iR$, where V is the voltage of the cell, E the equilibrium potential according to the Nernst equation, η_{aoa} and η_{aoc} the

activation overpotentials at the anode and cathode respectively, η_{coa} and η_{coc} the concentration overpotentials at the anode and cathode respectively, i the operating current, and R the resistance of the cell comprising η_{ohm}.[3, 4] Consequently, higher charging and discharging currents result in overpotentials that reduce the operating voltage of an electrochemical cell. With increasing overpotentials, the voltage profile deviates more from the equilibrium potential as illustrated in **Figure 2-1.**

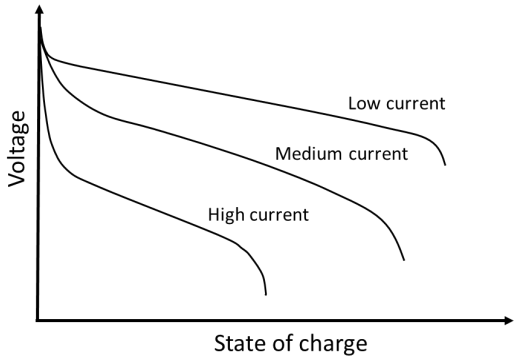

Figure 2-1 Typical discharge curves with increasing overpotentials with increasing current load.

The power performance or ability of a cell or material to handle large currents is routinely tested in rate tests. Here, starting from a low rate, the current is increased every few cycles. Typically, the capacity of a material decreases with increasing current loads, due to the higher resistance of the cell for higher currents as described above. Therefore, good power performance is closely linked to fast ionic transport in the electrolyte, separator, and electrodes and low resistances of current collectors and further cell components. Increasing overpotentials over time at a given current rate on the other hand indicate the evolution of resistive interfaces or materials decomposition, which result in overall increased resistance of the cell. This reduces the energy efficiency of the cell and indicates poor long-term stability.

In the battery community, the current rate is typically expressed as a C-rate, C/h, with h being the number of hours needed to reach the full capacity of a material at a given current. For a material with a capacity of 120 mAh g^{-1} for example, a C-rate of C/5 corresponds to a charging current of 24 mA g^{-1} and thus a charging time of five hours, whereas 5C corresponds to a current of 600 mA g^{-1} and a charging time of 12 minutes (1/5 hours).

In this thesis, GCPL was employed in **chapters 3, 4, 6** and **8** to characterize the operating potentials and cycling stability of electrode materials in various electrolytes. A key part are the long-term cycling tests of full-cells in **chapters 6** and **8**.

2.2 Electrolyte Properties

Physicochemical properties such as density, viscosity, or ionic conductivity are crucial factors influencing the performance of an electrochemical cell. High electrolyte density increases the weight of a cell, thus reducing the energy density, high viscosity may hinder the electrolyte from penetrating small pores in the active material, thereby influencing the activation overpotential and thus also energy/power density, and ionic conductivity affects e.g. the concentration overpotential and Ohmic losses, i.e. the power performance of the cell as described above.[3]

In a polar solvent like water, the dissolved ions, particularly the cations, are surrounded by solvent molecules resulting in a solvation shell around the ion.[3, 5] In an applied electric field, these solvated ions move towards the oppositely charged electrode. The resistance to this movement influences the ionic conductivity and is governed by various factors such as the charge, size, and shape of the moving ion, the extent of hydration/solvation, viscosity of the medium, and the solvent properties themselves, e.g. the dielectric constant.[5-7] The physicochemical properties of the electrolyte are thus linked to the solution structure, i.e. solvent-solute, solute-solute, and solvent-solvent interactions, and molecular structures of the electrolytes constituents.

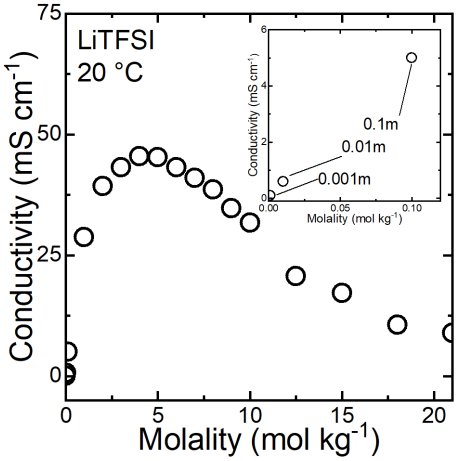

Figure 2-2 Ionic conductivity vs. concentration plot for aqueous LiTFSI solutions at 20 °C. The inset shows the linear dependence in the very dilute regime.

At concentrations above ca. 0.001m, solutions increasingly deviate from ideal behavior, where the dissolved ions would be distributed homogeneously without influencing each other resulting in a linear increase of conductivity with increasing concentration. Electrostatic interactions according to Coulombs law between the ions become relevant, increasingly so with higher charge density of the ions and lower dielectric constant of the solvent. Ion associates, e.g. ion pairs, can be formed at higher concentrations, effectively reducing the mobility of charge carriers, resulting in a lower than expected conductivity.[5-7] For many salts a maximum

in conductivity is observed at a concentration of ca. 4-5m, above which ion pair formation and larger agglomerates become dominant, resulting in gradually decreasing ionic conductivity as shown in **Figure 2-2**, discussed in more detail in **chapters 3** and **5**.[8] This change in solution structure with increasing concentration is particularly relevant for water-in-salt electrolytes, where due to the high concentration most ions can be expected to be paired/agglomerated to a certain degree. Solution structure of such water-in-salt electrolytes is discussed in more detail in the following chapters.

A critical factor for electrolyte properties is the charge density and polarizability of the dissolved ions, which greatly influences intermolecular interactions.[9, 10] For example, although the (crystallographic) ionic radius of alkali metal cations increases from Li^+<Na^+<K^+, the ionic conductivity at a given concentration is higher for potassium than lithium salt containing electrolytes.[11] The higher charge density of Li^+ cannot be shielded by a single layer of hydrating water molecules, resulting in an overall larger hydration shell containing a secondary sheath of water molecules.[12] Accordingly the radii of the hydrated cations, which is the entity that moves through the solution - not the bare cation, decreases in the order Li^+>Na^+>K^+ yielding the observed trend in ionic conductivities.[12] This is discussed in detail in **chapters 3** and **5**.

Viscosity is highly dependent on the molecular packing in the solution and thus the structure of the individual molecules in the electrolyte. One example is described in **chapter 4**, where a 35m NaFSI electrolyte, FSI being rather spherical, has a higher density but lower viscosity than an equimolar mixture of 25m NaFSI + 10m NaFTFSI, FTFSI being asymmetric and more oblong in shape. This may seem counterintuitive, assuming that in a highly dense solution an ion would meet more resistance upon movement, but it makes sense considering that the electrolyte is not a continuous medium but an assembly of intertwined individual molecules and ions. FSI may be packed more densely, but due to its small roundish shape it experiences less resistance when moving through the solution than the larger less spherical FTFSI anion, resulting in lower viscosity.[13]

In this thesis, impedance spectroscopy was used to determine the ionic conductivity of liquid electrolytes. The impedance of an electric circuit or component, such as an electrolyte or electrode material, corresponds to its effective resistance to an alternating current.[14] This method is used to probe a materials or components response to an oscillating electric field by scanning the frequency of the applied voltage over a wide range, typically from mHz to several MHz, at a constant amplitude, i.e. $V(t) = V_0 \sin(\omega t)$. The charges in the sample then move along the applied electric field and generate a response current, which oscillates with the same frequency but is phase shifted: $I(t) = I_0 \sin(\omega t - \phi)$. The impedance of the sample is then obtained as the ratio of V(t)/I(t), similar to Ohm's law that states the resistance as the

ratio of voltage and direct current R=V/I. Extrapolating the impedance to frequency = 0 Hz (corresponding to direct current) yields the resistance *R*. The direct current conductivity in a cell with a known geometrical factor C_0, or cell constant (dependent on the electrode distance *d* and Area *A*, $C_0 = \frac{A}{d}$), is then given by $\sigma_{dc} = (C_0 R)^{-1}$ and expressed in S m^{-1} (more typically S cm^{-1}). Viscosities were measured with an electromagnetically spinning sphere viscometer, where an aluminum sphere revolves in a sample container under a rotating external magnetic field. The viscosity is calculated from the rotational speed in the sample compared to a reference medium like high-purity water.

2.3 Raman Spectroscopy

Raman spectroscopy probes the rovibronic (rotational-vibrational) modes of molecules by inelastic scattering of an incident light beam, meaning that there is an exchange of energy resulting in an increase or decrease of the scattered beams energy.[15] The energy difference between the incident and scattered beam thus corresponds to the probed vibrational mode, e.g. a certain bond in a molecule. A monochromatic light source, usually a laser, is focused on the sample that is excited into a virtual energy state for a short time before the incident photon is reemitted. Typically, the sample molecules gain vibrational energy and the incident photons lose energy so the total energy remains constant. This is called Stokes Raman scattering. Anti Stokes Raman scattering is observed when the incident beam gains energy. Solid and liquid samples can easily be measured, but rotational modes are usually only observed in the gas phase.

The shift of energy with respect to the incident beam, the Raman shift, gives information of vibrational modes, e.g. bonds, in the sample and the pattern of Raman lines is characteristic of the molecular structure. Raman spectroscopy can also be used to better understand the local environment around a molecule, which can influence its symmetry, vibrational modes, and thus its Raman spectrum. Upon coordination of water to a cation for example, the vibrational mode of its O-H bonds is altered such that a shift to higher wavenumbers is observed.

In this thesis, Raman spectroscopy is extensively used to probe the solution structure of aqueous electrolytes in **chapters 3-8**. In pure water the many slightly different O-H stretching modes of water molecules in various hydrogen-bonding environments, e.g. bonded to one acceptor and one donor or two donors and two acceptors in a fully tetrahedral arrangement, result in a broad Raman signal as shown in **Figure 2-3**. The deconvolution of this signal into individual contributions is still actively discussed in literature.[16-18]

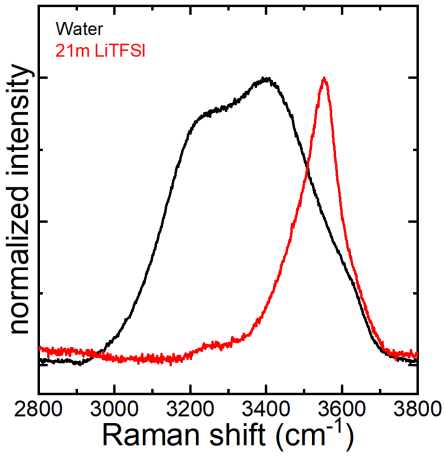

Figure 2-3 Raman spectra in the wavenumber region corresponding to the OH stretching modes of water in pure water and 21m LiTFSI, a typical water-in-salt electrolyte. The peaks are normalized for better comparison.

As hydrogen bonding is weakened, e.g. by increasing temperature or the addition of solutes that disturb the hydrogen-bonding network, the covalent O-H bonds are strengthened causing them to vibrate at higher frequencies.[19] Upon coordination to cations for example, the hydrogen-bonding network is broken and the water molecules are oriented with their oxygen atoms pointing towards the cations. This results in the evolution of a rather sharp peak with increasing salt concentration, a typical feature of highly concentrated aqueous electrolytes like 21m LiTFSI, shown in **Figure 2-3**.[8, 20] Similarly, solvent-solvent, solute-solvent, and solute-solute interactions can be monitored by observing shifting peaks that correspond to certain modes of the interacting molecules. The Raman band corresponding to the whole anion expansion and contraction modes of FSI for example is shifted to higher wavenumbers with increasing salt concentration. A stronger shift is observed with lithium compared to sodium due to the higher charge density and thus stronger interaction with the former cation.[21]

2.4 Differential Scanning Calorimetry

Differential scanning calorimetry (DSC) is a thermoanalytical method to detect phase transitions such as crystallization, melting, or glass transitions in various samples.[22] The difference in heat needed to increase the temperature of a sample versus a reference is measured as a function of temperature. In practical terms, an empty sample container with a known heat capacity serves as a reference while the sample is sealed in an identical container. The temperature is then scanned, while the heat flow for both crucibles is recorded. When the sample is undergoing a transformation such as phase transitions, more or less heat has to flow to the sample compared to the reference in order to keep both at the same temperature. Endothermic events, i.e. melting, will require a higher heat flow to reach the target temperature compared to the empty reference. Exothermic crystallizations on the other hand release heat, which reduces the needed amount of heat. Such first order transitions involve latent

heat that is absorbed or released at a well-defined temperature, which results in a sample-characteristic sharp peak in the DSC curve as shown in **Figure 2-4**. As these temperatures are scan rate dependent, the onset of the peaks is usually used to define the temperature of the transition of interest.[23, 24] Glass transitions are a second order phenomenon that can occur upon heating of an amorphous solid. They involve a change of the specific heat capacity of the material, resulting in a step rather than a peak in the DSC curves.

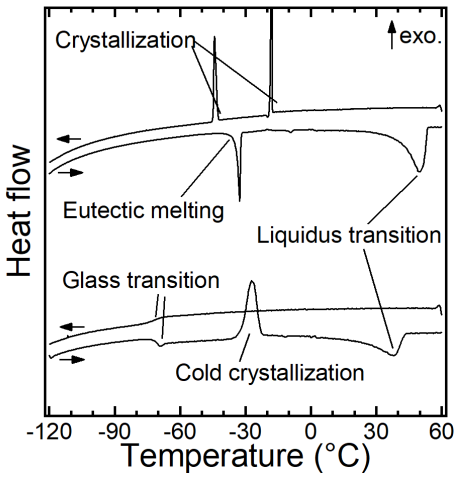

Figure 2-4 Differential scanning calorimetry curves of two water-in-salt electrolytes examined in this thesis, one showing crystallization upon cooling and melting of an eutectic phase during the heating scan, the other undergoing a glass transition followed by cold crystallization in the heating scan. Both electrolytes eventually undergo a liquidus transition at high enough temperatures. Recorded during scans from 60 to −120 °C and back.

In this thesis, DSC is used to define the temperature range in which electrolytes exist in liquid form in **chapters 6-8**. If the temperature is too low, the salt solubility limit can be reached and the electrolyte will partially crystallize, which results in battery failure. Typically, electrolyte samples were cooled at a slow scan rate and allowed to crystallize. During the heating scan, the melting temperature is determined, which defines the lower temperature limit for battery operation. In highly concentrated electrolytes however, mass transport can be rather slow which complicates DSC measurements. Often the samples did not undergo crystallization during the cooling process but showed just a glass transition into an amorphous solid, which for more dilute samples can usually only be achieved by quenching in liquid nitrogen. During the heating scan, a glass transition is observed and upon further heating, the amorphous solid becomes less viscous, resulting in increased motional freedom of the molecules. In some cases, cold crystallization, only possible from the amorphous state, may take place as the molecules spontaneously arrange into crystalline form. This is often followed by multiple melting processes of eutectic phases and eventually by the liquidus transition, which corresponds to the transition from a mixture of solid and liquid phases into a completely liquid electrolyte, again shown in **Figure 2-4**. The liquidus temperatures were determined by their peak maxima and eventually represent the lower temperature limit for stable operation of the cells.[23, 24]

2.5 Molecular Dynamics Simulations

Classical molecular dynamics (MD) is a computational simulation method to investigate the movement of atoms in a system. By calculating Newton's equation of motion for every atom in the simulation, both equilibrium as well as dynamical properties of the system can be computed at a given temperature. This numerical rather than analytical calculation is very efficient and accurate simulations are possible for large-scale systems with thousands of atoms over a timeframe of tens of nanoseconds. MD can therefore act as a computational microscope by providing atomic real-time information on the movement of atoms. See **Figure 2-5** for a typical workflow of a classical MD simulation. In practice, the atoms or molecules are placed in a simulation box, usually with periodic boundary conditions, and allowed to interact for a short time, typically for few femtoseconds. The forces between all particles are then calculated using interatomic potentials, often based on the simplest and widely used Lennard-Jones potential interaction model. It consists of a repulsive term at short distances due to overlapping electron orbitals, and an attractive long-range term that describes van der Waals type forces. Using these forces, the position and velocity of the particles in the next time step are calculated using Newton's laws of motion. This loop is then repeated millions of times, resulting in a molecular dynamics trajectory that tracks the movement of every atom in the simulation over typically tens of nanoseconds. In more practical studies, the simple interatomic potential or energy function is replaced by so called molecular mechanics force fields which include all parameters needed to calculate the potential energy of a system. These parameters are typically derived from experimental data and refined using quantum mechanical calculations. They include information such as atomic mass, van der Waals radius, force constants of bonds, equilibrium bond lengths and angles, charges, etc. The parameters for an oxygen atom for example are different in a carbonyl group and in a hydroxyl group. Particularly for the water molecule increasingly complex parameter sets, or water models, have been developed and are widely used without further optimization. The functional form of the potentials includes bonded terms for interactions of atoms that are connected by covalent bonds, and non-bonded terms for long-range electrostatic and van der Waals interactions. These are usually approximated by Coulomb's law and a Lennard-Jones-type potential, respectively, and computationally most expensive as they act between *every* pair of atoms. To speed up the simulation, a distance cut-off beyond/outside which non-bonded interactions are neglected is typically defined. The bonded interactions are composed of the energy between bonded atoms in the form of a harmonic force, i.e. a spring, the energy due to the angles between orbitals involved in bonding, and the energy due to torsion of bonds by neighboring atoms, lone pairs, or the bond order itself (e.g. single vs. double bond). The total energy is then the sum $E_{total} = E_{bonded} + E_{nonbonded}$, where the individual contributions can be written as

$E_{bonded} = E_{bonds} + E_{angles} + E_{dihedrals}$ and $E_{nonbonded} = E_{electrostatic} + E_{van\ der\ Waals}$. Additional terms, for example improper dihedrals enforcing the planarity of aromatic rings, can be added to improve the accuracy of the simulation.[14, 25-28]

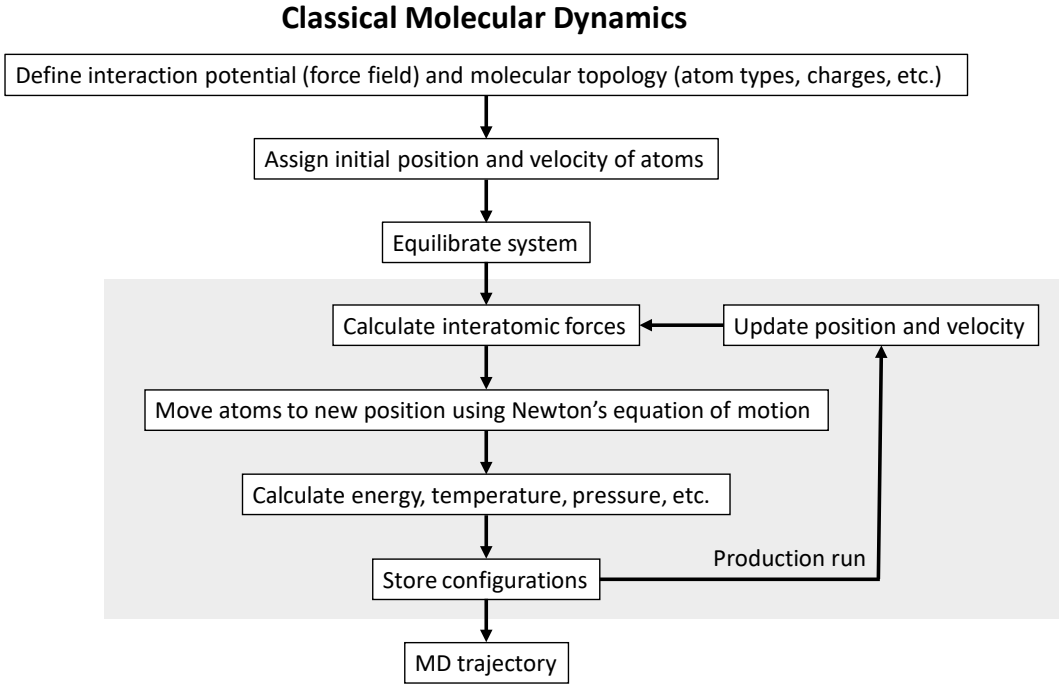

Figure 2-5 Typical MD workflow with the production run shaded in grey. The final trajectory is used for analysis.

As MD simulations move the molecular configuration forward in time in a step-by-step fashion, the trajectories are not only a great tool to investigate equilibrated systems, but in fact the simulation, the so called production run, is started from such an equilibrated state, thus allowing us to follow the dynamics, e.g. ionic conduction, in the system, see **Figure 2-5**. As an example, MD is perfectly suited to investigate the solution structure and dynamics in liquid electrolytes, e.g. in hydration shells or agglomerates, and it is possible to extract diffusion coefficients or rheological parameters. Note that the resulting parameters such as viscosity or diffusion coefficients are highly dependent on the initial force field parametrization and that statistical errors can be significant, particularly if the production run is short. Interactions become uncorrelated over a characteristic decay time and the simulation run time should be large compared to that. Similarly, the simulation box should be large compared to the characteristic distance over which interactions become uncorrelated. The exact parameters of course depend on the investigated system.

For condensed phase ionic systems such as ionic liquids or water-in-salt electrolytes it has further been shown that the polarizability of the particles has a significant influence on the dynamical properties in the simulation. This effect grows with increasing interaction of molecules, i.e. with increasing concentration. The lack of polarizability in most commonly used

force fields can be compensated by arbitrarily scaling the charges until dynamical properties reach experimental values. Often a scaling factor of ca. 0.8 is used for ionic liquids.[29]

To increase the accuracy of the calculation so called ab-initio simulations are also routinely conducted. Here the interatomic forces are calculated in real-time from electronic structure calculations. This approach is based on density functional theory and comes at significantly increased computational cost. Therefore, this is usually only done for few molecule systems to improve the understanding of e.g. individual solvation shells and is a complimentary technique to larger-scale classical MD simulations.

In **chapter 7** of this thesis, highly concentrated aqueous electrolytes containing symmetric or asymmetric anions were simulated using the Amber16 software package in Prof. Atsuo Yamada's laboratory at the University of Tokyo. The trajectories were analyzed to improve the understanding of solution structure in such concentrated systems. Information on local dynamics, such as bond rotations, was extracted and related to structural properties and experimental data.

References

1. Inzelt, G., A. Lewenstam, and F. Scholz, *Handbook of reference electrodes*. 2013: Springer.
2. La Mantia, F., et al., *Reliable reference electrodes for lithium-ion batteries.* Electrochemistry Communications, 2013. **31**: p. 141-144.
3. Huggins, R., *Advanced batteries: materials science aspects*. 2008: Springer Science & Business Media.
4. Massé, R.C., et al., *Energy storage through intercalation reactions: electrodes for rechargeable batteries.* National Science Review, 2017. **4**(1): p. 26-53.
5. Bockris, J.O.M., *Modern electrochemistry 2B: electrodics in chemistry, engineering, biology and environmental science*. Vol. 2. 2000: Springer Science & Business Media.
6. Angell, C. and R. Bressel, *Fluidity and conductance in aqueous electrolyte solutions. Approach from the glassy state and high-concentration limit. I. Calcium nitrate solutions.* The Journal of Physical Chemistry, 1972. **76**(22): p. 3244-3253.
7. Xu, W., E.I. Cooper, and C.A. Angell, *Ionic liquids: ion mobilities, glass temperatures, and fragilities.* The Journal of Physical Chemistry B, 2003. **107**(25): p. 6170-6178.
8. Suo, L., et al., *"Water-in-salt" electrolyte enables high-voltage aqueous lithium-ion chemistries.* Science, 2015. **350**(6263): p. 938-43.
9. Hou, M., R. Lu, and A. Yu, *Polarizability series of aqueous polyatomic anions revealed by femtosecond Kerr effect spectroscopy.* RSC advances, 2014. **4**(44): p. 23078-23083.
10. Grossfield, A., P. Ren, and J.W. Ponder, *Ion solvation thermodynamics from simulation with a polarizable force field.* Journal of the American Chemical Society, 2003. **125**(50): p. 15671-15682.

11. Reber, D., R.-S. Kühnel, and C. Battaglia, *High-voltage aqueous supercapacitors based on NaTFSI.* Sustainable Energy Fuels, 2017. **1**(10): p. 2155-2161.
12. Nightingale Jr, E.R., *Phenomenological theory of ion solvation. Effective radii of hydrated ions.* J. Phys. Chem., 1959. **63**(9): p. 1381-1387.
13. Sakai, K., T. Hirano, and M. Hosoda, *Electromagnetically spinning sphere viscometer.* Applied Physics Express, 2010. **3**(1): p. 016602.
14. Habasaki, J., C. Leon, and K. Ngai, *Dynamics of glassy, crystalline and liquid ionic conductors.* Top Appl Phys, 2017. **132**: p. 355-410.
15. Graves, P. and D. Gardiner, *Practical raman spectroscopy.* Springer, 1989.
16. Cross, P.C., J. Burnham, and P.A. Leighton, *The Raman spectrum and the structure of water.* Journal of the American Chemical Society, 1937. **59**(6): p. 1134-1147.
17. Sun, Q., *Local statistical interpretation for water structure.* Chemical Physics Letters, 2013. **568**: p. 90-94.
18. Auer, B. and J. Skinner, *IR and Raman spectra of liquid water: Theory and interpretation.* The Journal of chemical physics, 2008. **128**(22): p. 224511.
19. Walrafen, G., *Raman spectral studies of the effects of temperature on water structure.* The Journal of Chemical Physics, 1967. **47**(1): p. 114-126.
20. Yamada, Y., et al., *Hydrate-melt electrolytes for high-energy-density aqueous batteries.* Nat. Energy, 2016. **1**: p. 16129.
21. Reber, D., et al., *Stability of aqueous electrolytes based on LiFSI and NaFSI.* Electrochimica Acta, 2019. **321**: p. 134644.
22. Wunderlich, B., *Thermal analysis of polymeric materials*. 2005: Springer Science & Business Media.
23. Ding, M.S., K. Xu, and T.R. Jow, *Liquid-Solid Phase Diagrams of Binary Carbonates for Lithium Batteries.* J. Electrochim. Soc., 2000. **147**(5): p. 1688-1694.
24. Xu, K., *Nonaqueous liquid electrolytes for lithium-based rechargeable batteries.* Chemical reviews, 2004. **104**(10): p. 4303-4418.
25. Allen, M.P., *Introduction to molecular dynamics simulation.* Computational soft matter: from synthetic polymers to proteins, 2004. **23**: p. 1-28.
26. Allen, M.P. and D.J. Tildesley, *Computer simulation of liquids*. 2017: Oxford university press.
27. Wang, J., et al., *Development and testing of a general amber force field.* Journal of computational chemistry, 2004. **25**(9): p. 1157-1174.
28. Kühne, T.D., *Second generation Car-Parrinello molecular dynamics.* Wiley Interdisciplinary Reviews: Computational Molecular Science, 2014. **4**(4): p. 391-406.
29. Bedrov, D., et al., *Molecular dynamics simulations of ionic liquids and electrolytes using polarizable force fields.* Chemical reviews, 2019. **119**(13): p. 7940-7995.

3 High-Voltage Aqueous Supercapacitors Based on NaTFSI

David Reber,[1,2] Ruben-Simon Kühnel,[1] and Corsin Battaglia[1]

[1]Laboratory Materials for Energy Conversion, Swiss Federal Laboratories for Materials Science and Technology, Empa, Überlandstrasse 129, 8600 Dübendorf, Switzerland

[2]Institut des Matériaux, École Polytechnique Fédérale de Lausanne, EPFL, Station 12, 1015 Lausanne, Switzerland

Sustainable Energy & Fuels, 2017, 1, 2155-2161

DOI: 10.1039/C7SE00423K

https://pubs.rsc.org/en/content/articlelanding/2017/SE/C7SE00423K

In this study, we translate the water-in-salt concept to sodium electrolytes and recognize salt solubility as a major challenge. We scrutinize accurate measurement of electrochemical stability using high surface-area activated carbon electrodes and demonstrate our findings by developing a highly stable aqueous supercapacitor. **Author contributions:** D.R., R.-S.K., C.B. conceived the idea for this study. D.R. and R.-S.K. designed most experiments. D.R. carried out the experiments. D.R., R.-S.K., C.B. analyzed the data. D.R. prepared the figures and wrote the original draft of the manuscript. R.-S.K. and C.B. critically reviewed and edited the manuscript. All coauthors read and approved the final manuscript.

Abstract

Ultra-high salt concentration has recently been reported to extend the kinetic stability of aqueous electrolytes up to 3 V. However, the low ionic conductivity of these systems makes them unsuitable for high power devices such as supercapacitors. In this study, an 8 mol kg^{-1} NaTFSI aqueous electrolyte is reported that displays high stability of 1.8 V on activated carbon during a stringent stability test and conductivity of 48 mS cm^{-1} at 20 °C, the latter being comparable to the one of state-of-the-art acetonitrile-based non-aqueous electrolytes. A 1.8 V carbon/carbon supercapacitor employing 8 mol kg^{-1} NaTFSI displays a high maximum energy density of 14.4 Wh kg^{-1} on the activated carbon mass level and stable cycling for 100,000 cycles. By addition of the redox additive potassium iodide to the electrolyte, the maximum specific energy could be increased to an extremely high value of 37.8 Wh kg^{-1}, comparable to the performance of the current generation of commercial non-aqueous supercapacitors.

3.1 Introduction

Supercapacitors based on aqueous electrolytes are potentially safer and environmentally more benign than their non-aqueous electrolyte counterparts which typically employ highly flammable acetonitrile as the electrolyte solvent.[1] The low thermodynamic stability of water of 1.23 V puts aqueous double-layer capacitors at a natural disadvantage in terms of volumetric and gravimetric energy (E) and power (P) densities as both metrics scale with the square of the maximum operating voltage (V) ($E = 1/2CV^2$ and $P = V^2/(4R)$ with capacitance (C) and equivalent series resistance (R)).[2] In comparison, commercial non-aqueous supercapacitors are currently rated at up to 3.0 V.

The lower voltage of aqueous supercapacitors is partly offset by higher capacitance values of activated carbon (AC) in aqueous electrolytes due to the higher relative permittivity of water compared to acetonitrile.[2] In addition, the capacitance of AC in aqueous electrolytes benefits from typically smaller ion sizes and pseudocapacitive contributions from fast redox

reactions between surface functional groups and e.g. hydronium ions.[2] Redox active electrolyte additives like halogenides or quinone-based organics have been employed to further increase the capacitance of aqueous AC/AC supercapacitors.[3-5]

To increase the operating voltage and thus strongly increase the energy density of aqueous supercapacitors, several strategies have been proposed. Near pH-neutral electrolytes have improved kinetic stability compared to strongly basic or acidic solutions based on e.g. KOH or H_2SO_4, for which the cell voltage is limited to about 1 V. For 1 mol L^{-1} Li_2SO_4, initial results suggested stable long-term cycling up to 2.2 V using gold current collectors.[6] However, later studies revealed several stability issues for this system arising from water oxidation/reduction at high cell voltages. For example, carbon oxidation on the positive electrode by water oxidation products, resulting in continuous capacitance fading, has been observed in 1 mol L^{-1} Li_2SO_4 when the cell voltage exceeded values as low as 1.5 V.[7, 8] On the negative side, hydrogen formation is accompanied by an increase in local pH which can be detrimental to the stability of the current collector.[9] Furthermore, hydrogen evolution during operation of such systems at high voltages also raises safety concerns.

A possible solution for these stability and safety issues is the use of highly concentrated aqueous electrolytes. Recently very large stability windows of up to 3 V have been reported for ultra-highly concentrated aqueous electrolytes such as the water-in-salt system, 21 mol kg^{-1} (21m) LiTFSI (TFSI=$N(SO_2CF_3)_2$), by the battery community.[10-12] The increased apparent stability window is a consequence of the very small water-to-salt ratio in these systems leading to low fractions of free water molecules and increased average oxidative stability of water molecules and electrolyte anions. In addition, the formation of a passivation layer from reductive decomposition of electrolyte anions that further reduces the kinetics of the hydrogen evolution reaction has been reported for these systems.[10, 12] Furthermore, suppressed Al current collector dissolution has been reported for the water-LiTFSI system at very high salt concentration.[13] First studies using such highly concentrated electrolytes in supercapacitors indeed indicate improved stability compared to the Li_2SO_4 system. Gambou-Bosca and Bélanger reported a useable voltage window of 2.3 V for an AC-MnO_2 pseudocapacitor containing 5M (≈20m) LiTFSI.[14] Hasegawa et al. demonstrated stable cycling of an AC/AC supercapacitor based on 5M LiTFSI for 10,000 cycles at 5 A g^{-1} when cycled up to 2.4 V.[15] Tomiyasu et al. claimed even 3.2 V stability for a supercapacitor based on a saturated $NaClO_4$ solution.[16] However, the low conductivity of these highly concentrated aqueous electrolytes presents a major impediment to their use in high power devices such as supercapacitors.[14, 17]

Inspired by the trend of increasing conductivity with increasing cationic radius for other aqueous alkali metal salt solutions,[18] we explore solubility, conductivity and electrochemical

stability of different alkali metal TFSI salts in aqueous solutions on AC. The results are compared to values for the widely studied Li_2SO_4 system. Interestingly, we find conditions very suitable for supercapacitors at a NaTFSI concentration of 8m. This electrolyte displays a room temperature conductivity of ~50 mS cm^{-1} compared to <10 mS cm^{-1} for 21m LiTFSI, while the electrochemical stability window on AC of 1.8 V is only 200 mV smaller than the one for 21m LiTFSI. A double-layer capacitor based on 8m NaTFSI shows excellent rate performance and stability for 100,000 cycles when charged up to 1.8 V. Finally, we present results for a cell with the redox additive potassium iodide added to the NaTFSI electrolyte. This device displays an extremely high maximum energy density of 37.8 Wh kg^{-1} on the activated carbon mass level, reaching the performance of commercial non-aqueous electrolyte supercapacitors.

3.2 Results and Discussion

Figure 3-1a shows the concentration dependent conductivity at 20 °C of aqueous solutions of LiTFSI, NaTFSI, and KTFSI, respectively. We find that for a given molality the conductivity (σ) increases in the order $\sigma_{LiTFSI}<\sigma_{NaTFSI}<\sigma_{KTFSI}$. For example, at 1m the conductivities are 29, 37, and 46 mS cm^{-1} for LiTFSI, NaTFSI, and KTFSI, respectively. The same trend has been observed for other aqueous solutions of alkali metal salts and can be rationalized with the effective radii of the solvated cations.[18] With increasing cation radius (r) (in crystals: $r_c^{Li+}<r_c^{Na+}<r_c^{K+}$), the charge density decreases and hence ion-dipole forces between cation and water molecules weaken. As a consequence, at least for dilute solutions, the effective radii (r_h) of the corresponding hydrated cations decrease within increasing r_c, i.e. $r_h^{Li+}>r_h^{Na+}>r_h^{K+}$.[19] And the smaller the effective radius of the hydrated ion, the larger is the conductivity.

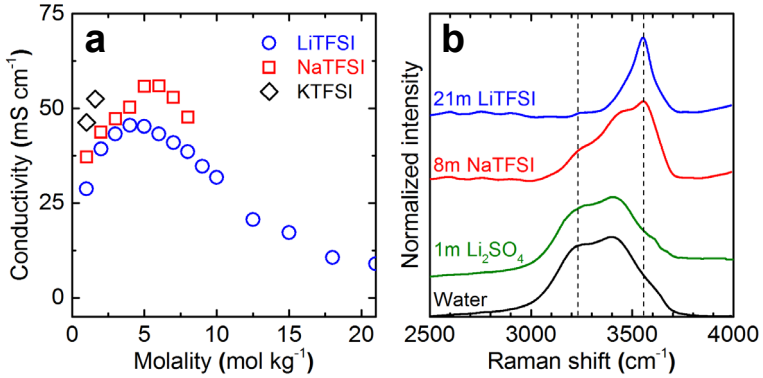

Figure 3-1 (a) Concentration-dependence of the conductivity of aqueous solutions of LiTFSI, NaTFSI, and KTFSI at 20 °C. (b) Raman spectra of pure water, 1m Li_2SO_4, 8m NaTFSI, and 21m LiTFSI in the wavenumber range corresponding to the OH stretching modes of water.

Another consequence of the differences in charge density is the difference in solubility. **Figure 3-1a** reports conductivity values up to the approximate room temperature solubility limit of each salt. The maximum solubility (c) decreases in the order $c_{LiTFSI}>c_{NaTFSI}>c_{KTFSI}$ from ca. 21 to 8 to 1.5m. Solubility is determined by the competition between the energy needed

to break-up the crystal lattice and the energy and entropy gains during hydration of the ions. Within a family of similar compounds, the melting points can often be used as a proxy for their relative lattice energies.[20] For the family of TFSI salts investigated here, the cations must determine the differences as the anions are identical. The high solubility of LiTFSI (~21m) is due to a combination of low lattice energy, as indicated by the low melting point of this salt (233 °C)[21], and high charge density of Li^+, which leads to a high hydration energy contribution. The melting point of NaTFSI is only slightly higher (257 °C)[21], indicating that the lattice energies are comparable. However, the 75% lower charge density of Na^+ compared to Li^+ indicates significantly lower hydration energy for NaTFSI compared to LiTFSI. The melting point of KTFSI (199 °C)[21] is slightly lower than the one of LiTFSI, indicating that the charge density of K^+, which is another 64% lower than the one of Na^+, is the cause for the lowest solubility in the series. Due to the relatively low solubility of KTFSI, solutions based on this salt were not further investigated in this study.

The conductivity of LiTFSI and NaTFSI solutions shows similar concentration dependences. At low concentration, the conductivity strongly increases with concentration, reaching maximum conductivities of 46 and 56 mS cm^{-1} for LiTFSI and NaTFSI at similar concentrations of 4 and 6m, respectively. When further increasing the concentration, the conductivity decreases faster for NaTFSI till reaching its solubility limit. The conductivity function of the LiTFSI solutions beyond the concentration of maximum conductivity is monotonically decreasing with increasing concentration and shows an inflection point at about 12m. For 21m LiTFSI, we measured a conductivity of 9 mS cm^{-1}, in line with previous reports.[10] At 8m, close to the solubility limit of NaTFSI, the LiTFSI and NaTFSI solutions display conductivities of 39 and 48 mS cm^{-1}, respectively. The latter value is very similar to the one of 1M Et_4N-BF_4 in acetonitrile (53 mS cm^{-1}), the standard non-aqueous electrolyte for supercapacitors and comparable to the one of 1m Li_2SO_4 (62 mS cm^{-1}). Due to its high conductivity at a relatively high concentration, we selected 8m NaTFSI as electrolyte for supercapacitors.

Raman spectra were recorded to compare the structure of pure water, 1m Li_2SO_4, 8m NaTFSI, and 21m LiTFSI. The bands observed between 2500-4000 cm^{-1} (**Figure 3-1b**) correspond to the OH stretching modes of water.[22] The various hydrogen bonding environments in water result in a broad Raman band between 2900-3700 cm^{-1}.[22] Upon salt addition, a distinct peak at ~3550 cm^{-1} emerges (see right dashed line in **Figure 3-1b**) that increases in intensity with increasing salt concentration.[23] At the same time, the broad signal of free water molecules vanishes.[23] Such a sharp OH stretching peak is typical for crystalline hydrates, indicating that a large fraction of water molecules is strongly interacting with Li^+.[10, 12] Indeed the fraction of free water molecules in 21m LiTFSI has been estimated from molecular dynamics simulations to be only ca. 15%.[10] The spectrum for 1m Li_2SO_4 resembles the one of pure

water, corresponding to a large fraction of free water in this electrolyte. In contrast, the fraction of free water in 8m NaTFSI appears to be significantly smaller. Compared to pure water, the intensity of the peak at ~3230 cm^{-1} (see left dashed line in **Figure 3-1b**) is significantly reduced and the sharp component at ~3550 cm^{-1} corresponding to water molecules strongly interacting with solution cations is clearly present.

Cyclic voltammetry (CV) in 3-electrode configuration with an oversized AC pellet as counter electrode was carried out to assess the electrochemical stability of 21m LiTFSI, 8m NaTFSI, and 1m Li_2SO_4 on AC working electrodes. We followed the potential opening approach, for both electrodes separately, and used a criterion based on Coulombic efficiency (η) to determine the stability limits.[24] We define stability as the last vertex potential (E_v) for which the modulus of the second derivative of η vs. E_v remains below 0.05 ($\left|\frac{d^2\eta}{dE_v{}^2}\right| < 0.05$). The rational put forward by Weingarth et al. for stability criteria based on the second derivative of Coulombic efficiency is to be able to distinguish between constant background currents, leakage currents that increase linearly with potential and currents corresponding to Faradaic processes, i.e. electrolyte decomposition.[24] The latter currents should increase exponentially with the potential as Faradaic processes generally follow the Butler-Volmer equation and can hence be detected as a change in the slope of η.[24] The CV curves and the corresponding η values are plotted in **Figure 3-2**.

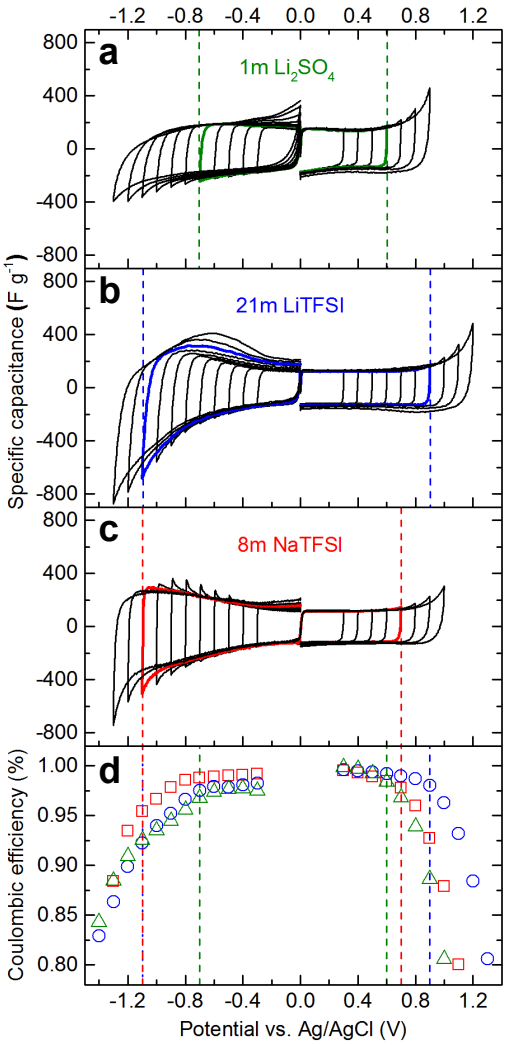

Figure 3-2 Cyclic voltammograms used to determine the stability windows of (a) 1m Li_2SO_4, (b) 21m LiTFSI, and (c) 8m NaTFSI. The scan rate was set to 1 mV s^{-1}. (d) Corresponding Coulombic efficiency vs. vertex potential plot. The vertical dashed lines correspond to the stability limits of the electrolytes according to the second derivative of efficiency criterion used in this work.

Positive effects of highly concentrated solutions are prominently observable for the positive electrode, where oxygen evolution is apparently pushed to higher potentials. The positive potential stability limit according to the second derivative of η criterion increases from 0.6 V vs. Ag/AgCl for 1m Li_2SO_4 to 0.7 V for 8m NaTFSI to 0.9 V for 21m LiTFSI. The increased stability can also be seen when comparing the Coulombic efficiencies for a fixed vertex potential. For example, for of a vertex potential of 0.8 V vs. Ag/AgCl, the efficiencies are 98.8% for 21m LiTFSI, 96.1% for 8m NaTFSI and only 94.2% for 1m Li_2SO_4. This can be explained with the higher energy of the highest occupied molecular orbital (HOMO) of water when coordinated to Li^+, i.e. higher oxidative stability of coordinated water molecules.[12] As the fraction of free water molecules strongly decreases from 1m Li_2SO_4 over 8m NaTFSI to 21m LiTFSI as demonstrated above, the average HOMO energy of water increases and hence the oxidation kinetics decreases.

Positive effects of high concentration are also observable on the negative side. Here, the negative potential stability limit according to the second derivative of η criterion decreases from -0.7 V vs. Ag/AgCl for 1m Li_2SO_4 to -1.1 V for 8m NaTFSI and 21m LiTFSI. Interestingly, we

find the highest Coulombic efficiencies for 8m NaTFSI and not for 21m LiTFSI. As previously shown both experimentally and theoretically, $TFSI^-$ reduction is shifted to more positive potentials at ultra-high concentration as a consequence of the proximity of Li^+ and $TFSI^-$ at such high concentration.[10, 12] This has been described as a positive effect of ultra-high salt concentration for batteries, leading to the formation of LiF-based passivation layers that reduce the kinetics of hydrogen formation on the anode side. However, for a supercapacitor we suspect that this could lead to pore clogging and hence reduced capacitance over time. At 8m, at least for NaTFSI, the reductive stability of $TFSI^-$ seems not to be altered significantly judging from the higher efficiency between -0.7 and -1.1 V vs. Ag/AgCl and the similarity in peak position of the major $TFSI^-$ Raman band at ~745 cm^{-1} for diluted (1m) compared to 8m NaTFSI (**Figure 3-6**). For 21m LiTFSI, the peak position is more similar to the one in crystalline LiTFSI, indicative of a stronger average interaction between Li^+ and $TFSI^-$ at this concentration, which leads to the change in reductive stability.

Subtracting the potential limits for the negative from the limits for the positive electrodes, we obtain stability windows of 2.0 V, 1.8 V and 1.3 V for 21m LiTFSI, 8m NaTFSI and 1m Li_2SO_4, respectively. When comparing the stability window on activated carbon of 2.0 V for 21m LiTFSI with literature data obtained using other working electrodes, it is interesting to note that the stability window strongly depends on the nature of the electrode, i.e. on the electrocatalytic properties with respect to the hydrogen and oxygen evolution reactions. Consequently, stability windows of 2.3, 2.8 and even 4.1 V were measured on platinum, gold, and glassy carbon electrodes, respectively.[25] The narrower window of 2.0 V obtained by us can be rationalized with differences in experimental parameters: We used a two orders of magnitude lower scan rate and AC has a much larger surface area compared to the flat electrodes used in the cited study. Furthermore, we apply a particularly stringent stability criterion.

In literature, somewhat larger stability windows of ≥1.5 V have been reported for Li_2SO_4 solutions using other stability criteria. The decreasing Coulombic efficiency with decreasing potential beyond -0.7 V vs. Ag/AgCl for 1m Li_2SO_4 is due to irreversible hydrogen formation. A higher upper cut-off potential than the 0 V vs. Ag/AgCl we used during the CV measurements might render this reaction more reversible, i.e. might allow partial re-oxidation of hydrogen. However, this would require an open circuit potential of AC in such solutions that is significantly higher than 0 V vs. Ag/AgCl, which is not the case for our AC on stainless steel or nickel electrodes. Furthermore, a high open circuit potential would complicate the electrode mass balancing as it would shrink the available potential range for the positive electrode.

Rate tests were performed in half-cell configuration for 1m Li_2SO_4, 8m NaTFSI, and 21m LiTFSI (**Figure 3-3**). Separate tests were carried out for the negative and positive electrodes and the cells were charged up to/down to the respective potential limits of the electrolytes determined in **Figure 3-2**, respectively. As expected from the differences in conductivity, the rate performance using 8m NaTFSI and 1m Li_2SO_4 is much better than the one using 21m LiTFSI. The capacitance for the former electrolytes shows only weak rate dependence, while it is very pronounced for the latter one. For example, when comparing the performance at 1 and 5 A g^{-1}, the capacitance retention is ≥88% for the highly conductive electrolytes and only ≤64%, and starting from lower absolute values, for 21m LiTFSI. The results clearly demonstrate the poor power capabilities of supercapacitors based on super-concentrated LiTFSI solutions. Even at 20 A g^{-1}, 8m NaTFSI and 1m Li_2SO_4 still deliver ≥82% and ≥92% of the capacitance values at 1 A g^{-1} for the negative and positive electrode, respectively. Overall, the capacitance retention is slightly better for 1m Li_2SO_4 compared to 8m NaTFSI due to the higher conductivity of the former electrolyte (62 vs. 48 mS cm^{-1} at 20 °C).

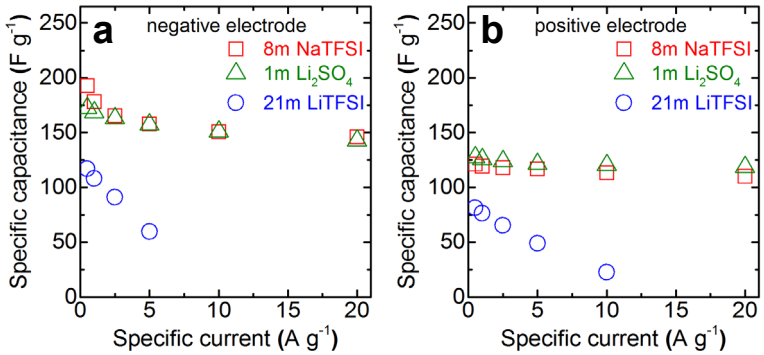

Figure 3-3 Rate-dependent capacitance of activated carbon in 1m Li_2SO_4, 8m NaTFSI, and 21m LiTFSI for the (a) negative and (b) positive electrode.

The absolute capacitance values for 8m NaTFSI and 1m Li_2SO_4 are very similar. We find higher maximum capacitance values for the negative (>170 F g^{-1}) compared to the positive electrodes (<130 F g^{-1}) in line with the cyclic voltammograms shown in **Figure 3-2**. We attribute this to the differences in ion size. For both electrolytes, the cations are smaller than the anions. The smaller Li^+ and Na^+ cations can access smaller pores than the bulkier SO_4^{2-} and $TFSI^-$ anions, giving rise to an ion sieving effect and additional capacitance for the negative electrode where the properties of the cations dominate.[26]

Among the investigated electrolytes, 8m NaTFSI shows the best combination of high conductivity (~50 mS cm^{-1} at room temperature) and wide electrochemical stability window (1.8 V). We therefore assembled full cells based on this electrolyte and carried out long-term cycling tests to assess the stability of the system. We used nickel as current collector material for the negative electrodes of these cells in light of a recent report that stainless steel is more prone to corrosion in such aqueous electrolytes than nickel under conditions where the local

pH might increase due to hydrogen formation.[9] Aluminum current collectors cannot be used in combination with 8m NaTFSI as we observe strong anodic aluminum dissolution in this electrolyte. We assign the lower stability of aluminum in 8m NaTFSI compared to 8m LiTFSI to the higher fraction of free water molecules in the former electrolyte due to the lower charge density of Na^+ compared to Li^+.[13] The tests were carried out at two different current densities, 1 and 10 A g^{-1} (referring to the total mass of AC) in order to study both the low and high rate stability. The capacitance retention for the two different loads is plotted in **Figure 3-4**. Both cells show initial capacitance fading of about 20% during the first ca. 1,000 cycles at 1 A g^{-1} and 15,000 cycles at 10 A g^{-1}. We assign the initial capacitance loss to irreversible oxidation/reduction of functional groups of the AC. After the initial fading, the capacitance loss per cycle is significantly reduced and the cells only loose further ca. 3% during the remaining cycles, demonstrating the feasibility of 8m NaTFSI as electrolyte for high-voltage aqueous supercapacitors.

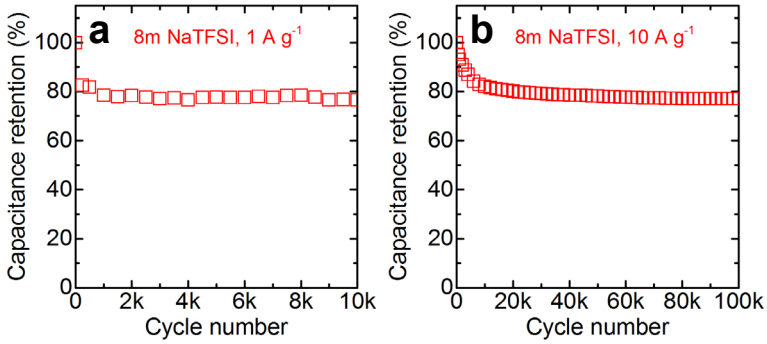

Figure 3-4 Capacitance retention obtained during long-term cycling of 1.8 V activated carbon full cells containing 8m NaTFSI as the electrolyte. The cells were subjected to (a) 1 A g^{-1} and (b) 10 A g^{-1}.

Commercial non-aqueous electrolyte supercapacitors currently reach up to about 35 Wh kg^{-1} on the activated carbon mass level. In comparison, our cell based on 8m NaTFSI shows a maximum specific energy of 14.4 Wh kg^{-1}. In order to close the gap in energy density and also to facilitate the mass balancing of the electrodes (for 8m NaTFSI, the positive electrode has to be massively oversized to compensate for its lower capacitance and smaller useable potential window compared to the negative electrode), a redox additive active at the positive electrode was added to the electrolyte. We chose potassium iodide (KI) because the reversible redox reactions of the iodine system take place around 0.3 V vs. Ag/AgCl, well within the stability window of 8m NaTFSI.[3, 27, 28] Potassium was selected as the counter ion to avoid a common ion effect and thus precipitation of NaTFSI.

We prepared a solution containing 8m NaTFSI and 0.5m KI, and carried out the same rate test for this electrolyte as the one shown in **Figure 3-3**. As expected, the performance of the

negative electrode is almost unaffected by KI addition to the electrolyte. In contrast, the positive electrode benefits significantly, especially at low rates. For redox additive-enhanced supercapacitors, capacity is usually a more suitable performance metric than capacitance because the voltage profile differs significantly from the one of a pure double-layer capacitor. With KI, the capacity of the positive electrode reaches very high values of 140 mAh g^{-1} at 0.5 A g^{-1} compared to 23.5 mAh g^{-1} without KI. At high currents, the performance of the positive electrode converges to the one operated without redox additive. This suggests that the kinetics of the redox reactions of the iodine species are significantly slower than double-layer formation for this system.

We also assembled a full cell with this electrolyte, which enables a balancing close to 1:1 due to the much improved capacitance of the positive electrode. Our preliminary results show that such a cell has a very high maximum specific energy of 37.8 Wh kg^{-1} on the activated carbon mass level, reaching or even exceeding the level of commercial non-aqueous electrolyte systems. However, due to the very different rate-dependence of the capacitance for the positive and negative electrodes, the optimal balancing is strongly rate dependent and a cell that is optimized for one rate tends to be less stable when cycled at other rates.

Increased self-discharge rates have been observed in the presence of certain redox additives.[29] However, a recent study reported that the self-discharge behavior of aqueous supercapacitors is not affected by the addition of KI to the electrolyte.[3] To confirm that this also applies to our system, we carried out self-discharge tests for cells containing 8m NaTFSI with and without addition of 0.5m KI (see experimental section for details). **Figure 3-7** shows the time evolution of the potential under open-circuit conditions after the AC electrodes were kept for 3 h at the potential stability limits determined above corresponding to a cell voltage of 1.8 V. The self-discharge of the negative electrode is not affected by the addition of KI. The potential of the positive electrode decays initially slightly faster with KI, but stabilizes at comparable (in fact even slightly higher) potentials than without KI after 24 h in agreement with results reported in Ref. 3.

To compare the performance of supercapacitors based on 8m NaTFSI, 8m NaTFSI + 0.5m KI and 21m LiTFSI, we constructed a Ragone plot (**Figure 3-5**). The reported specific energy and power values are those of balanced full cells cycled within the electrochemical stability windows determined above. It is important to note that the AC electrodes used in all experiments were not optimized. Hence, only the maximum reported specific energies are realistic, while there is much room for improvement for the power performance.

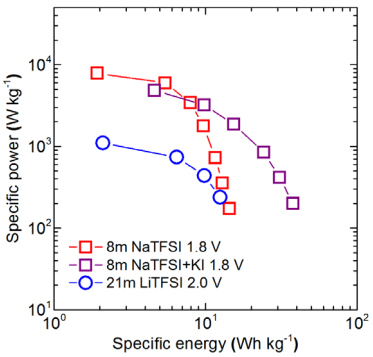

Figure 3-5 Ragone plot on the activated carbon mass level comparing specific energy and power of full cells containing 8m NaTFSI (1.8 V), 8m NaTFSI + 0.5m KI (1.8 V), and 21m LiTFSI (2.0 V) as the electrolyte, respectively.

The outstanding maximum energy density of the cell based on the KI enhanced electrolyte (37.8 Wh kg^{-1}) even surpasses commercial systems at low currents. However, the power performance of this system suffers from strong load dependence of the pseudocapacitive contribution of KI to the total capacitance of the positive electrode. The device based on 21m LiTFSI also displays a relatively high maximum specific energy of 12.5 Wh kg^{-1} on the activated carbon mass level during our test, benefiting from the largest maximum cell voltage of 2.0 V. However, due to the low conductivity of the electrolyte, the energy that can be stored in such a device is very load dependent and the maximum power performance of the system is relatively poor. The supercapacitor based on 8m NaTFSI shows the most balanced behavior. Although the maximum energy density is limited to 14.4 Wh kg^{-1}, it shows the best energy retention with increasing current and the highest maximum power of all investigated systems.

3.3 Conclusions

Alkali metal TFSI solutions of a concentration of 8m are promising aqueous electrolytes for supercapacitors due to their comparably high conductivity but improved electrochemical stability compared to standard concentration (~1m) pH-neutral aqueous electrolytes. We demonstrated that the stability window on AC is enhanced by several hundred millivolts to 1.8 V for 8m NaTFSI compared to 1m Li_2SO_4.

In addition, 8m NaTFSI exhibits a room temperature conductivity of ~50 mS cm^{-1}, comparable to the one of state-of-the-art non-aqueous electrolytes based on acetonitrile. Ultra-highly concentrated electrolytes like 21m LiTFSI suffer not only from low conductivity (<10 mS cm^{-1}) as pointed out previously,[14] but our tests also show lower Coulombic efficiencies on the negative electrode for this electrolyte compared to 8m NaTFSI.

We also demonstrate that the combination with a redox additive further narrows the gap in energy density between aqueous and non-aqueous supercapacitors. An AC/AC full cell based on 8m NaTFSI + 0.5m KI displays a very high maximum energy density of 37.8 Wh kg^{-1} on the activated carbon mass level when charged up to 1.8 V, comparable to the performance

of state-of-the-art non-aqueous supercapacitors. However, electrode balancing for such a system remains challenging because the pseudocapacitive contribution of the redox additive to the capacitance of the positive electrode is very rate dependent and hence the optimal balancing strongly depends on the targeted load. The balancing issue could be eased by the use of a second redox additive active at the negative electrode that would lead to more similar capacitance retention for the two electrodes, bringing the performance of aqueous to the level of organic electrolyte supercapacitors.

3.4 Methods

The electrolytes were prepared by dissolving the as received salts LiTFSI (99.95%, Sigma-Aldrich or 99.9%, Solvionic), NaTFSI (99.5%, Solvionic), KTFSI (99.5%, Solvionic), Li_2SO_4 (99.99%, Alfa Aesar) and KI (≥99.5%, Sigma-Aldrich), respectively, in high purity water (prepared with a Millipore Milli-Q water purification system). Neutral pH was established by addition of appropriate amounts of a suitable hydroxide solution and the electrolytes were degassed with argon or nitrogen prior to their use.

Ionic conductivity was determined by impedance spectroscopy in sealed 2-electrode cells equipped with Pt electrodes (Materials Mates HTCC) using a Bio-Logic VMP3 electrochemical workstation. The temperature was controlled with a climatic chamber (Binder MK53). The electrolyte resistance was extracted from the intersection of the complex impedance curve with the x-axis in a Nyquist plot.

Raman spectra of selected electrolytes sealed in NMR tubes were collected at room temperature on a Renishaw Ramascope between 100 and 4000 cm^{-1} using a laser with a wavelength of 633 nm.

All supercapacitors were assembled in stainless steel T-type Swagelok cells in 3-electrode configuration and characterized using a Bio-Logic VMP3 electrochemical workstation. An Ag/AgCl miniature electrode (eDAQ) was used as reference. For the half-cell tests, oversized AC pellets served as counter electrode.

AC (MTI AB-520, coconut-derived, BET surface area: 2000±100 $m^2 g^{-1}$, pore volume: 0.9±0.1 $cm^3 g^{-1}$, carbon content: >95%) electrodes were prepared by casting a slurry consisting of 85% AC, 10% carbon black (IMERYS Graphite & Carbon C-NERGY SUPER C65) and 5% polyvinylidene difluoride (PVdF) binder (Arkema Kynar HSV900) suspended in *N*-methyl-2-pyrrolidone (NMP) on stainless steel (grade 1.4310; thickness: 25 µm) or nickel (grade 2.4068; thickness: 20 µm) foils. The stainless steel foils were etched in 4m KOH heated to 60 °C for 30 s and both foils were roughened (further) with sandpaper before casting to improve adhesion. The electrode sheets were then dried over night at 80 °C in air and electrode discs with a diameter of 12 mm were punched out. The electrodes were then pressed at 15 t for 30 s before a final

drying step at 120 °C under vacuum over night. The AC mass loading was about 1-2 mg for all tests except for the full cell tests, where the combined mass loading of both electrodes was about 6 mg.

The stability window of the electrolytes on AC was determined in half-cell configuration by cyclic voltammetry with a scan rate of 1 mV s^{-1}. After five conditioning cycles between ±0.2 V vs. Ag/AgCl, the cut-off potential was increased in 100 mV steps to ±1.5 V vs. Ag/AgCl and the second vertex potential was fixed at 0 V vs. Ag/AgCl. Three cycles were recorded for each potential window to reduce the influence of wetting phenomena and first cycle effects. Separate measurements were conducted for the negative and positive electrode, respectively.

Rate tests in half-cell configuration at specific currents ranging from 0.5 to 20 A g^{-1} were conducted separately for both electrodes in the respective potential windows. Balanced full cells were assembled for the long-term cycling tests and the Ragone plot by adapting the mass loadings of the positive and negative electrodes in a way that the potentials of electrodes would not significantly exceed their determined stability limits.

Self-discharge tests in half-cell configuration were conducted separately for the negative and positive electrodes. After 250 cycles of activation cycling at 1 A g^{-1}, the working electrode potentials were kept constant for 3 h at -1.1 or 0.7 V vs. Ag/AgCl, respectively. Subsequently, the potential evolution over time was monitored for 24 h under open-circuit conditions.

3.5 Supporting Information

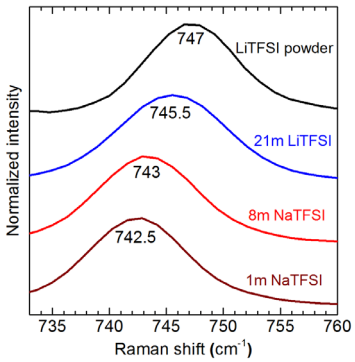

Figure 3-6 Raman spectra of 1m NaTFSI, 8m NaTFSI, 21m LiTFSI, and LiTFSI powder in the wavenumber region of the major $TFSI^-$ mode.

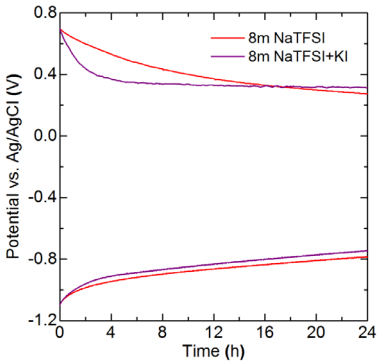

Figure 3-7 Self-discharge test of supercapacitors containing 8m NaTFSI or 8m NaTFSI + 0.5m KI as the electrolyte, respectively.

References

1. Béguin, F., et al., *Carbons and Electrolytes for Advanced Supercapacitors.* Advanced Materials, 2014. **26**(14): p. 2219-2251.
2. Conway, B.E., *Electrochemical Supercapacitors*. 1999, New York: Springer Science+Business Media.
3. Abbas, Q., et al., *Sustainable AC/AC hybrid electrochemical capacitors in aqueous electrolyte approaching the performance of organic systems.* Journal of Power Sources, 2016. **326**: p. 652-659.
4. Gastol, D., et al., *Enhancement of the carbon electrode capacitance by brominated hydroquinones.* Journal of Power Sources, 2016. **326**: p. 587-594.
5. Menzel, J., K. Fic, and E. Frackowiak, *Hybrid aqueous capacitors with improved energy/power performance.* Progress in Natural Science: Materials International, 2015. **25**(6): p. 642-649.
6. Fic, K., et al., *Novel insight into neutral medium as electrolyte for high-voltage supercapacitors.* Energy & Environmental Science, 2012. **5**(2): p. 5842-5850.

7. Ratajczak, P., K. Jurewicz, and F. Béguin, *Factors contributing to ageing of high voltage carbon/carbon supercapacitors in salt aqueous electrolyte.* Journal of Applied Electrochemistry, 2014. **44**(4): p. 475-480.
8. He, M., et al., *Ageing phenomena in high-voltage aqueous supercapacitors investigated by in situ gas analysis.* Energy & Environmental Science, 2016. **9**(2): p. 623-633.
9. Abbas, Q., et al., *Strategies to Improve the Performance of Carbon/Carbon Capacitors in Salt Aqueous Electrolytes.* Journal of The Electrochemical Society, 2015. **162**(5): p. A5148-A5157.
10. Suo, L., et al., *"Water-in-salt" electrolyte enables high-voltage aqueous lithium-ion chemistries.* Science, 2015. **350**(6263): p. 938-43.
11. Suo, L., et al., *Advanced High-Voltage Aqueous Lithium-Ion Battery Enabled by "Water-in-Bisalt" Electrolyte.* Angewandte Chemie International Edition, 2016. **55**(25): p. 7136-41.
12. Yamada, Y., et al., *Hydrate-Melt Electrolytes for High-Energy-Density Aqueous Batteries.* Nature Energy, 2016. **1**: p. 16129.
13. Kühnel, R.-S., et al., *"Water-in-salt" electrolytes enable the use of cost-effective aluminum current collectors for aqueous high-voltage batteries.* Chemical Communications, 2016. **52**(68): p. 10435-8.
14. Gambou-Bosca, A. and D. Bélanger, *Electrochemical characterization of MnO2-based composite in the presence of salt-in-water and water-in-salt electrolytes as electrode for electrochemical capacitors.* Journal of Power Sources, 2016. **326**: p. 595-603.
15. Hasegawa, G., et al., *Hierarchically Porous Carbon Monoliths Comprising Ordered Mesoporous Nanorod Assemblies for High-Voltage Aqueous Supercapacitors.* Chemistry of Materials, 2016. **28**(11): p. 3944-3950.
16. Tomiyasu, H., et al., *An aqueous electrolyte of the widest potential window and its superior capability for capacitors.* Scientific Reports, 2017. **7**: p. 45048.
17. Simon, P., Y. Gogotsi, and B. Dunn, *Materials science. Where do batteries end and supercapacitors begin?* Science, 2014. **343**(6176): p. 1210-1.
18. Mosqueda, H.A., et al., *Electrolytes for hybrid carbon–MnO2 electrochemical capacitors.* Electrochimica Acta, 2010. **55**(25): p. 7479-7483.
19. Nightingale, E.R., *Phenomenological Theory of Ion Solvation. Effective Radii of Hydrated Ions.* The Journal of Physical Chemistry, 1959. **63**(9): p. 1381-1387.
20. Gopal, R., *Relation Between Lattice Energy and Melting Points of Some Crystalline Substances. II. Alkali Metals.* Zeitschrift für anorganische und allgemeine Chemie, 1955. **278**(1-2): p. 42-45.
21. Hagiwara, R., et al., *Thermal Properties of Mixed Alkali Bis(trifluoromethylsulfonyl)amides.* Journal of Chemical & Engineering Data, 2008. **53**(2): p. 355-358.
22. Smith, J.D., et al., *Unified Description of Temperature-Dependent Hydrogen-Bond Rearrangements in Liquid Water.* Proceedings of the National Academy of Sciences of the United States of America, 2005. **102**(40): p. 14171-14174.

23. Yin, J., et al., *Concentrated NaClO4 aqueous solutions as promising electrolytes for electric double-layer capacitors.* Journal of Power Sources, 2011. **196**(8): p. 4080-4087.

24. Weingarth, D., et al., *A reliable determination method of stability limits for electrochemical double layer capacitors.* Electrochimica Acta, 2013. **103**: p. 119-124.

25. Coustan, L., G. Shul, and D. Belanger, *Electrochemical behavior of platinum, gold and glassy carbon electrodes in water-in-salt electrolyte.* Electrochemistry Communications, 2017. **77**: p. 89-92.

26. Eliad, L., et al., *Ion Sieving Effects in the Electrical Double Layer of Porous Carbon Electrodes: Estimating Effective Ion Size in Electrolytic Solutions.* Journal of Physical Chemistry B, 2001. **105**(29): p. 6880-6887.

27. Lota, G. and E. Frackowiak, *Striking capacitance of carbon/iodide interface.* Electrochemistry Communications, 2009. **11**(1): p. 87-90.

28. Senthilkumar, S.T., et al., *Electric double layer capacitor and its improved specific capacitance using redox additive electrolyte.* J. Mater. Chem. A, 2013. **1**(4): p. 1086-1095.

29. Chen, L., et al., *Mechanism investigation and suppression of self-discharge in active electrolyte enhanced supercapacitors.* Energy & Environmental Science, 2014. **7**(5): p. 1750-1759.

4 A High-Voltage Aqueous Electrolyte for Sodium-ion Batteries

Ruben-Simon Kühnel,[1] David Reber,[1,2] and Corsin Battaglia[1]

[1]Laboratory Materials for Energy Conversion, Swiss Federal Laboratories for Materials Science and Technology, Empa, Überlandstrasse 129, 8600 Dübendorf, Switzerland

[2]Institut des Matériaux, École Polytechnique Fédérale de Lausanne, EPFL, Station 12, 1015 Lausanne, Switzerland

ACS Energy Letters, 2017, 2, 2005−2006

DOI: 10.1021/acsenergylett.7b00623

https://pubs.acs.org/doi/abs/10.1021/acsenergylett.7b00623

Here we study the limited solubility, and eventually lower electrochemical stability, of aqueous sodium electrolytes compared to lithium based systems. We identify NaFSI as a promising salt for water-in-salt electrolytes due to its high solubility and develop the first water-in-salt electrolyte for sodium-ion batteries with a stability window of up to 2.6 V. **Author contributions**: D.R., R.-S.K., C.B. conceived the idea for this study. R.-S.K. identified NaFSI as a promising salt. D.R. and R.-S.K. designed most experiments. D.R. carried out the experiments. D.R., R.–S.K., C.B. analyzed the data. D.R. prepared the figures. R.-S.K wrote the original draft of the manuscript. D.R., R.-S.K., C.B. critically reviewed and edited the manuscript. All coauthors read and approved the final manuscript.

Abstract

Sodium bis(fluorosulfonyl)imide based aqueous electrolytes exhibit a wide electrochemical stability window of up to 2.6 V when the salt concentration is increased above 20 mol kg^{-1} enabling the fabrication of high-voltage rechargeable aqueous sodium-ion batteries.

4.1 Introduction

The major disadvantage of water as electrolyte solvent for batteries is its intrinsically narrow electrochemical stability window (thermodynamically only 1.23 V) limiting maximum cell voltage and consequently the battery's energy density. For the lithium system, the operational stability window could be increased recently to >2 V by the use of highly concentrated aqueous solutions of lithium salts containing perfluorinated anions such as bis(trifluoromethylsulfonyl)imide (TFSI).[1-3] We have shown that for the corresponding sodium system, the maximum solubility is only 8 mol kg^{-1} (8m) resulting in a relatively narrow stability window of only 1.8 V.[4]

Here we report the discovery of high solubility of sodium bis(fluorosulfonyl)imide (NaFSI) in water of ~21m and metastable solutions up to 37m. Aqueous NaFSI electrolytes display a room temperature conductivity of up to 90 mS cm^{-1} with a maximum around 4 mol kg^{-1}. Even above 30m the conductivity remains comparable to that of 21m LiTFSI. The solutions > 20m offer a much enhanced stability window of up to 2.6 V.

4.2 Results and Discussion

We prepared NaFSI solutions of various concentrations by dissolving the appropriate amounts of NaFSI (99.5%, Solvionic) in high-purity water (Millipore Milli-Q) under heating. The maximum room temperature solubility was determined by addition of small amounts of NaFSI acting as seed crystals. For solutions with concentrations exceeding ~37m, we observe rapid

solidification of the entire supersaturated solution upon seed crystal addition that we attribute to hydrate formation. Below ~37m, an additional marginal amount of NaFSI can still be dissolved and the mixture remains liquid. Upon longer storage however, we still observed crystallization and conclude a maximum stable room temperature solubility of ca. 21m.

Solubility is the competition between the energy needed to break up the crystal lattice and the energy and entropy gains upon hydration of the ions. The melting points of similar salts can often act as a proxy for their relative lattice energies.[5] NaTFSI has a melting point of 257 °C,[6] while the value for NaFSI is only 106 °C,[7] corresponding to a lower lattice energy for the latter salt if entropic effects play no significant role. In addition, the FSI^- anion is smaller than the $TFSI^-$ anion, corresponding to a higher charge density of the former anion. In a first approximation, the higher the charge density, the higher is the energy gain upon hydration of the ion. Hence, higher hydration energy can be expected for the dissolution of NaFSI compared to NaTFSI, further contributing to the high solubility of NaFSI.

Figure 4-1a shows the concentration-dependent conductivity of aqueous NaFSI solutions at 20 °C. The trend resembles that found for LiTFSI solutions; with a maximum at ~4 mol kg^{-1} (4m) and a decrease to 30 mS cm^{-1} at 21m and ca. 8 mS cm^{-1} at a concentration of 35m. For comparison, aqueous LiTFSI solutions display a maximum conductivity of 45 mS cm^{-1} at 4m and a conductivity of 9 mS cm^{-1} at the solubility limit of 21m.[1] The lower charge density of Na^+ compared to Li^+ apparently enables the high ion mobility at this water-to-salt molar ratio.

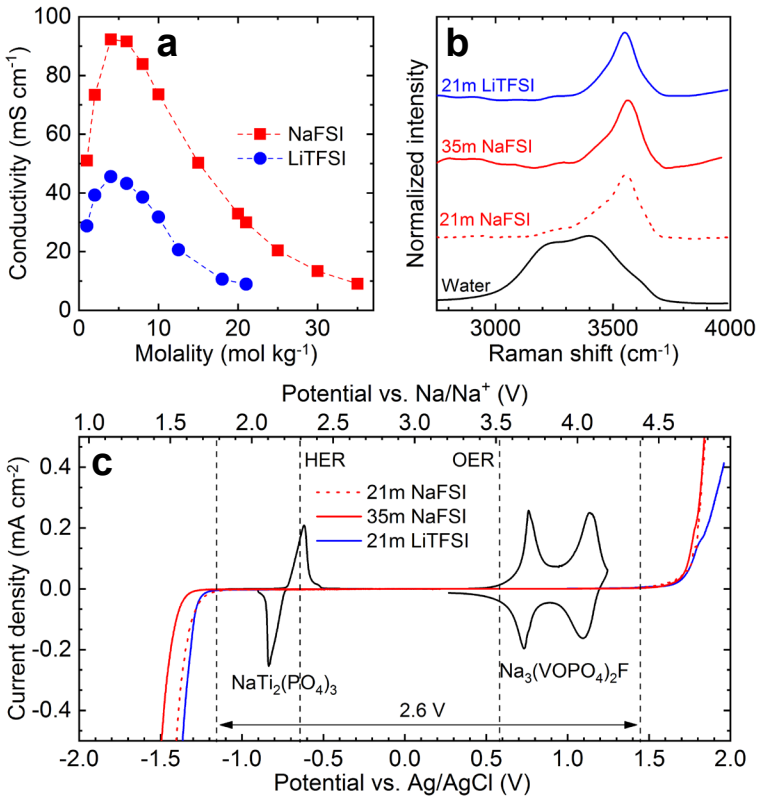

Figure 4-1 Conductivity, structural characterization, and electrochemical stability of aqueous electrolytes based on NaFSI: (a) conductivity at 20 °C, (b) Raman spectra in the wavenumber region corresponding to the OH stretching modes of water, and (c) electrochemical stability on stainless steel evaluated using linear sweep voltammetry at a scan rate of 0.1 mV s^{-1}. Cyclic voltammograms of $NaTi_2(PO_4)_3$ and $Na_3(VOPO_4)_2F$ based electrodes measured in 35m NaFSI at a scan rate of 0.05 mV s^{-1} are also shown. The current densities for the active material measurements were scaled to fit to the electrolyte stability measurements. The thermodynamic potentials for the hydrogen and oxygen evolution reactions at pH=7 are shown as vertical dashed lines labeled HER and OER, respectively. For comparison, data for aqueous LiTFSI solutions is also shown.

To probe the solution structure, we carried out Raman spectroscopy. **Figure 4-1b** shows the Raman spectra for pure water, 21m NaFSI, and 35m NaFSI in the wavenumber region corresponding to the OH stretching modes of water. For comparison, we also included the spectrum of 21m LiTFSI. Pure water shows a broad Raman band between 2900 and 3700 cm^{-1} due to its various hydrogen bonding environments.[8] In contrast, 21m LiTFSI shows a relatively narrow peak, resembling the one of water in crystalline hydrates.[1, 3] It has been shown via molecular dynamics simulations that the fraction of free water molecules is only ~15% and that the remaining 85% are strongly interacting with Li^+.[1] For NaFSI, the Raman signature is almost identical for 21m and 35m solutions, indicating that already at 21m most water is coordinating to sodium. Hence, we conclude that the water environment in concentrated NaFSI solutions resembles the one in 21m LiTFSI, i.e. most water molecules are simultaneously part of the first solvation sheath of the cations. Upon strong coordination to a cation, water molecules display a shift of the highest occupied molecular orbital to higher energy resulting in higher oxidative stability.[1, 3] In combination with the low fraction of free water molecules, a

wide electrochemical stability window can therefore be expected for NaFSI electrolytes at such high concentration.[1]

To confirm whether the change in solution structure results in the desired enhanced electrochemical stability, we carried out linear sweep voltammetry on stainless steel working electrodes in 3-electrode configuration at a scan rate of 0.1 mV s^{-1} (**Figure 4-1c**). 35m NaFSI displays a very wide electrochemical stability window of ca. 2.6 V, even slightly exceeding the already broad one of 21m LiTFSI. Compared to 21m NaFSI, only the cathodic stability seems to be slightly improved.

4.3 Conclusions

In summary, we discovered an aqueous sodium-ion electrolyte system with a much-enhanced electrochemical stability window. The wide stability window of 2.6 V for 21 to 35m NaFSI broadens the choice of suitable active materials for aqueous sodium-ion batteries. We are currently synthesizing and testing the anode material $NaTi_2(PO_4)_3$ and the cathode material $Na_3(VOPO_4)_2F$ in the NaFSI electrolytes.[9, 10] **Figure 4-1c** shows preliminary cyclic voltammetry data carried out at 0.05 mV s^{-1} for half-cells based on these active materials on stainless steel current collectors and metastable 35m NaFSI as the electrolyte. Both active materials show reversible behavior in this electrolyte, demonstrating the feasibility of 35m NaFSI as electrolyte for ≥2 V aqueous sodium-ion batteries.

References

1. Suo, L., et al., *"Water-in-salt" electrolyte enables high-voltage aqueous lithium-ion chemistries.* Science, 2015. **350**(6263): p. 938-43.
2. Suo, L., et al., *Advanced High-Voltage Aqueous Lithium-Ion Battery Enabled by "Water-in-Bisalt" Electrolyte.* Angewandte Chemie International Edition, 2016. **55**(25): p. 7136-41.
3. Yamada, Y., et al., *Hydrate-melt electrolytes for high-energy-density aqueous batteries.* Nature Energy, 2016. **1**: p. 16129.
4. Reber, D., R.-S. Kühnel, and C. Battaglia, Sustainable Energy & Fuels, 2017: p. submitted for publication.
5. Gopal, R., *Relation between lattice energy and melting points of some crystalline substances. II. Alkali Metals.* Zeitschrift für anorganische und allgemeine Chemie, 1955. **278**(1-2): p. 42-45.
6. Hagiwara, R., et al., *Thermal Properties of Mixed Alkali Bis(trifluoromethylsulfonyl)amides.* Journal of Chemical & Engineering Data, 2008. **53**(2): p. 355-358.

7. Kubota, K., T. Nohira, and R. Hagiwara, *Thermal Properties of Alkali Bis(fluorosulfonyl)amides and Their Binary Mixtures.* Journal of Chemical & Engineering Data, 2010. **55**(9): p. 3142-3146.
8. Smith, J.D., et al., *Unified description of temperature-dependent hydrogen-bond rearrangements in liquid water.* Proceedings of the National Academy of Sciences of the United States of America, 2005. **102**(40): p. 14171-14174.
9. Li, Z., et al., *Towards High Power High Energy Aqueous Sodium-Ion Batteries: The NaTi2(PO4)3/Na0.44MnO2 System.* Advanced Energy Materials, 2013. **3**(3): p. 290-294.
10. Qi, Y., et al., *Superior Na-Storage Performance of Low-Temperature-Synthesized Na3(VO1−xPO4)2F1+2x (0≤x≤1) Nanoparticles for Na-Ion Batteries.* Angewandte Chemie International Edition, 2015. **54**(34): p. 9911-9916.

5 Stability of Aqueous Electrolytes Based on LiFSI and NaFSI

David Reber,[1,2] Renato Figi,[1] Ruben-Simon Kühnel,[1] and Corsin Battaglia[1]

[1]Laboratory Materials for Energy Conversion, Swiss Federal Laboratories for Materials Science and Technology, Empa, Überlandstrasse 129, 8600 Dübendorf, Switzerland

[2]Institut des Matériaux, École Polytechnique Fédérale de Lausanne, EPFL, Station 12, 1015 Lausanne, Switzerland

Electrochimica Acta, 2019, 321, 134644

DOI: 10.1016/j.electacta.2019.134644

https://www.sciencedirect.com/science/article/pii/S0013468619315038

Benefitting from the high solubility of bis(fluorosulfonyl)imide (FSI) salts, we investigate the chemical stability of the anion in highly concentrated aqueous electrolytes. We find that the kinetics of the anion decomposition are highly cation- and concentration-dependent and report increased chemical stability for NaFSI based aqueous electrolytes compared to LiFSI analogues. **Author contributions:** D.R., R.-S.K., C.B. conceived the idea for this study. D.R. and R.-S.K. designed most experiments. D.R. carried out most experiments. R.F. performed the ion chromatography experiments. D.R., R.F., R.-S.K., C.B. analyzed the data. D.R. prepared the figures and wrote the original draft of the manuscript. R.-S.K. and C.B. critically reviewed and edited the manuscript. All coauthors read and approved the final manuscript.

Abstract

Through a combination of bulk, interface, and interphase effects, water-in-salt electrolytes, employing a high salt concentration, offer a wider electrochemical stability window than traditional dilute aqueous electrolytes. Here we explore chemical stability, conductivity, viscosity, and electrochemical stability of aqueous solutions of bis(fluorosulfonyl)imide (FSI) salts as electrolytes for lithium-ion and sodium-ion batteries. We demonstrate that the FSI anion is prone to hydrolysis in this environment. However, the kinetics of the reaction strongly depend on salt concentration and nature of the cation. Interestingly, we find that NaFSI solutions are significantly more stable than LiFSI solutions. Highly concentrated NaFSI solutions also display a wide electrochemical stability window and high conductivity.

5.1 Introduction

Novel rechargeable batteries based on aqueous electrolytes are developed as a large-scale stationary energy storage alternative to lithium-ion batteries based on organic electrolytes. The inherent non-flammability and potentially low total cost of ownership of such battery systems make them promising candidates for this application.[1, 2] The challenge for aqueous batteries is the narrow electrochemical stability window of water (thermodynamically 1.23 V at 25 °C), which limits their energy density. In recent reports, very high salt concentrations were shown to extend the narrow electrochemical stability window of water beyond 1.5 V.[3-6] The following mechanisms were proposed to explain the enhanced electrochemical stability of highly concentrated aqueous electrolytes: (i) Overpotentials towards water electrolysis are imposed by the low mobility and concentration of water in highly concentrated electrolytes, (ii) the cathode surface is blocked by bulky anions resulting in additional overpotentials for water oxidation, and (iii) in certain systems a solid-electrolyte interphase (SEI) is formed on the anode which suppresses water reduction during subsequent battery cycling.[3-

[5, 7] As this SEI is predominantly derived from anion reduction products,[3, 8] the chemical nature of the anion(s) present in the electrolyte is of key importance for the SEI formation ability of the electrolyte.

In a pioneering study, the bis(trifluoromethanesulfonyl)imide (TFSI) anion was identified to possess such SEI-forming properties at very high salt concentration.[3] LiTFSI, the lithium salt of the TFSI anion, has a very high solubility in water (21 mol kg^{-1} (21m) at 25 °C). In combination with the high oxidative stability of TFSI, the 21m aqueous solution of LiTFSI became the first example of a new generation of aqueous electrolytes with enhanced electrochemical stability.[3] These electrolytes are also called water-in-salt electrolytes as the salt fraction in the solution exceeds the water fraction by both weight and volume. The discovery of the water-in-salt approach has subsequently spurred research on a variety of chemistries based on this principle.[5, 6, 9-16]

Considering the often significantly lower cost of sodium salts and the high salt concentration of water-in-salt electrolytes, it appears particularly interesting to develop a water-in-salt electrolyte for sodium-ion batteries. However, it has proven difficult to develop such electrolytes due to the typically lower solubility of the sodium analogues of the lithium salts that are known to form water-in-salt electrolytes. For example, NaTFSI has a room temperature solubility of only 8m. We found that this concentration is too low to approach the wide electrochemical stability window of e.g. 21m LiTFSI.[17] Interestingly, SEI-forming ability and hence a wide electrochemical stability window were reported for 9m sodium trifluoromethanesulfonate (NaOTf).[10] However, it can be expected that the lithium analogue of this electrolyte still offers a more extended electrochemical stability window near its solubility limit of ~22m at 25 °C.[9]

The rare exception of a sodium salt of the bis(fluoro(alkyl)sulfonyl)imide type with sufficiently high solubility to enable high electrochemical stability is sodium bis(fluorosulfonylimide) (NaFSI). In fact, we found that the stability window of highly concentrated NaFSI electrolytes is comparable to that of typical lithium-ion water-in-salt electrolytes.[6] However, concerns have been raised as to the chemical stability of the FSI anion against hydrolysis.[18]

Here, we study the chemical stability of NaFSI and LiFSI aqueous solutions of various concentrations. We find that the cation has a large influence on the stability of FSI-based solutions. Furthermore, we determine key physicochemical properties of LiFSI and NaFSI aqueous solutions including conductivity, viscosity, and electrochemical stability.

5.2 Results and Discussion

Considering the relative weakness of S-F bonds (tabulated bond dissociation energy: 344 kJ mol^{-1}) present in FSI compared to C-F bonds (tabulated as 514 kJ mol^{-1}) present in TFSI, a stronger tendency of FSI towards hydrolysis can be expected.[19] These values should only be compared qualitatively as the sulfur atom in FSI is part of a larger conjugated unit. To study the chemical stability of FSI in aqueous environments, we prepared LiFSI and NaFSI aqueous solutions in a broad concentration range (1m, 5m, 10m, 15m, 20m, 25m, 30m, 35m) and monitored optical appearance, pH, and fluoride content of sealed samples during storage at 30 and 60 °C.

At 30 °C, no change in appearance is observed upon weekly visual inspection of the solutions during storage for four weeks. We only observe the formation of small amounts of a white precipitate for the highly concentrated LiFSI solutions (30m and 35m). After three months however, we observe a color change and the presence of larger amounts of a white precipitate for the 30m and 35m LiFSI solutions, while still no change in appearance is observed for the NaFSI solutions (**Figure 5-1a-b**).

A more marked difference between the LiFSI and NaFSI solutions is observed in the evolution of the pH (see **Figure 5-1c-d**). To distinguish between data points overlapping in the figures, all pH values are also listed in **Table 5-1**. Prior to the start of the experiment, we adjusted the pH of all solutions to a value of ~6, as battery electrodes tend to be most stable in neutral electrolytes. After four weeks, the pH of the highly concentrated LiFSI samples drastically decreases to values of ≤1. pH values of <1 cannot be distinguished from a value of 1 with the pH paper used for this experiment. Interestingly, the pH only decreases slightly to values between 4 and 5 for the NaFSI solutions. This shows that the cation has a strong influence on the stability of FSI.

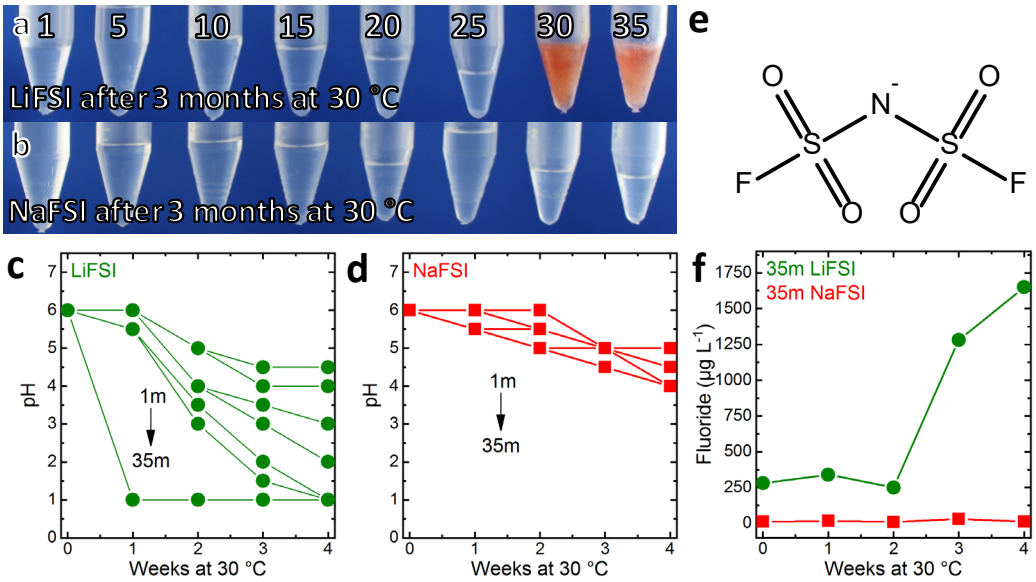

Figure 5-1 (a,b) Photographs of polypropylene vials containing aqueous solutions of (a) LiFSI and (b) NaFSI of various concentrations after storage at 30 °C for 3 months. The numbers on top of figure (a) correspond to the initial molality of the solutions in moles of salt per kilogram of water. (c,d) Evolution of the pH of (c) LiFSI and (d) NaFSI aqueous solutions of various concentrations during storage at 30 °C. (e) Chemical structure of the FSI anion. (f) Evolution of the fluoride content of 35m LiFSI and 35m NaFSI during storage at 30 °C.

Hydrolysis of FSI is expected to result in the formation of F^-/HF and sulfonic acids (e.g. via $[FSO_2NSO_2F]^- + H_2O$ ➔ HF + $[FSO_2NSO_3H]^-$ or related reactions). Hence, we measured the evolution of the fluoride content of the 35m samples, which showed the most rapid change in pH (see **Figure 5-1f).** Confirming the previous results, the fluoride content remains much more stable for the NaFSI than for the LiFSI sample. After four weeks, we measured a more than 100 times higher fluoride content for the LiFSI sample compared to the NaFSI sample. However, this difference in fluoride content of two orders of magnitude was still smaller than expected from the difference in pH of at least three orders of magnitude (see again **Figure 5-1c–d**). Given the low solubility of LiF in water of only 0.05m at 30 °C[20] and the high concentration of lithium cations in the examined solutions, the solubility product of LiF was likely exceeded during the experiment. Hence, we ascribe the white precipitate forming in the LiFSI samples at least in part to LiF. As HF is only a weak acid (pK_a = 3.2),[21] the low pH of ≤1 reached for the highly concentrated LiFSI solutions during storage at 30 °C supports the reaction mechanism stated above that involves the formation of sulfonic acids, which are much stronger acids (e.g. pK_a = -1.9 for methanesulfonic acid).[22]

At 60 °C, we observed a white precipitate after one week for LiFSI samples with a concentration of >5m. The 20m and 25m samples show an additional brown discoloration (**Figure 5-2a**), whereas the decomposition reaction proceeded more rapidly for the 30m and 35m samples as evidenced by the color change of the polypropylene container to dark brown and

more precipitation of the white residue. In contrast, all NaFSI samples remained unchanged in appearance upon visual inspection during storage for four weeks (see **Figure 5-2b**). However, at this temperature the pH of all NaFSI solutions, except of the one with a concentration of 1m, also dropped to a value of ≤1 after four weeks (**Figure 5-2c-d** and **Table 5-2**).

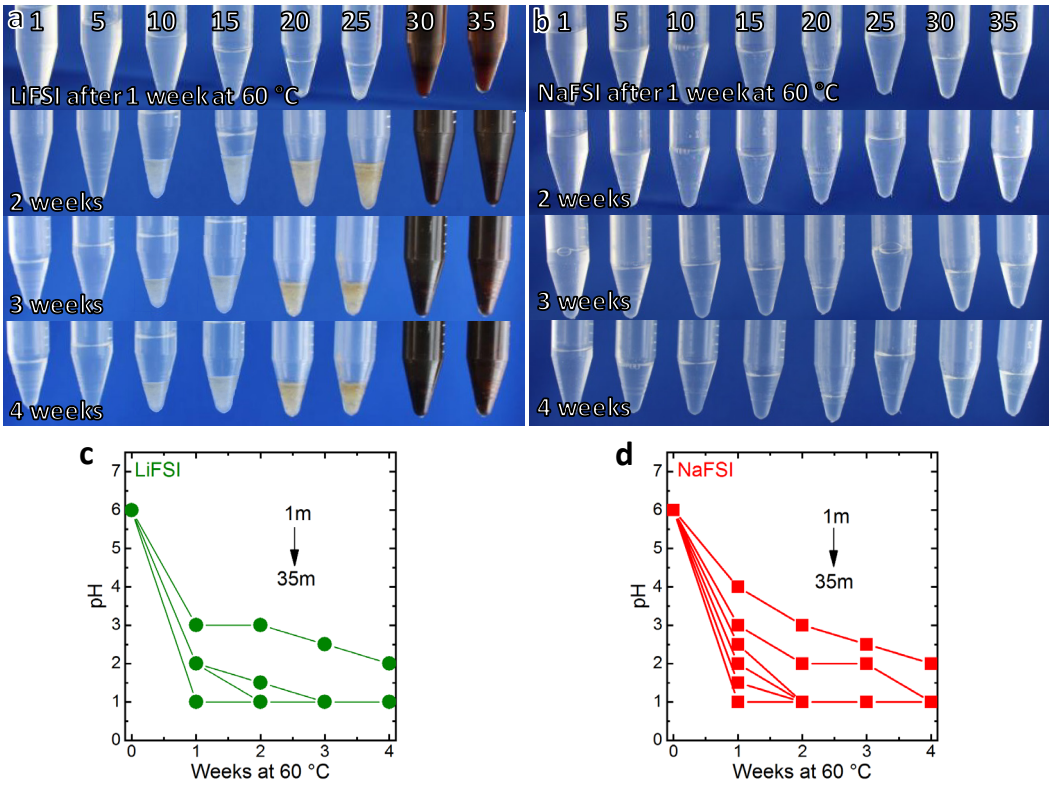

Figure 5-2 (a,b) Photographs of polypropylene vials containing (a) LiFSI and (b) NaFSI aqueous solutions of various concentrations during storage at 60 °C. The numbers on top of figures (a) and (b) correspond to the initial molality of the solution in moles of salt per kilogram of water. (c,d) Evolution of the pH of (c) LiFSI and (d) NaFSI aqueous solutions of various concentrations during storage at 60 °C.

Our results clearly show that NaFSI solutions are chemically much more stable than LiFSI solutions. Combined with the observed trend of reduced chemical stability with increasing concentration, we conclude that anion-cation interactions are very important for the stability of FSI anions in aqueous solution. This finding is in line with the result of DFT calculations for the LiTFSI-H_2O system that suggest that the strong interaction between Li^+ and TFSI anions at very high concentration, i.e. when the water-to-cation ratio is too low for water to fully solvate Li^+, reduces the stability of TFSI anions against reduction.[3] For LiTFSI-based electrolytes, it was reported that water-rich and anion-rich domains exist at high concentration.[23] If the same holds true for highly concentrated FSI-based electrolytes, we expect the destabilization of the FSI anions to be more pronounced in the anion-rich domains.

Na^+ has a lower charge density than Li^+ and hence the Coulomb interaction between FSI anions and Na^+ can be expected to be weaker than in the case of Li^+. This is indeed the case as shown in **Figure 5-3** by the larger peak shift of the S-N-S vibrational mode of FSI towards higher

wavenumbers for the LiFSI compared to the NaFSI solutions when increasing the concentration from 1m to 35m. Upon anion-cation interaction, withdrawal of charge through the oxygen atoms of the anion results in strengthened F-S and S-N bonds, leading to a higher frequency of the corresponding vibrational modes.[24] The S-N-S mode has been shown to be particularly sensitive to the strength of the cation-anion interaction.[25-27]

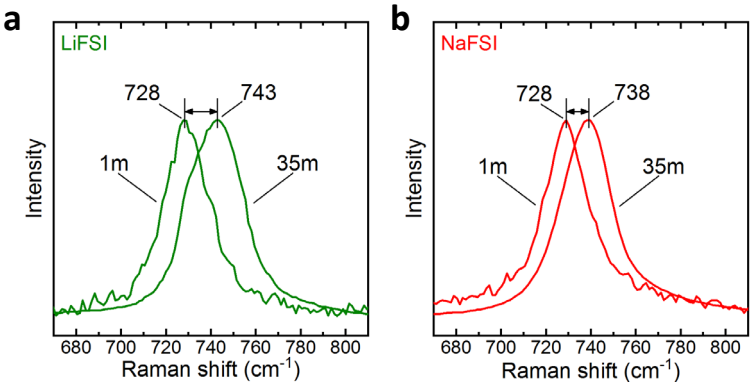

Figure 5-3 Raman spectra of 1m and 35m (a) LiFSI and (b) NaFSI aqueous solutions in the wavenumber region corresponding to the S-N-S vibrational mode of the FSI anion. The spectra have been normalized in order to better compare the significantly weaker signals of the 1m solutions with those of the 35m samples.

A somewhat different result has been recently reported for two TFSI-containing aqueous solutions: Faster degradation of TFSI anions during storage at 120 °C for 12 h was observed for 0.1 mol L^{-1} KTFSI in 3 mol L^{-1} KOH compared to 0.1 mol L^{-1} LiTFSI in 3 mol L^{-1} LiOH. However, these results are not directly comparable to ours as the pH of these solutions is much higher than the initial pH of our solutions. Furthermore, the Li^+/Na^+ solvation sheaths are FSI-rich in the case of our highly concentrated FSI solutions, while they can only contain little TFSI in the case of these hydroxide solutions. In our case, the cation with the higher charge density, Li^+, likely leads to faster hydrolysis of FSI through a stronger Coulomb interaction compared to Na^+, increasing the relative electrophilicity of FSI. In contrast, it can be expected that the stronger interaction between OH^- and Li^+ compared to K^+, which has a much lower charge density, results in a weaker nucleophilicity of the hydroxide anions and hence slower TFSI degradation kinetics.[8]

Besides the difference in charge density between Li^+ and Na^+, the lower solubility of LiF in water (0.05m) compared to NaF (1m) represents an additional factor for the faster degradation of LiFSI-based solutions.[20] Precipitation of LiF, as observed particularly at 60 °C (see **Figure 5-2a**), shifts the hydrolysis reaction formulated above to the product side due to removal of F^- ions.

Conductivity and viscosity of LiFSI and NaFSI solutions with different concentrations measured at 25 °C are shown in **Figure 5-4a** and **b**, respectively**.** The conductivity of the NaFSI solutions is slightly higher than for LiFSI for the lower concentrations. This can be explained by the smaller effective radius of hydrated Na^+ compared to Li^+ in aqueous solutions, resulting in higher mobility of the former.[28, 29] For both cations, the conductivity goes through a maximum around 5m. Due to the relatively small size of the FSI anion, the conductivity is much higher than that of TFSI-based electrolytes. For example, both 20m solutions have a conductivity of >30 mS cm^{-1} compared to ~10 mS cm^{-1} for 21m LiTFSI.[3] **Figure 5-4b** shows the corresponding increase in viscosity with increasing concentration.

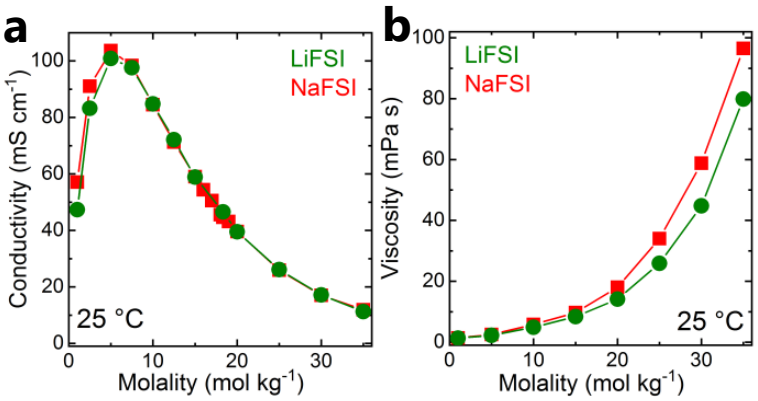

Figure 5-4 (a) Conductivity and (b) viscosity at 25 °C of LiFSI and NaFSI solutions over the whole investigated concentration range.

Conductivity and viscosity over a wide temperature range are reported in **Figure 5-6**. At high temperatures, the viscosity of the highly concentrated NaFSI solutions is slightly lower than for LiFSI, whereas at and below room temperature the trend is reversed (**Figure 5-6c-d)**. In the Arrhenius plots of the conductivity data, see **Figure 5-7**, it can be seen that the deviation from purely exponential Arrhenius behavior is more pronounced for >20m NaFSI solutions than for the LiFSI analogues. The temperature-dependence of the conductivity data is well described by the Vogel-Tammann-Fulcher (VTF) equation ($\sigma = A \times \exp(-B/(T - T_0))$)[30] for both electrolyte series; see curves in **Figure 5-7**. The corresponding VTF parameters are listed in **Table 5-3**.

Raman spectra in the wavenumber region corresponding to the OH stretching vibrations of water are established simple probes to assess the electrochemical stability of aqueous electrolytes: While water displays a broad signal in this wavenumber region, the signature of aqueous electrolytes with enhanced electrochemical stability is a relatively narrow peak at ~3550 cm^{-1}.[5] **Figure 5-5a-b** shows the Raman spectra in this wavenumber region for the investigated LiFSI and NaFSI solutions. Narrowing of the initially broad signal and emergence of a peak at

~3550 cm^{-1} can be clearly seen for both electrolyte series when increasing the concentration, indicating increasing electrochemical stability. In line with the lower charge density of Na^+, a higher NaFSI concentration is apparently needed to have the same effect on the electrolyte structure as for LiFSI-based electrolytes.

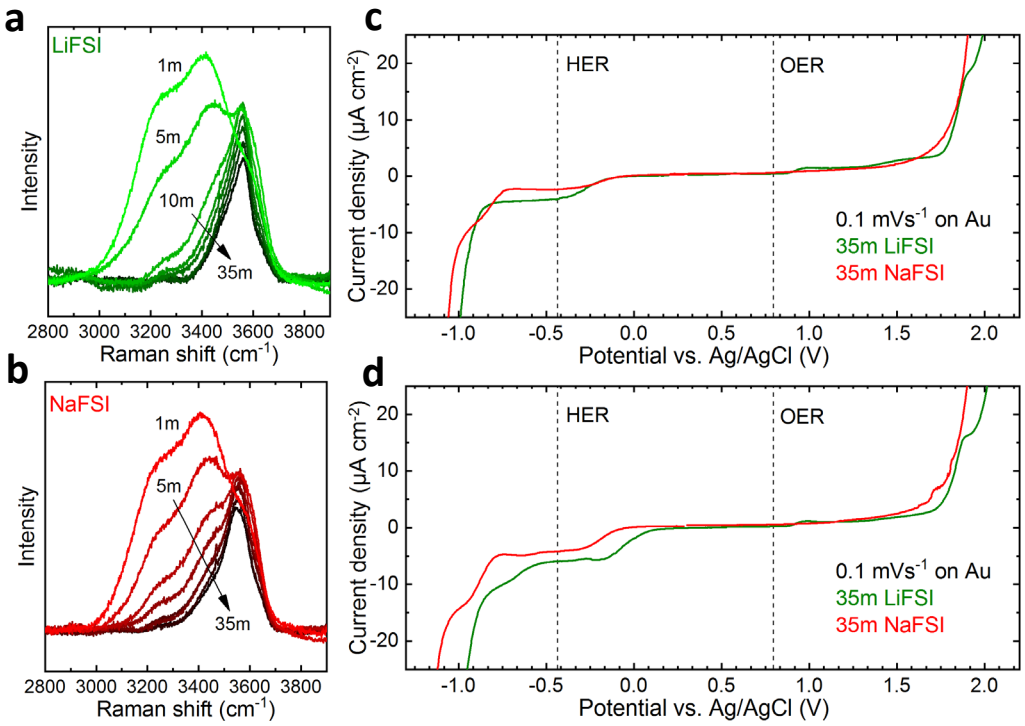

Figure 5-5 (a,b) Raman spectra in the wavenumber region corresponding to the OH stretching modes of water of (a) LiFSI and (b) NaFSI aqueous solutions of various concentrations (1m, 5m, 10m, 15m, 20m, 25m, 30m, and 35m). (c) Linear sweep voltammograms of freshly prepared and (d) one week old 35m LiFSI and NaFSI aqueous solutions on gold electrodes. The thermodynamic potentials for the hydrogen (HER) and oxygen evolution (OER) reactions at pH=6 are indicated by dashed vertical lines.

The voltammograms of the 35m LiFSI and NaFSI solutions recorded using gold working electrodes (see **Figure 5-5c**) confirm that these solutions possess wide electrochemical stability windows as indicated by the Raman spectra. For a cut-off current density of 5 µA cm^{-2}, both electrolytes display a stability window of ~2.5 V, with the window being somewhat wider for the Li-based electrolyte. We ascribe the plateau between ca. -0.3 V and -0.8 V vs. Ag/AgCl to anion decomposition and potentially SEI formation as suggested for 21m LiTFSI, the original water-in-salt electrolyte.[3] In line with the observed higher chemical stability of NaFSI compared to LiFSI aqueous solutions, the plateau current is lower for the Na-based electrolyte. We note that recent studies for TFSI-based highly concentrated aqueous electrolytes question the hypothesis of SEI formation through *electrochemical* reduction of imide anions. [8, 31] Instead, an alternative *chemical* mechanism is proposed that requires the initial formation of particularly reactive hydroxide anions as a byproduct of the hydrogen evolution reaction that then undergo a nucleophilic attack of TFSI anions.[8] Considering the difference in chemical

stability between FSI and TFSI anions in aqueous solution, SEI formation might also be different for the two systems. However, a detailed analysis of potential SEI formation in FSI-based water-in-salt electrolytes is beyond the scope of this study.

After storage of the electrolytes at 30 °C for just one week, the reductive stability of 35m LiFSI is already significantly reduced as expected from the drop in pH reported above (see **Figure 5-5d**). In contrast, the 35m NaFSI electrolyte appears again much more stable.

5.3 Conclusions

In summary, we studied the chemical stability, conductivity, viscosity, and electrochemical stability of LiFSI and NaFSI aqueous solutions over a broad concentration range. While our results show that FSI is prone to hydrolysis in both LiFSI and NaFSI solutions, the latter appear to be significantly more stable, highlighting the important role of the cation. Due to the small size of the FSI anion, both 20m solutions retain a high conductivity of >30 mS cm^{-1} at 25 °C. In our opinion, NaFSI-based aqueous electrolytes can play a role in the development of novel high-voltage sodium-ion batteries. However, considering that particularly at elevated temperatures NaFSI solutions are still prone to rapid acidification, further efforts are needed to develop a highly soluble sodium salt with excellent oxidative stability that is stable against hydrolysis and ideally also has SEI-forming capabilities to enable long cycle and calendar life in batteries.

5.4 Methods

Samples were prepared by dissolving LiFSI (battery grade, Fluorochem) or NaFSI (99.7%, Solvionic) in high-purity water (Millipore Milli-Q, degassed with Ar). Using lithium or sodium hydroxide solutions, the initial pH of the electrolytes was adjusted to a value of ~6. The approximate pH of the solutions was determined using pH paper (Merck, pH1-14 universal indicator). Due to the very high salt concentration of some samples and the possible presence of HF, a standard pH electrode was not employed.

Ionic conductivity was determined via impedance spectroscopy (Bio-Logic MCS 10) in sealed 2-electrode cells equipped with Pt electrodes (Bio-Logic HTCC). Viscosity was determined with an electromagnetically spinning viscometer (Kyoto Electronics Manufacturing EMS-1000) using 2 mm Al spheres. Sample volumes of 400 µL were used. The samples were equilibrated for 15 min at each temperature. Raman spectra were collected at room temperature from samples sealed in NMR tubes (Renishaw Ramascope equipped with a 50 mW laser with a wavelength of 633 nm). Linear sweep voltammetry was carried out with a gold working electrode with a diameter of 1 mm (eDAQ) in a small volume glass cell (eDAQ) at 30 °C. A miniature Ag/AgCl electrode (eDAQ) was used as reference electrode and a Pt-coated Ti rod

(eDAQ) served as counter electrode. The electrolyte volume was ca. 600 µL and the scan rate was set to 0.1 mV s^{-1}. The working electrode potential was scanned from the open circuit potential until a current density of ±1.5 mA cm^{-2} was reached. Separate experiments were carried out to determine the cathodic and anodic stability.

Electrolyte samples were sealed in polypropylene tubes and stored at 30 or 60 °C. In one week intervals, the approximate pH of the samples was determined as described above and photographs of the samples were taken. Additionally, small samples were taken every week to determine the fluoride content via ion chromatography with a Metrohm 882 Compact IC Plus equipped with a conductivity detector. After dilution with high-purity water to 1:120, these samples were stored at 4 °C and measured together after all samples were collected. For the measurements, the samples were further diluted to 1:600 and 1:1200 with deionized water and filtered through a 0.45 µm membrane filter. The injection volume was 20 µL. The measurement of fluoride was performed isocratically with an eluent aqueous solution containing 3.2 mM Na_2CO_3 and 1.0 mM $NaHCO_3$. The separation was carried out on a Metrosep A Supp 5-250/4.0 column. The flow rate was 0.7 mL min^{-1}. For the quantification, an external five-point calibration ($R^2 > 0.9999$) was carried out using standard solutions (IC Calibration mix R7, ROMIL Ltd) in a range of 0.2 to 1.6 µg mL^{-1}.

5.5 Supporting Information

Table 5-1 Evolution of the pH of (a) LiFSI and (b) NaFSI aqueous electrolytes during storage at 30 °C as shown in Figure 5-1.

a, LiFSI 30 °C	1m	5m	10m	15m	20m	25m	30m	35m
Fresh	6	6	6	6	6	6	6	6
1 week	6	6	6	6	5.5	5.5	1	1
2 weeks	5	5	4	4	3.5	3	1	1
3 weeks	4.5	4	3.5	3	2	1.5	1	1
4 weeks	4.5	4	3	2	1	1	1	1

b, NaFSI 30 °C	1m	5m	10m	15m	20m	25m	30m	35m
Fresh	6	6	6	6	6	6	6	6
1 week	6	6	5.5	5.5	5.5	5.5	5.5	5.5
2 weeks	5.5	6	5	5.5	5.5	5	5	5
3 weeks	5	5	4.5	5	5	5	5	5
4 weeks	5	4	4	4	4	4.5	4	5

Table 5-2 Evolution of the pH of (a) LiFSI and (b) NaFSI aqueous electrolytes during storage at 60 °C as shown in Figure 5-2.

a, LiFSI 60 °C	1m	5m	10m	15m	20m	25m	30m	35m
Fresh	6	6	6	6	6	6	6	6
1 week	3	2	2	1	1	1	1	1
2 weeks	3	1.5	1	1	1	1	1	1
3 weeks	2.5	1	1	1	1	1	1	1
4 weeks	2	1	1	1	1	1	1	1

b, NaFSI 60 °C	1m	5m	10m	15m	20m	25m	30m	35m
Fresh	6	6	6	6	6	6	6	6
1 week	4	3	3	2.5	2	1.5	1	1
2 weeks	3	2	2	1	1	1	1	1
3 weeks	2.5	2	2	1	1	1	1	1
4 weeks	2	1	1	1	1	1	1	1

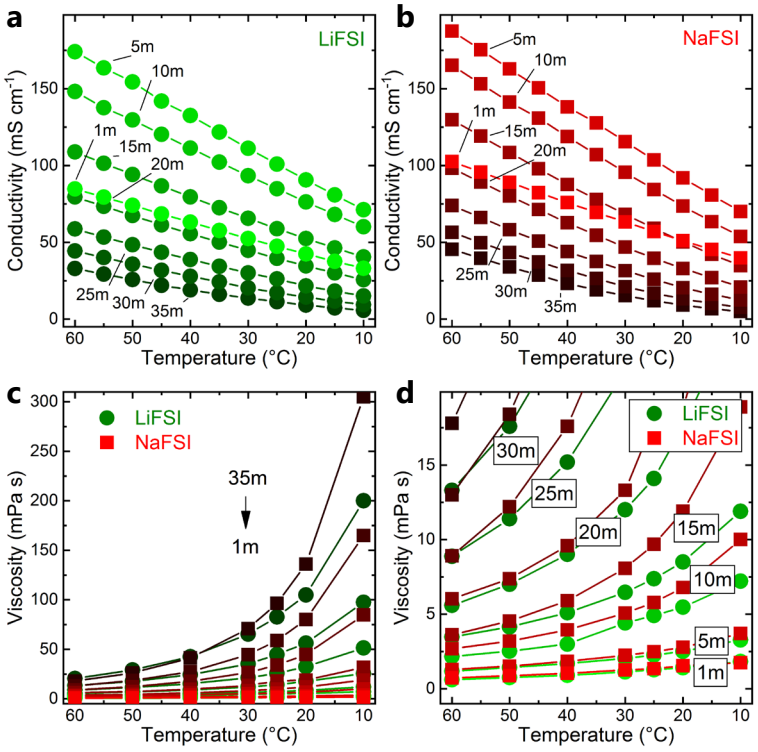

Figure 5-6 (a,b) Conductivity and (c,d) viscosity of (a,c,d) LiFSI and (b,c,d) NaFSI aqueous solutions of various concentrations.

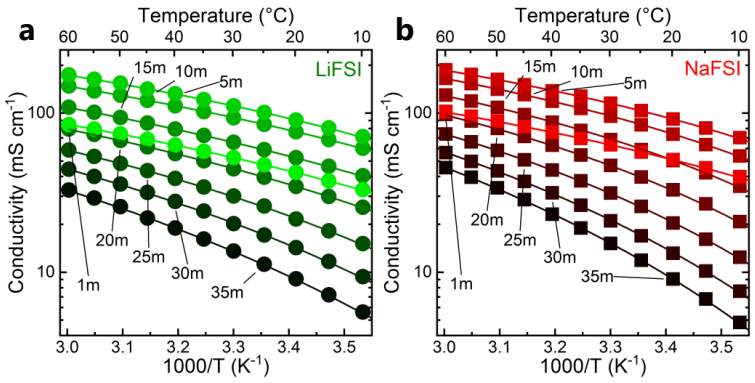

Figure 5-7 Arrhenius plots of the conductivity data of (a) LiFSI and (b) NaFSI aqueous solutions of various concentrations. The curves connecting the data points have been generated based on the best VTF fits.

Table 5-3 VTF parameters including the coefficient of determination (R^2) for the conductivity of (a) LiFSI and (b) NaFSI electrolytes over the whole concentration range.

a, LiFSI	T_0 (K)	A (S cm^{-1})	B (K)	R^2
1m	178	0.621	309	0.9999
5m	192	0.890	231	0.9998
10m	181	0.923	279	0.9999
15m	175	0.925	339	0.9999
20m	184	0.748	335	0.9999
25m	194	0.662	338	0.9998
30m	191	0.799	411	0.9998
35m	187	0.986	498	0.9999

b, NaFSI	T_0 (K)	A (S cm^{-1})	B (K)	R^2
1m	184	0.664	280	0.9998
5m	200	0.956	218	0.9998
10m	204	0.979	230	0.9999
15m	211	0.866	233	0.9996
20m	211	0.909	273	0.9999
25m	206	1.176	352	0.9999
30m	202	1.518	431	0.9998
35m	199	2.011	508	0.9999

References

1. Palomares, V., et al., *Na-ion batteries, recent advances and present challenges to become low cost energy storage systems.* Energy Environ. Sci., 2012. **5**(3): p. 5884-5901.
2. Pan, H., Y.-S. Hu, and L. Chen, *Room-temperature stationary sodium-ion batteries for large-scale electric energy storage.* Energy Environ. Sci., 2013. **6**(8): p. 2338-2360.
3. Suo, L., et al., *"Water-in-salt" electrolyte enables high-voltage aqueous lithium-ion chemistries.* Science, 2015. **350**(6263): p. 938-43.
4. Suo, L., et al., *How solid-electrolyte interphase forms in aqueous electrolytes.* J. Am. Chem. Soc., 2017. **139**(51): p. 18670-18680.
5. Yamada, Y., et al., *Hydrate-melt electrolytes for high-energy-density aqueous batteries.* Nat. Energy, 2016. **1**: p. 16129.
6. Kühnel, R.-S., D. Reber, and C. Battaglia, *A High-Voltage Aqueous Electrolyte for Sodium-Ion Batteries.* ACS Energy Lett., 2017. **2**(9): p. 2005-2006.
7. Vatamanu, J. and O. Borodin, *Ramifications of water-in-salt interfacial structure at charged electrodes for electrolyte electrochemical stability.* J. Phys. Chem. Lett., 2017. **8**(18): p. 4362-4367.
8. Dubouis, N., et al., *The role of the hydrogen evolution reaction in the solid–electrolyte interphase formation mechanism for "Water-in-Salt" electrolytes.* Energy & Environmental Science, 2018. **11**(12): p. 3491-3499.
9. Suo, L., et al., *Advanced High-Voltage Aqueous Lithium-Ion Battery Enabled by "Water-in-Bisalt" Electrolyte.* Angew. Chem. Int. Ed., 2016. **55**(25): p. 7136-7141.
10. Suo, L., et al., *"Water-in-Salt" Electrolyte Makes Aqueous Sodium-Ion Battery Safe, Green, and Long-Lasting.* Adv. Energy Mater., 2017. **7**(21): p. 1701189.
11. Yang, C., et al., *4.0 V Aqueous Li-Ion Batteries.* Joule, 2017. **1**(1): p. 122-132.
12. Wang, F., et al., *Stabilizing high voltage $LiCoO_2$ cathode in aqueous electrolyte with interphase-forming additive.* Energy Environ. Sci., 2016. **9**(12): p. 3666-3673.
13. Leonard, D.P., et al., *Water-in-Salt Electrolyte for Potassium-Ion Batteries.* ACS Energy Lett., 2018. **3**(2): p. 373-374.
14. Lukatskaya, M.R., et al., *Concentrated mixed cation acetate "water-in-salt" solutions as green and low-cost high voltage electrolytes for aqueous batteries.* Energy Environ. Sci., 2018. **11**(10): p. 2876-2883.
15. Wang, F., et al., *Highly reversible zinc metal anode for aqueous batteries.* Nat. Mater., 2018. **17**(6): p. 543.
16. Zhang, N., et al., *Rechargeable aqueous zinc-manganese dioxide batteries with high energy and power densities.* Nat. Commun., 2017. **8**(1): p. 405.
17. Reber, D., R.-S. Kühnel, and C. Battaglia, *High-voltage aqueous supercapacitors based on NaTFSI.* Sustainable Energy Fuels, 2017. **1**(10): p. 2155-2161.
18. Bin, D., et al., *Progress in Aqueous Rechargeable Sodium-Ion Batteries.* Adv. Energy Mater., 2018. **8**(17): p. 1703008.
19. Rumble, J.R., ed., *CRC Handbook of Chemistry and Physics, 99th Edition (Internet Version 2018)*. Boca Raton: CRC Press/Taylor & Francis.

20. Payne, J.H., *The solubility of lithium and sodium fluorides.* J. Am. Chem. Soc., 1937. **59**(5): p. 947-947.

21. Ellis, A.J., *The effect of temperature on the ionization of hydrofluoric acid.* J. Chem Soc., 1963(0): p. 4300-4304.

22. Guthrie, J.P., *Hydrolysis of esters of oxy acids: pKa values for strong acids; Brønsted relationship for attack of water at methyl; free energies of hydrolysis of esters of oxy acids; and a linear relationship between free energy of hydrolysis and pKa holding over a range of 20pK units.* Can. J. Chem., 1978. **56**(17): p. 2342-2354.

23. Borodin, O., et al., *Liquid structure with nano-heterogeneity promotes cationic transport in concentrated electrolytes.* ACS Nano, 2017. **11**(10): p. 10462-10471.

24. Beran, M., et al., *A new route to the syntheses of alkali metal bis (fluorosulfuryl) imides: Crystal structure of $LiN(SO_2F)_2$.* Polyhedron, 2006. **25**(6): p. 1292-1298.

25. Bakker, A., et al., *Contact ion pair formation and ether oxygen coordination in the polymer electrolytes $M[N(CF_3SO_2)_2]_2PEO_n$ for M= Mg, Ca, Sr and Ba.* Polymer, 1995. **36**(23): p. 4371-4378.

26. Herstedt, M., et al., *Spectroscopic characterization of the conformational states of the bis(trifluoromethanesulfonyl) imide anion ($TFSI^-$).* J. Raman Spectrosc., 2005. **36**(8): p. 762-770.

27. Boschin, A. and P. Johansson, *Characterization of NaX (X: TFSI, FSI)–PEO based solid polymer electrolytes for sodium batteries.* Electrochim. Acta, 2015. **175**: p. 124-133.

28. Mosqueda, H., et al., *Electrolytes for hybrid carbon–MnO_2 electrochemical capacitors.* Electrochim. Acta, 2010. **55**(25): p. 7479-7483.

29. Nightingale Jr., E.R., *Phenomenological theory of ion solvation. Effective radii of hydrated ions.* J. Phys. Chem., 1959. **63**(9): p. 1381-1387.

30. Fulcher, G.S., *Analysis of recent measurements of the viscosity of glasses.* J. Am. Ceram. Soc., 1925. **8**(6): p. 339-355.

31. Coustan, L., K. Zaghib, and D. Bélanger, *New insight in the electrochemical behaviour of stainless steel electrode in water-in-salt electrolyte.* J. Power Sources, 2018. **399**: p. 299-303.

6 Suppressing Crystallization of Water-in-Salt Electrolytes by Asymmetric Anions Enables Low-Temperature Operation of High-Voltage Aqueous Batteries

David Reber,[1,2] Ruben-Simon Kühnel,[1] and Corsin Battaglia[1]

[1]Laboratory Materials for Energy Conversion, Swiss Federal Laboratories for Materials Science and Technology, Empa, Überlandstrasse 129, 8600 Dübendorf, Switzerland

[2]Institut des Matériaux, École Polytechnique Fédérale de Lausanne, EPFL, Station 12, 1015 Lausanne, Switzerland

ACS Materials Letters, 2019, 1, 44-51

DOI: 10.1021/acsmaterialslett.9b00043

https://pubs.acs.org/doi/abs/10.1021/acsmaterialslett.9b00043

In this study, we show that a key factor limiting the applicability of water-in-salt electrolytes is their tendency to crystallize near room temperature. We demonstrate that asymmetric anions can suppress the crystallization and demonstrate this approach with a 2 V class aqueous sodium-ion battery with excellent cycling stability from -10 to 30 °C. **Author contributions:** D.R., R.-S.K., C.B. conceived the idea for this study. R.-S.K. identified NaFTFSI as a promising salt. D.R. and R.-S.K. designed most experiments. D.R. carried out the experiments. D.R., R.-S.K., C.B. analyzed the data. D.R. prepared the figures and wrote the original draft of the manuscript. R.-S.K. and C.B. critically reviewed and edited the manuscript. All coauthors read and approved the final manuscript.

Abstract

The discovery of enhanced electrochemical stability for aqueous electrolytes with very high salt concentration has stimulated the development of high-voltage aqueous batteries. We show that a key factor limiting the applicability of these batteries is the tendency of highly concentrated electrolytes to crystallize near room temperature, leading to cell failure. Here we report the use of asymmetric anions as solution to suppress the crystallization of highly concentrated aqueous electrolytes. We demonstrate this approach with a ternary sodium-ion electrolyte that we employ in a 2 V class aqueous sodium-ion battery based on a $NaTi_2(PO_4)_3$ anode and a $Na_3(VOPO_4)_2F$ cathode. This cell displays excellent cycling stability at 30 °C with capacity retention of 85% after 100 cycles at C/5 and 77% after 500 cycles at 1C. The cell reaches a specific energy of 64 Wh kg^{-1} based on the active masses of both electrodes, twice as high as previously reported for this electrode couple. Further, the cell can be operated down to temperatures of at least -10 °C, with capacity retention of 74% after 500 cycles at C/5.

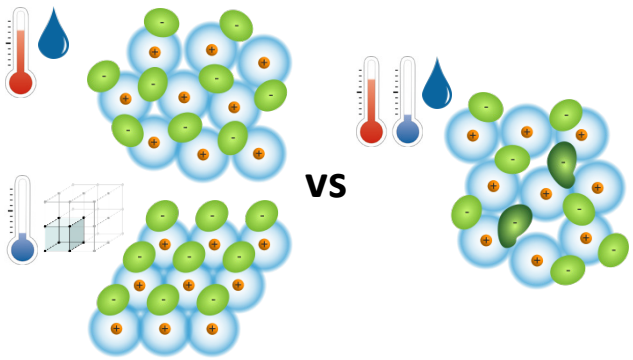

6.1 Introduction

The major challenge for batteries employing non-flammable aqueous electrolytes is the narrow electrochemical stability window (ESW) of water of 1.23 V at 25 °C, which limits the maximum cell voltage due to the onset of water electrolysis. For comparison, lithium-ion batteries employing flammable organic electrolytes operate at an average nominal cell voltage of typically 3.7 V. Employing very high salt concentration is a promising recent approach to widen the electrochemical stability window of aqueous electrolytes.[1-3] This so-called water-in-salt approach extends in particular the oxidative stability substantially, enabling reversible cycling of high-voltage cathode materials in aqueous lithium-, sodium-, potassium-, and zinc-ion batteries.[4-11]

Here, we show that previously reported water-in-salt electrolytes, operating near the salt solubility limit, appear stable for a prolonged period of time, but have a tendency to (partially) crystallize during long-term cycling in a battery, causing cell failure. We further show that this problem can be addressed by the addition of salts with asymmetric anions, which extend the liquid state of water-in-salt electrolytes to lower temperatures. We demonstrate our approach for a water-in-salt electrolyte for sodium-ion batteries where we substitute a fraction of the 35 mol·kg^{-1} (35m) sodium bis(fluorosulfonyl)imide (NaFSI) with symmetric anions by sodium (fluorosulfonyl)(trifluoromethylsulfonyl)imide (NaFTFSI) with asymmetric anions (see **Figure 6-1a** for the chemical structures of the anions employed in this study). The concept is also demonstrated for the chemically less stable LiFSI system with LiFTFSI substitution. Furthermore, we developed a sodium-ion battery employing the mixed NaFSI/NaFTFSI electrolyte in combination with a $NaTi_2(PO_4)_3$ anode and a $Na_3(VOPO_4)_2F$ cathode and report stable cycling down to temperatures of -10 °C with excellent capacity retention and high energy density.

6.2 Results and Discussion

Differential scanning calorimetry (DSC) was used to probe the thermal behavior of various water-in-salt electrolytes. To start from a fully liquid state, all samples were initially equilibrated at 60 °C for 30 min. The cooling/heating rate was set to 1 °C·min^{-1} and a small amount of meso-carbon microbeads (MCMB) was added to all samples to provoke crystallization.[12]

In a first series of DSC experiments the following electrolytes were cooled from 60 to −120 °C and subsequently heated back to 60 °C: 21m lithium bis(trifluoromethylsulfonyl)imide (LiTFSI), the original water-in-salt electrolyte, 19.5m LiTFSI + 8.3m lithium bis(pentafluoroethylsulfonyl)imide (LiBETI), also called hydrate-melt electrolyte, and 35m NaFSI, the first sodium-ion water-in-salt electrolyte recently reported by us.[1-3] As shown in **Figure 6-1b**, all

three electrolytes undergo exothermic events during cooling that we assign to crystallization. During heating, the three electrolytes show sharp endothermic peaks at -9, -12, and -34 °C, respectively. We assign these events to eutectic melting based on the phase diagrams for the LiTFSI-H_2O system[13] and the NaFSI-H_2O system (mapped out in **Figure 6-6**). Liquidus transitions, corresponding to the transition to a fully liquid state, are observed at 23, 28, and 50 °C, respectively.

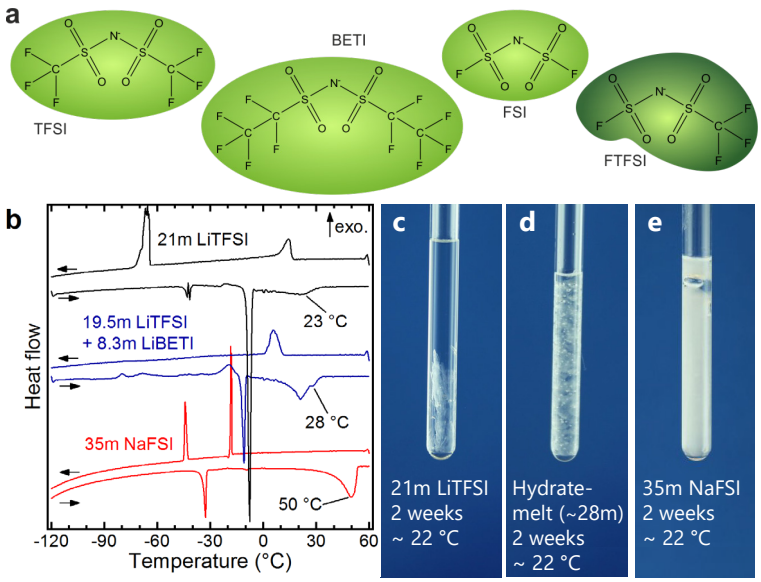

Figure 6-1 Thermal characterization of water-in-salt electrolytes. a, Structural formulas of the symmetric and asymmetric anions used in this study. ***b****, Differential scanning calorimetry curves of various water-in-salt electrolytes recorded during scans from 60 °C to -120 °C and back to 60 °C. All samples were mixed with a small amount of meso-carbon microbeads to provoke crystallization and all scan rates were set to 1 °C·min^{-1}.* ***c,d,e****, Photographs of (c) 21m LiTFSI, (d) 19.5m LiTFSI + 8.3 LiBETI (hydrate-melt), and (e) 35m NaFSI after storage at room temperature for two weeks.*

The liquidus temperature for all three electrolytes lies above 20 °C, which matches our observation of partial crystallization of these electrolytes during storage at room temperature. **Figure 6-1c-e** show typical photographs of the electrolytes after storage at ~22 °C for two weeks. Crystallization can be clearly seen for all electrolytes. The amount of crystallized salt visibly increases with increasing initial concentration of the solution in line with the phase diagrams. When using these electrolytes in batteries operated at room temperature, it must hence be expected that crystallization will lead to a reduction of salt concentration in the liquid phase. Consequently, the electrochemical stability window of the electrolyte will narrow, leading to accelerated water electrolysis. Hydrogen and/or oxygen evolution not only result in lower Coulombic efficiency, but also affect the (local) pH of the electrolyte, which can cause active material dissolution, leading to premature cell failure.[14, 15]

We find that adding a second asymmetric anion to water-in-salt electrolytes suppresses crystallization of the electrolyte at temperatures relevant for battery operation. To demonstrate this approach, we chose the asymmetric FTFSI anion as model system, which can be

described as being a hybrid between the symmetric TFSI and FSI anions (see again **Figure 6-1a**). We further chose to modify the 35m NaFSI solution as this electrolyte has the highest liquidus temperature among the investigated water-in-salt electrolytes. We prepared two mixed solutions, one containing 30m NaFSI and 5m NaFTFSI and one containing 25m NaFSI and 10m NaFTFSI. Mixed 35m NaFSI/NaFTFSI solutions with a higher NaFTFSI content could not be prepared due to the limited room temperature solubility of NaFTFSI (~19m).

We repeated the same DSC experiment as the one shown in **Figure 6-1b** for these mixed-anion electrolytes. Interestingly, the two mixed electrolytes do not show any crystallization event during the cooling scan (**Figure 6-2**), resulting in a vitreous state.[16] This observation is a first indication that the presence of asymmetric FTFSI anions hinders the crystallization of the electrolyte. During the heating scan, we observe the onset of a glass transition at -65 and -69 °C for the mixed electrolytes containing 5m and 10m NaFTFSI, respectively. The glass transition is followed by a cold crystallization event at -34 and -32 °C, where the quenched amorphous/vitreous structure becomes sufficiently mobile for crystallization to occur.[17, 18] Finally, the mixed electrolytes undergo a liquidus transition to a fully liquid state at 44 and 38 °C for 5m and 10m NaFTFSI, respectively. Hence, the presence of the second, asymmetric anion is an effective strategy to lower the liquidus temperature, albeit by only 6 and 12 °C, respectively. We expect that the liquidus temperature can be further lowered by the presence of a third anion as this would further increase the entropy of the system.

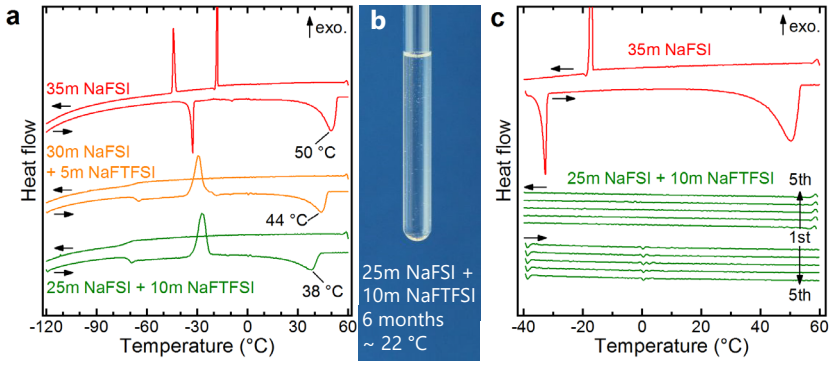

Figure 6-2 Impact of asymmetric anion on crystallization. a, DSC curves of 35m NaFSI and of mixed electrolytes containing symmetric FSI and asymmetric FTFSI anions recorded during scans from 60 °C to -120 °C and back to 60 °C. ***b****, Photograph of 25m NaFSI + 10m NaFTFSI after storage at room temperature for six months.* ***c****, DSC curve of 35m NaFSI and multiple scans for 25m NaFSI + 10m NaFTFSI between 60 °C and -40 °C.*

Remarkably, the 25m NaFSI + 10m NaFTFSI electrolyte has remained liquid at room temperature (~22 °C) ever since we prepared it more than six months ago (see **Figure 6-2b)** despite the higher liquidus temperature of 38 °C compared to e.g. 23 °C for the 21m LiTFSI electrolyte (see again **Figure 6-1b** and **c**), which crystallizes already after a few days at this temperature. This result is in line with our finding that no crystallization is observed for this electrolyte during the DSC cooling run down to -120 °C (see again **Figure 6-2a**) although we applied a low

scan rate of 1 °C·min^{-1}, which weakens the tendency towards supercooling[19, 20], and used a crystallization agent (MCMB). When we cycle the mixed FSI/FTFSI electrolyte in a temperature range more relevant for battery applications, between -40 and 60 °C (see **Figure 6-2c)**, we also observe no evidence of crystallization during heating. In contrast, the 35m NaFSI electrolyte (also shown in **Figure 6-2c**) shows the same behavior in this temperature range as in the extended temperature range. Furthermore, as shown below, full cells based on the mixed FSI/FTFSI electrolyte show stable charge/discharge cycling behavior down to at least -10 °C, while the 35m NaFSI electrolyte crystallizes in our full cells already at 30 °C. We hence conclude that the presence of the asymmetric FTFSI anions impedes the formation of long range order thereby effectively suppressing crystallization.[21] In other words, these mixed-anion electrolytes show particularly strong supercooling behavior, which has also been observed for other viscous liquids like ionic liquids.[22, 23]

To study the influence of the symmetry of the anion on the supercooling behavior, we prepared a second series of electrolytes based on 35m LiFSI. The higher room temperature solubility of LiTFSI (~20m)[13] compared to NaTFSI (~8m)[24] enables substitution of 10m of LiFSI either by LiFTFSI with asymmetric anions or by LiTFSI with symmetric anions, which is not possible for the NaFSI system. From the DSC experiments, a very similar reduction in liquidus temperature of ~6 °C is obtained for both mixed-anion electrolytes relative to 35m LiFSI (see **Figure 6-3a**). However, upon storage at 0 °C for four weeks, we observe crystallization only for the sample containing the symmetric TFSI anions, whereas the solution containing the asymmetric FTFSI anions remains liquid (see photographs in **Figure 6-3b** and **c**). These results demonstrate the effectiveness of asymmetric FTFSI anions in kinetically stabilizing water-in-salt electrolytes below the liquidus temperature. The mechanism by which the symmetry of the anions influences the crystallization kinetics is currently subject to further research via molecular dynamics simulations.

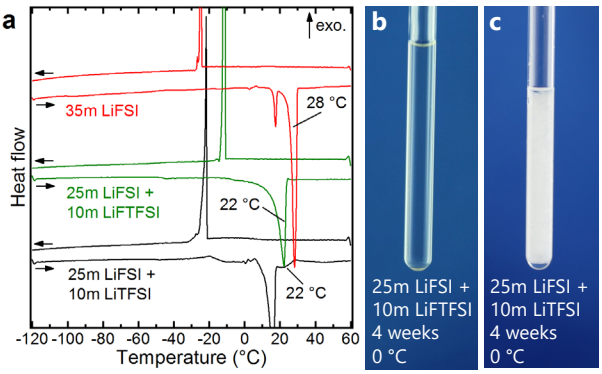

Figure 6-3 Comparison of the impact of the symmetry of the second anion. a, DSC curves of 35m LiFSI and mixed lithium electrolytes containing symmetric FSI and asymmetric FTFSI or symmetric TFSI anions, respectively, during scans from 60 °C to -120 °C and back to 60 °C. ***b-c****, Photographs of (b) 25m LiFSI + 10m LiFTFSI and (c) 25m LiFSI + 10m LiTFSI after storage at 0 °C for four weeks.*

As water-in-salt electrolytes for sodium-ion batteries are particularly attractive considering the high salt content of such electrolytes and the typically lower cost of sodium salts compared to lithium salts, we decided to focus on the NaFSI/NaFTFSI system for the remainder of this study.

Besides thermal properties, conductivity and electrochemical stability window are key properties of electrolytes for battery applications. The physicochemical properties of the NaFSI-based electrolytes, 35m NaFSI, 30m NaFSI + 5m NaFTFSI, and 25m NaFSI + 10m NaFTFSI, are summarized in **Table 6-1**. With increasing fraction of NaFTFSI, the viscosity increases from 75.8 to 94.2 mPa·s. The ionic conductivity follows the usual inverse trend, decreasing from 14.8 to 11.8 mS cm^{-1}. This correlates well with the larger size of the FTFSI compared to the FSI anion. The marginal reduction in density with increasing FTFSI content can also be explained by the larger, bulkier, and asymmetric FTFSI anions, which disturb dense ion packing. As seen from the Walden plot in **Figure 6-7**, all three electrolytes can be classified as superionic, meaning the ionic conductivity is decoupled from the viscosity. Such superionicity has been described for other water-in-salt electrolytes[2] and is further discussed in reference [25]. With a value of 11.8 mS cm^{-1} at 30 °C, the ionic conductivity of the mixed-anion electrolyte containing 25m NaFSI and 10m NaFTFSI is comparable to that of previously reported water-in-salt electrolytes (12.1 mS cm^{-1} for 21m LiTFSI, 3.0 mS cm^{-1} for 27.8m LiTFSI/BETI[2], 14.8 mS cm^{-1} for 35m NaFSI), making it a suitable candidate for battery applications. Considering also that this mixture shows the weakest tendency to crystallize below its liquidus temperature, we employ this electrolyte for the remainder of this study while drawing comparisons to the 35m NaFSI electrolyte.

Table 6-1 Physicochemical properties of 35m NaFSI and mixed electrolytes: All data was collected at 30 °C.

Sample acronym	Molality NaFSI ($mol \cdot kg^{-1}$)	Molality NaFTFSI ($mol \cdot kg^{-1}$)	Density ($g \cdot cm^{-3}$)	Viscosity ($mPa \cdot s$)	Conductivity ($mS\ cm^{-1}$)
35	35	0	1.923	75.8	14.8
30+5	30	5	1.919	82.9	13.0
25+10	25	10	1.914	94.2	11.8

As indicated by linear sweep voltammetry, partial substitution of FSI by FTFSI anions does not significantly alter the electrochemical stability of the electrolyte (see **Figure 6-8a**). Similarly, the Raman spectrum in the wavenumber region corresponding to the OH stretching modes of water is not altered noticeably (see **Figure 6-8b**). For a more detailed discussion, refer to the supporting information.

To capitalize on the robustness against crystallization over a wide temperature range, high conductivity, and wide electrochemical stability window, we implemented the 25m NaFSI + 10m NaFTFSI electrolyte in a 2 V class sodium-ion battery based on a $NaTi_2(PO_4)_3$ (NTP) anode and a $Na_3(VOPO_4)_2F$ (NVPOF) cathode. NTP has emerged as one of the most promising anode materials for aqueous sodium-ion batteries due to its relatively high theoretical capacity of 133 mAh g^{-1} and its flat redox potential of -0.6 V vs. SHE (2.1 V vs. Na/Na^+).[26, 27] The NVPOF cathode combines a theoretical capacity of 130 mAh g^{-1} with a high average discharge potential of 1.1 V vs. SHE (3.8 V vs. Na/Na^+).[28, 29] We synthesized NTP and NVPOF through solid-state routes as detailed in the methods section. The X-ray diffractograms of the two materials synthesized by us match the ones reported in literature (see **Figure 6-9**).

Figure 6-4 shows the cycling performance of our NTP/NVPOF full cell employing the mixed 25m NaFSI + 10m NaTFSI electrolyte at 30 °C at a rate of 1C. All cells were cycled between 0.3 and 2.2 V. We report specific capacities with respect to the active mass of the cathode as our cells are cathode limited. The cell displays an initial charge capacity of 110 mAh g^{-1}, which is relatively close to the theoretical capacity. The discharge capacity of the first cycle approaches 80 mAh g^{-1}, corresponding to 1.23 extracted sodium ions per formula unit of NVPOF. Hence, the Coulombic efficiency of the first cycle is 73%. The irreversible capacity may be related to the formation of a solid-electrolyte interphase on the NTP anode as reported for a sodium triflate-based electrolyte.[30] During subsequent cycling, the Coulombic efficiency rapidly reaches 99.7%, confirming the excellent electrochemical stability of the electrolyte. Consequently, a remarkable capacity retention of 77% is achieved after 500 full charge/discharge cycles with respect to the discharge capacity of the first cycle.

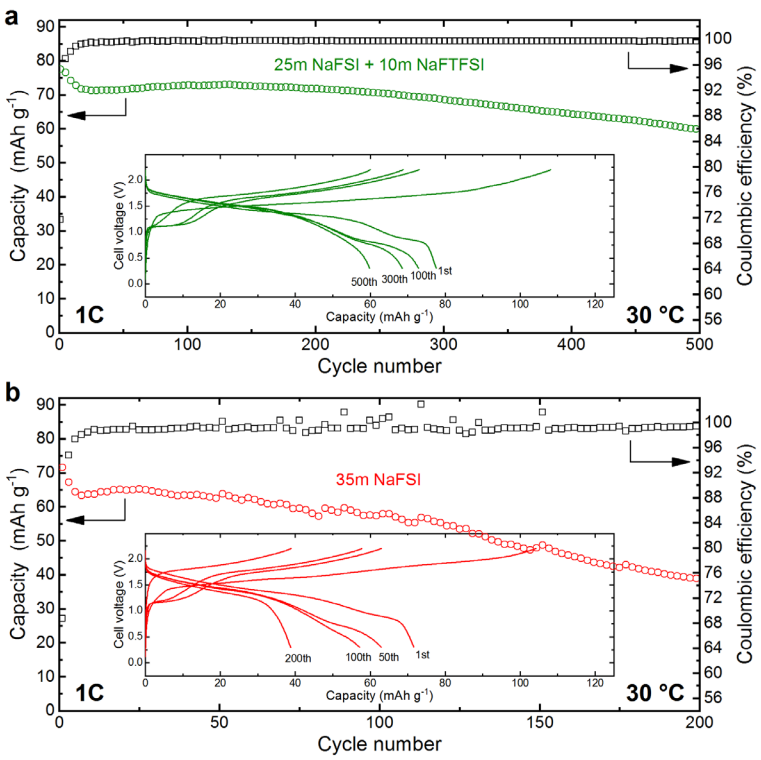

Figure 6-4 Electrochemical characterization of $NaTi_2(PO_4)_3$ | $Na_3(VOPO_4)_2F$ full cells at 1C. a,b, Discharge capacity (based on the active material weight of the cathode) and Coulombic efficiency of cells containing (a) 25m NaFSI + 10m NaFTFSI and (b) 35m NaFSI. The cells were cycled at 30 °C between 0.3 and 2.2 V. The insets show voltage profiles for selected cycles.

Figure 6-4b shows the capacity, Coulombic efficiency, and voltage profile evolution of a 35m NaFSI cell during identical long-term cycling at 1C. During the first few cycles, the performance of the cell resembles that of the mixed-anion electrolyte cell (compare to **Figure 6-4a**). But subsequently, the capacity of the 35m NaFSI cell deteriorates more rapidly. We assign the difference in cycling stability to crystallization of the 35m NaFSI electrolyte during operation of the cell. This crystallization manifests itself also in pronounced fluctuations in the Coulombic efficiency and in the increasing polarization visible in the voltage profiles (see inset of **Figure 6-4b**). Furthermore, we noticed that the exact cycling behavior of cells containing electrolytes with a tendency to crystallize at 30 °C like 35m NaFSI is not very reproducible. **Figure 6-10** shows the cycling results for a second, identical cell. This cell delivers a lower capacity than the cell in **Figure 6-4b** already during the first cycle, presumably due to electrolyte crystallization shortly after cell assembly. This cell also shows larger swings in Coulombic efficiency and more pronounced capacity fading during the 200 cycles of the experiment.

When we disassemble the cells after the long-term cycling experiment, we observe a clear difference between the two cells. **Figure 6-11** shows typical photographs of separators extracted from cycled cells containing mixed NaFSI/NaFTFSI or pure NaFSI electrolyte. The glass fibers soaked with the still liquid mixed-anion electrolyte can be clearly distinguished from the separator with solidified electrolyte recovered from the 35m NaFSI cell, on which distinct solid

domains can be observed under an optical microscope. Hence, electrolyte crystallization is indeed the cause for the lower stability of the 35m NaFSI cell relative to the cell containing the NaFSI/NaFTFSI electrolyte. We note that the introduction of FTFSI anions might also have an influence on the cycling stability of the cells by altering the structure of the SEI potentially forming on the NTP anode. However, a detailed investigation of the SEI is out of the scope of this work.

Compared to the 35m NaFSI cell, we observe even lower cycling stability when we test identical NTP/NVPOF full cells containing recently proposed water-in-salt electrolytes 8m NaTFSI or 9m sodium trifluoromethanesulfonate (NaOTf) (see. **Figure 6-12**).[24, 30] The electrochemical stability of these electrolytes is apparently insufficient to allow stable cycling of this 2 V class electrode couple.

In **Figure 6-5a**, we report cycling data for the cell containing the mixed-anion electrolyte at a lower rate of C/5 for different temperatures. This cycling protocol is more demanding due to the relatively longer time spent at high cell voltages. At 30 °C, the initial capacity is slightly higher than at 1C due to lower rate. Although notably lower than at 1C, the Coulombic efficiency still reaches a rather high value for a 2 V class aqueous battery of ~98% after 20 cycles. Correspondingly, the cell still delivers more than 85% of the initial capacity after 100 cycles at C/5. Combined with the average discharge voltage of 1.44 V, the initial energy density at C/5 is 64 Wh kg^{-1} based on the active masses of both anode and cathode. To the best of our knowledge, this is the highest value reported so far for an aqueous sodium-ion battery. The energy density of our cell is approximately twice as high as previously reported for the NTP/NVPOF electrode couple using less concentrated electrolytes.[31, 32]

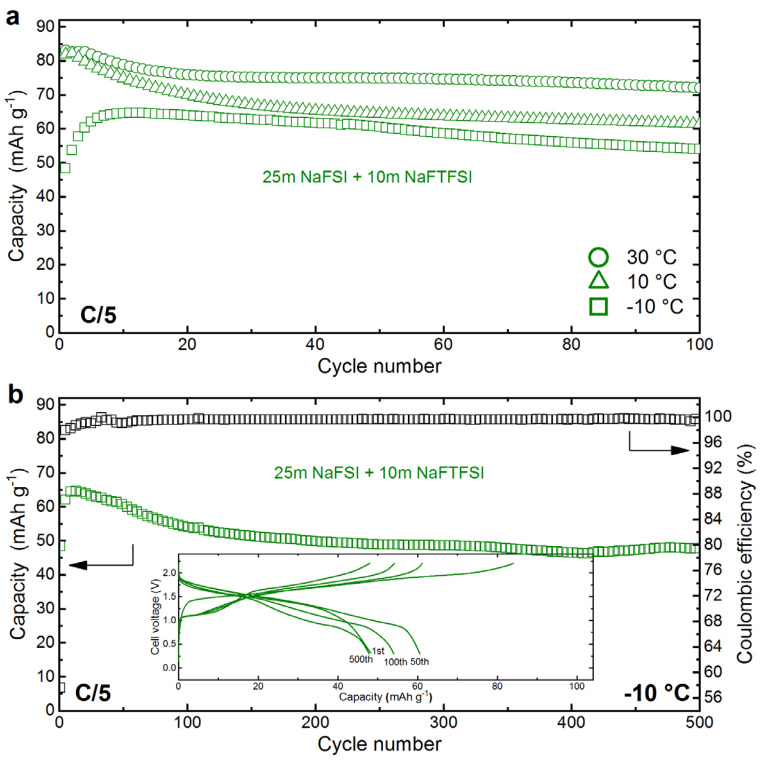

Figure 6-5 $NaTi_2(PO_4)_3$ | $Na_3(VOPO_4)_2F$ full cells cycled at C/5 at different temperatures. ***a****, Discharge capacity (based on the active material weight of the cathode) and Coulombic efficiency of cells containing 25m NaFSI + 10m NaFTFSI operated at 30 °C, 10 °C, and -10 °C. The cells were cycled between 0.3 and 2.2 V.* ***b****, Cycling data of the -10 °C cell shown in (a) for the total of 500 cycles. The inset shows voltage profiles for selected cycles.*

We also tested the low temperature cyclability of the NTP/NVPOF full cell at 10 and -10 °C (also shown in **Figure 6-5a**). The latter temperature is the typical lower temperature limit for the charging process of organic electrolyte-based lithium-ion batteries.[33, 34] As shown in the figure, the cells can indeed be cycled at 10 and -10 °C, confirming the DSC results and our visual observations. Due to slower kinetics at lower temperatures, the cells deliver a lower capacity compared to 30 °C: At 10 and -10 °C, the discharge capacities of the first cycles are 81 mAh g^{-1} and 48 mAh g^{-1}, respectively, compared to 83 mAh g^{-1} at 30 °C. Subsequently, the -10 °C cell goes through an activation phase that we assign to electrode wetting. This process increases the capacity to a value of 65 mAh g^{-1} after 12 cycles. During subsequent cycling, the cells show good cycling stability with capacity retentions after 100 cycles of 87% at 30 °C and 75% at 10 °C. At -10 °C capacity retention is 111% relative to the first cycle and 83% relative to the maximum in capacity occurring at cycle number 12.

We continued to cycle the -10 °C cell to reach a total number of 500 cycles (see **Figure 6-5b)**. The cell maintained high cycling stability, and we observed no signs of crystallization during the three months of operation. After 500 cycles, the capacity retention of the cell was 99%, 74%, and 89% relative to the 1st, 12th, and 100th cycle, respectively. This result highlights the effectiveness of the suppression of electrolyte crystallization by the presence of asymmetric FTFSI anions.

6.3 Conclusion

In conclusion, our study revealed that common water-in-salt electrolytes suffer from crystallization at room temperature leading to cell failure. To remedy this limitation, we demonstrated that the presence of anions with an asymmetric structure suppresses crystallization of water-in-salt electrolytes effectively. We developed a 2 V class sodium-ion battery based on a $NaTi_2(PO_4)_3$ anode and a $Na_3(VOPO_4)_2F$ cathode and demonstrated stable cycling at temperatures as low as -10 °C. Our results pave the way towards the development of high-voltage aqueous batteries that can be operated well below 25 °C as is required for many applications. A more detailed understanding of the influence of asymmetry on solution structure and long range ordering in water-in-salt electrolytes should enable further exploitation of this concept, leading to water-in-salt electrolytes with even wider liquid-state temperature windows.

6.4 Methods

LiFSI (battery grade, Fluorochem), LiTFSI (99.9%, Solvionic), LiBETI (>99%, Iolitec), NaFSI (99.7%, Solvionic), NaFTFSI (≥98%, Provisco), NaOTf (98%, Thermo Fischer), and NaTFSI (99.5%, Solvionic) were used as received. The electrolytes were prepared by dissolving one or two salts in high-purity water (prepared with a Millipore Milli-Q water purification system). The pH values of the electrolytes were adjusted to 5-6 using hydroxide solutions, and the electrolytes were degassed with argon.

Differential scanning calorimetry was carried out with a Netzsch STA 449 F3 simultaneous thermal analyzer. Ca. 30 mg of electrolyte sample were mixed with 1-2 mg of meso-carbon microbeads acting as crystallization agent and hermetically sealed in Al pans. All measurements were carried out at a scan rate of 1 °C·min^{-1}. The samples were equilibrated at 60 °C for 30 min prior to the start of the measurement. The eutectic melting points were defined by their onset temperature, whereas for the liquidus transitions the peak maxima were considered.[35]

Ionic conductivity was determined at 30 °C by impedance spectroscopy in sealed 2-electrode cells equipped with Pt electrodes (Materials Mates HTCC) using a Bio-Logic VMP3 electrochemical workstation. The frequency was scanned from 200 kHz to 1 Hz, the amplitude was set to 10 mV, and the temperature was controlled with a climatic chamber (Binder MK53). The electrolyte resistance was extracted from the intersection of the complex impedance curve with the horizontal axis of the Nyquist plot. Viscosity at 30 °C was determined with a Kyoto Electronics Manufacturing EMS-1000 electromagnetically spinning viscometer. Density at 30 °C was measured with an Anton Paar DMA 4100 M density meter.

Electrochemical stability windows at 30 °C were determined via linear sweep voltammetry in 3-electrode Swagelok cells with a Bio-Logic VMP3 electrochemical workstation. Stainless steel and titanium working electrodes were used for the cathodic and anodic scans, respectively. Activated carbon-based pellets were used as counter electrodes, and a miniature Ag/AgCl electrode (eDAQ) was used as reference electrode. The scan rate was set to 0.1 mV s^{-1}.

Raman spectra of selected electrolytes sealed in NMR tubes were collected at room temperature on a Renishaw Ramascope using a laser with a wavelength of 633 nm.

$NaTi_2(PO_4)_3$ and $Na_3(VOPO_4)_2F$ were synthesized via solid-state routes similar to the ones reported in literature:[28, 36]

For the synthesis of $NaTi_2(PO_4)_3$, the precursors Na_2CO_3 (>99.8%, VWR), TiO_2 (>99.5%, Sigma-Aldrich), and $(NH_4)_2HPO_4$ (>98.5% Sigma-Aldrich) were ball-milled, calcined at 500 °C for 5 h in air, ground, and then annealed at 900 °C for 24 h in air. For the carbon-coating, the as prepared $NaTi_2(PO_4)_3$ was ball-milled with glucose (10% solution in water), dried under stirring, and finally reacted at 550 °C under argon for 1.5 h.

For the synthesis of $Na_3(VOPO_4)_2F$, a $VOPO_4{\cdot}2H_2O$ precursor was synthesized from V_2O_5 (>99%, Sigma-Aldrich) und H_3PO_4 (85%, Sigma-Aldrich) following a wet-chemical route:[37] Stoichiometric amounts of V_2O_5 and phosphoric acid were mixed with water (twice the volume of phosphoric acid), and heated to reflux overnight. The bright yellow product was washed with water and acetone and dried at 120 °C. Next, $VOPO_4{\cdot}2H_2O$ was ball-milled in acetone together with NaF (>99%, Sigma-Aldrich) and Na_2CO_3. The obtained powder mixture was pelletized and annealed at 700 °C for 1.5 h. The carbon-coating was obtained following the same procedure as for $NaTi_2(PO_4)_3$. Powder X-ray diffractograms of the two active materials were recorded with a Panalytical X- X'pert PRO MRD using Cu-Kα1 radiation.

$NaTi_2(PO_4)_3$ and $Na_3(VOPO_4)_2F$ electrodes with a diameter of 12 mm and a mass loading of 4 to 6 mg cm^{-2} were prepared from *N*-methyl-2-pyrrolidone (NMP)-based slurries on stainless steel and titanium current collectors, respectively. The composition of the electrodes was 80% active material, 10% polyvinylidene difluoride (PVdF) binder (Arkema Kynar HSV900), and 10% carbon black (IMERYS Graphite & Carbon C-NERGY SUPER C65). The electrodes were pressed at 5 t for 30 s.

2-electrode full cells were assembled using Swagelok stainless steel T-cells. The mass loading of the cathode exceeded that of the anode by 10-20%. Whatman GF/D glass microfiber filters with a diameter of 13 mm were used as separator. The cells were filled with ca. 200 µl of electrolyte. The full cells were electrochemically characterized at -10, 10, or 30 °C using a Bio-Logic VMP3 electrochemical workstation.

6.5 Supplementary Information

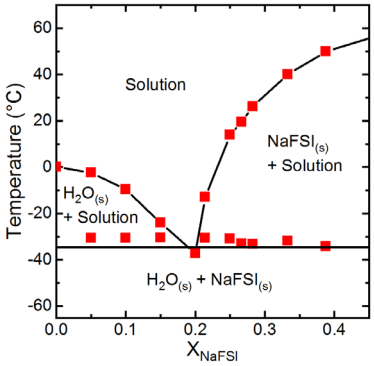

Figure 6-6 Liquid-solid phase diagram for the NaFSI-H_2O binary system. The melting points of pure water and NaFSI were used as end members of the composition range.

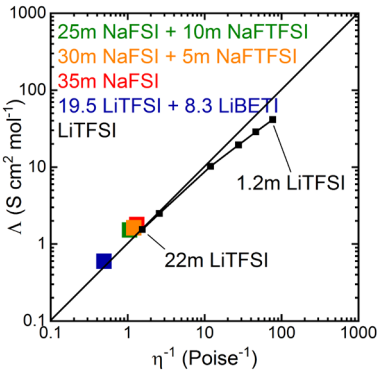

Figure 6-7 Walden plot for 35m NaFSI and mixed electrolytes with asymmetric anions at 30 °C. Data for the hydrate-melt electrolyte and aqueous LiTFSI solutions of various concentrations (taken from ref. [1]) are shown for comparison.

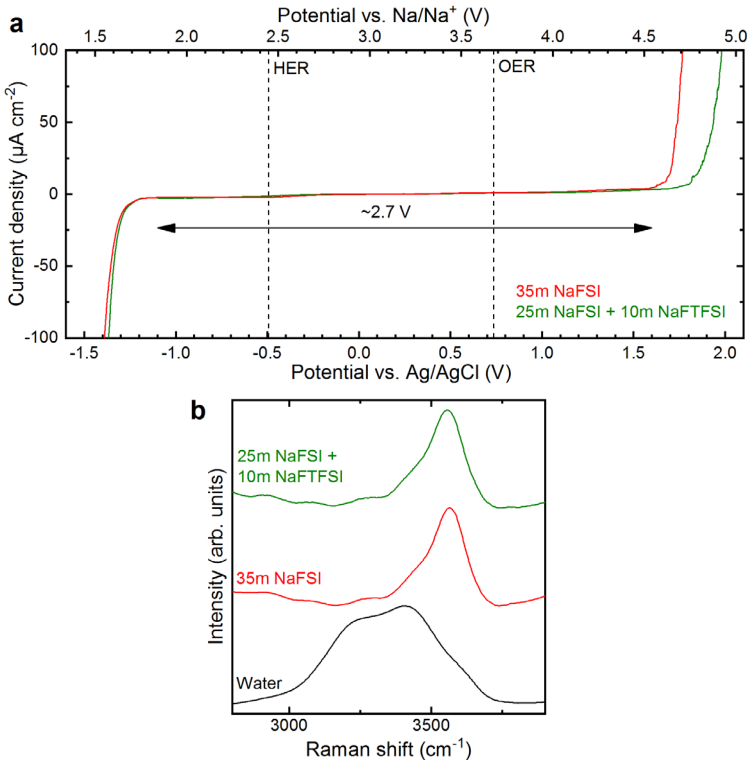

Figure 6-8 a, Linear sweep voltammograms of 25m NaFSI + 10m NaFTFSI and of 35m NaFSI at 30 °C. The scan rate was set to 0.1 mV·s^{-1}. The thermodynamic potentials for the hydrogen and oxygen evolution reactions (HER and OER, respectively) at pH 5 are indicated by dashed vertical lines. b, Raman spectra of water, 25m NaFSI + 10m NaFTFSI, and 35m NaFSI in the wavenumber region corresponding to the OH stretching modes of water.

We determined the electrochemical stability of the mixed-anion electrolyte via separate linear voltammetry sweeps to determine the cathodic and anodic stability, respectively. We applied a threshold current-density of ±3 µA cm^{-2} to determine the stability limits. For the 35m NaFSI electrolyte, we previously reported an electrochemical stability window of 2.6 V. We observe unchanged reductive stability and even slightly improved oxidative stability resulting in an electrochemical stability window of 2.7 V.

Raman spectroscopy in the wavenumber region corresponding to the OH stretching modes of water was used to probe the water environment of the electrolytes (see **Figure 6-8b**). Pure water shows a broad signal between 2900 and 3700 cm^{-1} corresponding to a wide dispersion of the OH bond strengths due to the formation of various clusters.[38] Consistent with the small difference in electrochemical stability, the spectra for the mixed-anion electrolyte and for 35m NaFSI are very similar in this wave number region. The emergence of the sharp peak at ~3500 cm^{-1} and the vanishing of the broad signal of water for both electrolytes indicates strong interaction of water with the dissolved cations and therefore a low level of free water molecules as previously suggested.[1, 2]

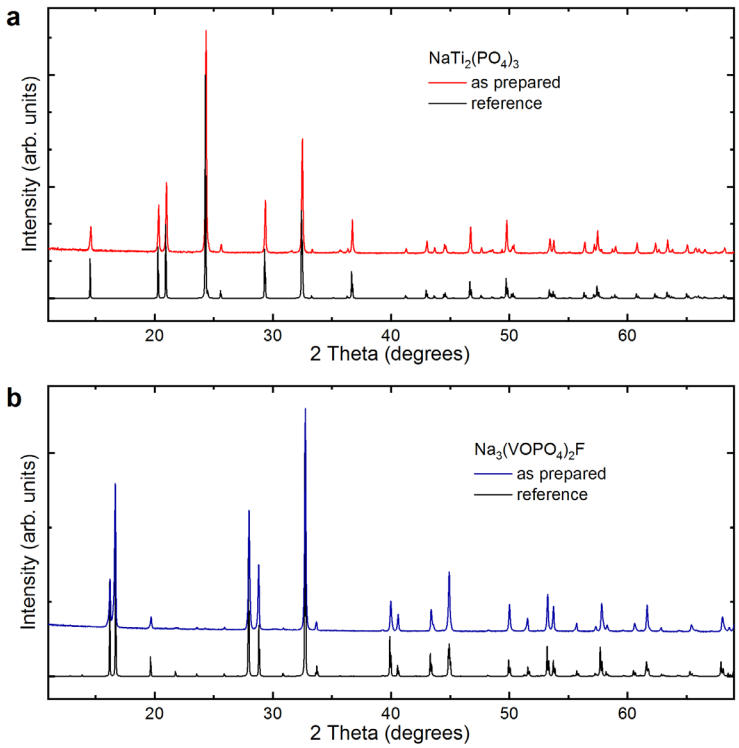

Figure 6-9 a,b, X-ray diffractograms of (a) $NaTi_2(PO_4)_3$ and (b) $Na_3(VOPO_4)_2F$ prepared by us. For comparison, reference diffractograms are also shown.[39, 40]

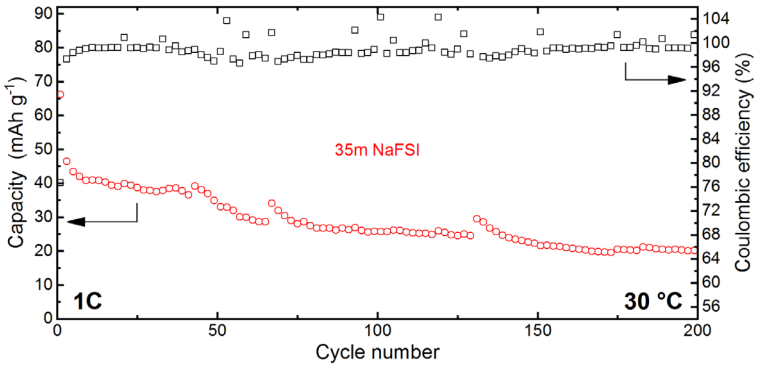

Figure 6-10 Performance of a second of $NaTi_2(PO_4)_3$ | $Na_3(VOPO_4)_2F$ full cell containing 35m NaFSI as the electrolyte. Discharge capacity (based on the active material weight of the cathode) and Coulombic efficiency of a $NaTi_2(PO_4)_3$| $Na_3(VOPO_4)_2F$ full cell identical to the one shown in Fig. 3b. The current rate was set to 1C and the cell was cycled between 0.3 and 2.2 V at 30 °C.

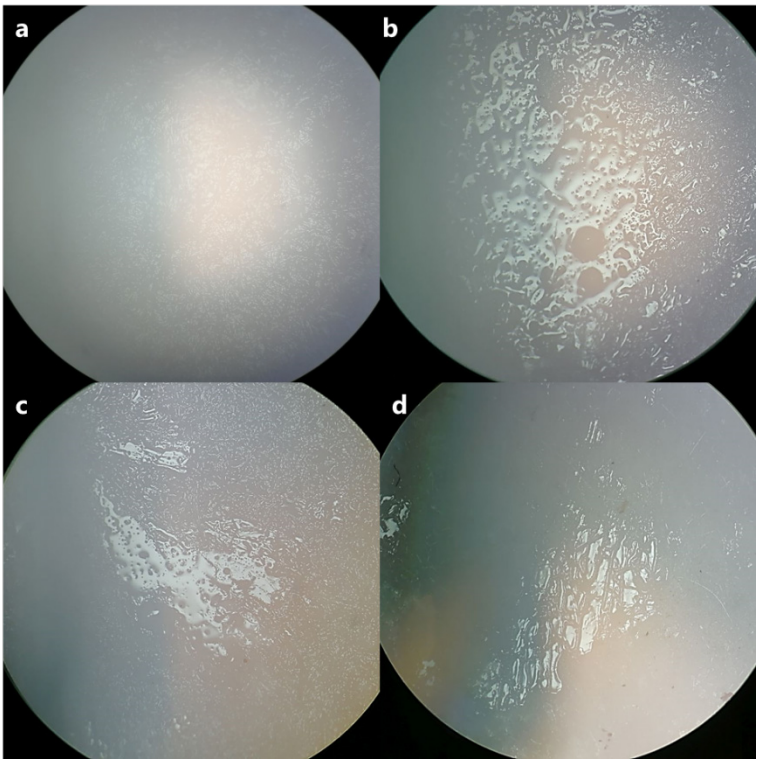

Figure 6-11 Micrographs of glass fiber separators extracted from cycled cells shown in Fig. 4, containing (a) 25m NaFSI + 10m NaFTFSI or (b-d) 35m NaFSI.

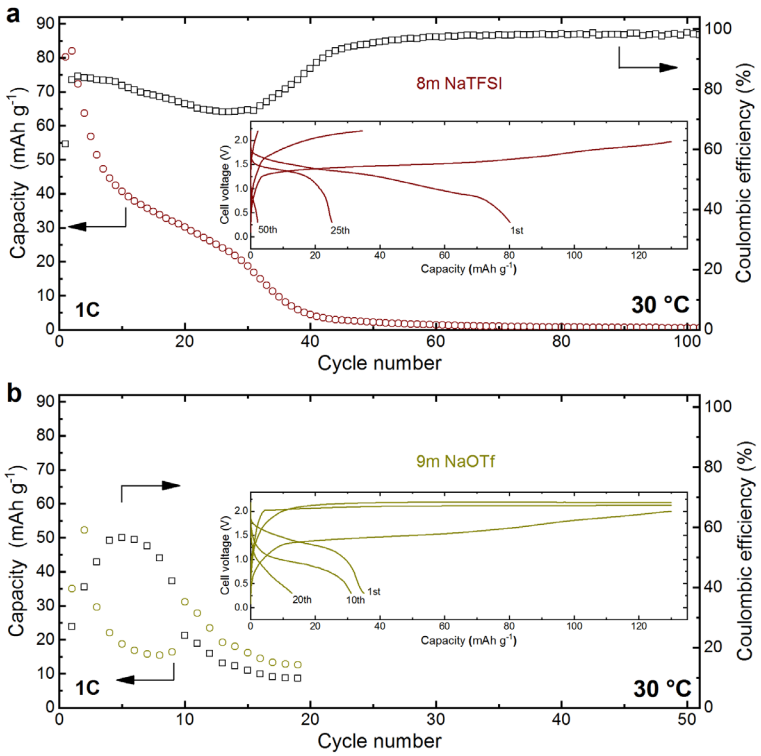

Figure 6-12 Cycling performance of sodium-ion full cells employing reference electrolytes. a,b, Discharge capacity (based on the active material weight of the cathode) and Coulombic efficiency of $NaTi_2(PO_4)_3$| $Na_3(VOPO_4)_2F$ full cells containing (a) 8m NaTFSI and (b) 9m NaOTf as the electrolyte. The cells were cycled at 30 °C between 0.3 and 2.2 V. The insets show voltage profiles for selected cycles.

References

1. Suo, L., et al., *"Water-in-salt" electrolyte enables high-voltage aqueous lithium-ion chemistries.* Science, 2015. **350**(6263): p. 938-43.
2. Yamada, Y., et al., *Hydrate-melt electrolytes for high-energy-density aqueous batteries.* Nat. Energy, 2016. **1**: p. 16129.
3. Kühnel, R.-S., D. Reber, and C. Battaglia, *A High-Voltage Aqueous Electrolyte for Sodium-Ion Batteries.* ACS Energy Lett., 2017. **2**(9): p. 2005-2006.
4. Suo, L., et al., *Advanced High-Voltage Aqueous Lithium-Ion Battery Enabled by "Water-in-Bisalt" Electrolyte.* Angew. Chem., 2016. **55**(25): p. 7136-41.
5. Suo, L., et al., *"Water-in-Salt" electrolytes enable green and safe Li-ion batteries for large scale electric energy storage applications.* J. Mater. Chem. A., 2016. **4**(17): p. 6639-6644.
6. Yang, C., et al., *4.0 V Aqueous Li-Ion Batteries.* Joule, 2017. **1**(1): p. 122-132.
7. Wang, F., et al., *Stabilizing high voltage $LiCoO_2$ cathode in aqueous electrolyte with interphase-forming additive.* Energy Environ. Sci., 2016. **9**(12): p. 3666-3673.
8. Leonard, D.P., et al., *Water-in-Salt Electrolyte for Potassium-Ion Batteries.* ACS Energy Lett., 2018. **3**(2): p. 373-374.
9. Lukatskaya, M.R., et al., *Concentrated Mixed Cation Acetate "Water-in-Salt" Solutions as Green and Low Cost High Voltage Electrolytes for Aqueous Batteries.* Energy Environ. Sci., 2018. **3**(3): p. 373-374.
10. Wang, F., et al., *Highly reversible zinc metal anode for aqueous batteries.* Nat. Mater., 2018. **17**(6): p. 543.
11. Zhang, N., et al., *Rechargeable aqueous zinc-manganese dioxide batteries with high energy and power densities.* Nat. Commun., 2017. **8**(1): p. 405.
12. Ding, S., et al., *Diminution of Supercooling of Electrolytes by Carbon Particles.* J. Electrochem. Soc., 1999. **146**(11): p. 3974-3980.
13. Ding, M.S. and K. Xu, *Phase Diagram, Conductivity, and Glass Transition of LiTFSI–H_2O Binary Electrolytes.* J. Phys. Chem. C, 2018. **122**(29): p. 16624-16629.
14. Mohamed, A.I. and J. Whitacre, *Capacity Fade of $NaTi_2(PO_4)_3$ in Aqueous Electrolyte Solutions: Relating pH Increases to Long Term Stability.* Electrochim. Acta, 2017. **235**: p. 730-739.
15. Zhang, M. and J. Dahn, *Electrochemical Lithium Intercalation in VO_2(B) in Aqueous Electrolytes.* J. Electrochem. Soc., 1996. **143**(9): p. 2730-2735.
16. Gutzow, I. and J. Schmelzer, *The vitreous state*. 1995: Springer.
17. Wunderlich, B., *Theory of cold crystallization of high polymers.* The Journal of Chemical Physics, 1958. **29**(6): p. 1395-1404.
18. Fredlake, C.P., et al., *Thermophysical properties of imidazolium-based ionic liquids.* J. Chem. Eng. Data, 2004. **49**(4): p. 954-964.
19. Mullin, J.W., *Crystallization*. 2001: Elsevier.
20. Uthaipan, N., et al., *Effects of cooling rates on crystallization behavior and melting characteristics of isotactic polypropylene as neat and in the TPVs EPDM/PP and EOC/PP.* Polym. Testing, 2015. **44**: p. 101-111.

21. Lee, S., et al., *Multiple pathways of crystal nucleation in an extremely supersaturated aqueous potassium dihydrogen phosphate (KDP) solution droplet.* Proc. Natl. Acad. Sci. U.S.A., 2016. **113**(48): p. 13618-13623.

22. Holbrey, J.D. and K.R. Seddon, *The phase behaviour of 1-alkyl-3-methylimidazolium tetrafluoroborates; ionic liquids and ionic liquid crystals.* Dalton Trans., 1999. **13**(13): p. 2133-2140.

23. Wilkes, J.S., *Properties of ionic liquid solvents for catalysis.* J. Mol. Catal. Chem. , 2004. **214**(1): p. 11-17.

24. Reber, D., R.-S. Kühnel, and C. Battaglia, *High-voltage aqueous supercapacitors based on NaTFSI.* Sustainable Energy Fuels, 2017. **1**(10): p. 2155-2161.

25. Borodin, O., et al., *Liquid structure with nano-heterogeneity promotes cationic transport in concentrated electrolytes.* ACS nano, 2017. **11**(10): p. 10462-10471.

26. Park, S.I., et al., *Electrochemical Properties of $NaTi_2(PO_4)_3$ Anode for Rechargeable Aqueous Sodium-Ion Batteries.* J. Electrochem. Soc., 2011. **158**(10): p. A1067-A1070.

27. Delmas, C., A. Nadiri, and J. Soubeyroux, *The nasicon-type titanium phosphates $ATi_2(PO_4)_3$ (A= Li, Na) as electrode materials.* Solid State Ion., 1988. **28**: p. 419-423.

28. Park, Y.U., et al., *A New High-Energy Cathode for a Na-Ion Battery with Ultrahigh Stability.* J. Am. Chem. Soc., 2013. **135**(37): p. 13870-8.

29. Park, Y.-U., et al., *A Family of High-Performance Cathode Materials for Na-ion Batteries, $Na_3(VO_{1-x}PO_4)_2F_{1+2x}(0 \leq x \leq 1)$: Combined First-Principles and Experimental Study.* Adv. Funct. Mater., 2014. **24**(29): p. 4603-4614.

30. Suo, L., et al., *"Water-in-Salt" Electrolyte Makes Aqueous Sodium-Ion Battery Safe, Green, and Long-Lasting.* Adv. Energy Mater., 2017. **7**(21): p. 1701189.

31. Kumar, P.R., et al., *$Na_3V_2O_{2x}(PO_4)_2F_{3-2x}$: A stable and high-voltage cathode material for aqueous sodium-ion batteries with high energy density.* J. Mater. Chem. A, 2015. **3**(12): p. 6271-6275.

32. Kumar, P.R., et al., *$Na_3V_2O_2(PO_4)_2F$-MWCNT nanocomposites as a stable and high rate cathode for aqueous and non-aqueous sodium-ion batteries.* J. Power Sources, 2016. **324**: p. 421-427.

33. Zhang, S., K. Xu, and T. Jow, *Low temperature performance of graphite electrode in Li-ion cells.* Electrochim. Acta, 2002. **48**(3): p. 241-246.

34. Zhang, S., K. Xu, and T. Jow, *The low temperature performance of Li-ion batteries.* J. Power Sources, 2003. **115**(1): p. 137-140.

35. Ding, M.S., K. Xu, and T.R. Jow, *Liquid-Solid Phase Diagrams of Binary Carbonates for Lithium Batteries.* J. Electrochim. Soc., 2000. **147**(5): p. 1688-1694.

36. Li, Z., et al., *Towards High Power High Energy Aqueous Sodium-Ion Batteries: The $NaTi_2(PO_4)_3/Na_{0.44}MnO_2$ System.* Adv. Energy Mater., 2013. **3**(3): p. 290-294.

37. Brody, J.F., J.W. Johnson, and J. Vaughey, *Vanadyl Phosphates and Organylphosphonates.* Inorganic Syntheses: Nonmolecular Solids, Volume 30, 1995: p. 241-248.

38. Smith, J.D., et al., *Unified description of temperature-dependent hydrogen-bond rearrangements in liquid water.* Proc. Natl. Acad. Sci. U.S.A., 2005. **102**(40): p. 14171-14174.

39. Rodrigo, J., P. Carrasco, and J. Alamo, *Thermal expansion of NaTi2 (PO4) 3 studied by rietveld method from X-ray diffraction data.* Materials Research Bulletin, 1989. **24**(5): p. 611-618.

40. Sharma, N., et al., *Sodium distribution and reaction mechanisms of a Na3V2O2 (PO4) 2F electrode during use in a sodium-ion battery.* Chemistry of Materials, 2014. **26**(11): p. 3391-3402.

7 Impact of Anion Asymmetry on Local Structure and Supercooling Behavior of Water-in-Salt Electrolytes

David Reber,[1,2] Norio Takenaka,[3,4] Ruben-Simon-Kühnel,[1] Atsuo Yamada,[3,4] and Corsin Battaglia[1]

[1]Laboratory Materials for Energy Conversion, Swiss Federal Laboratories for Materials Science and Technology, Empa, Überlandstrasse 129, 8600 Dübendorf, Switzerland

[2]Institut des Matériaux, École Polytechnique Fédérale de Lausanne, EPFL, Station 12, 1015 Lausanne, Switzerland

[3]Department of Chemical System Engineering, The University of Tokyo, 7-3-1, Hongo, Bunkyo-ku, Tokyo 113-8656, Japan

[4]Elements Strategy Initiative for Catalysts & Batteries (ESICB), Kyoto University, 1-30, Goryo-Ohara, Nishikyo-ku, Kyoto 615-8245, Japan

Journal of Physical Chemistry Letters 2020, 11, 4720-4725

DOI: 10.1021/acs.jpclett.0c00806

https://doi.org/10.1021/acs.jpclett.0c00806

Suppressed crystallization due to anion-asymmetry enabled the development of a highly stable 2 V class aqueous sodium-ion battery operating in a wide temperature range. Based on classical molecular dynamics simulations and Raman spectroscopy, we hypothesize that different anion-cation coordination geometries and subsequent intramolecular bond rotations lie at the heart of the phenomenon. **Author contributions:** D.R., C.B. conceived the idea for this study. D.R. and N.T. designed most experiments. D.R. carried out the experiments and simulations. N.T. supervised the simulations. D.R., N.T., R.-S.K., C.B. analyzed the data. D.R. prepared the figures and wrote the original draft of the manuscript. N.T., R.-S.K., A.Y., C.B. critically reviewed and edited the manuscript. All coauthors read and approved the final manuscript.

Abstract

Salts with asymmetric (fluorosulfonyl)(trifluoromethanesulfonyl)imide (FTFSI) anions have recently shown to suppress crystallization of water-in-salt electrolytes, enabling low-temperature operation of high-voltage aqueous rechargeable batteries. To clarify the underlying mechanism for the kinetic suppression of crystallization, we investigate the local solution structures and dynamic behaviors of water-in-salt electrolytes based on the asymmetric FTFSI anion and its symmetric anion analogues by Raman spectroscopy and molecular dynamics simulations. We find that monodentate coordination of FTFSI to cations leads to high rotational mobility of the uncoordinated SO_2CF_3 group. We conclude that the peculiar, coordination dependent, local dynamics in the asymmetric FTFSI anion, manifested by enhanced intramolecular bond rotation, enables the strong supercooling behavior.

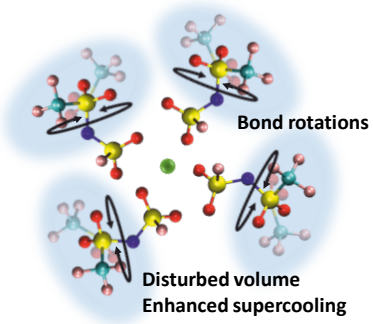

7.1 Introduction

Highly concentrated aqueous electrolytes, such as water-in-salt[1] or hydrate-melt[2] electrolytes, offer a wide electrochemical stability window of over 3 V, compared to approximately 1.5 V for dilute aqueous electrolytes, and have enabled high-voltage aqueous rechargeable batteries. Such approaches are narrowing the gap to state-of-the-art batteries that are based on flammable organic electrolytes. In particular, the oxidative stability of water-in-salt electrolytes is comparable to organic electrolytes, enabling high-voltage cathodes (e.g. $LiMn_2O_4$), while complementary approaches were developed to suppress hydrogen evolution on the anode.[1-11] Batteries with concentrated aqueous electrolytes promise increased safety due to their non-flammability and are potentially less expensive to manufacture as a dry atmosphere is not required during cell assembly, partially overcoming the higher electrolyte cost associated with the high salt concentration.[12]

Typically, at room temperature, these electrolytes are saturated or eutectic solutions of one or more salts with overall molalities above 20 moles of salt per kilogram of water (20 mol/kg, 20m). Prominent examples are the archetypical 21m lithium bis(trifluoromethanesulfonyl)imide (LiTFSI) water-in-salt[1], 28m hydrate-melt[2], and 28m water-in-bisalt[4] electrolytes. Operation below room temperature however results in partial crystallization and premature cell failure.[9] Our recent work has shown that in 35-molal bis(fluorosulfonyl)imide (FSI)-based electrolytes, partial substitution of symmetric FSI anions by asymmetric (fluorosulfonyl)(trifluoromethanesulfonyl)imide (FTFSI) anions kinetically suppresses crystallization, extending the liquid-state temperature range of the electrolyte to lower temperatures.[9] This finding enabled the development of a highly-stable 2 V class aqueous sodium-ion battery that can be operated in a wide temperature range.[9] In contrast, no significant change in supercooling behavior was observed when simply mixing symmetric FSI and TFSI salts.[9]

Here, we investigate the supercooling behaviors of water-in-salt electrolytes containing asymmetric FTFSI anions, or symmetric FSI or TFSI ones (**Figure 7-1a**). We compare the local solution structures and dynamic behaviors by means of Raman spectroscopy and molecular dynamics simulations, and discuss the key factors governing the observed differences in supercooling behavior. We note that the FSI and FTFSI anions are prone to hydrolysis due to the presence of two or one S–F bond(s), respectively.[13] However, the peculiar supercooling behavior merits investigation, as the results may be transferable to other electrolytes.

7.2 Results and Discussion

Figure 7-1b shows the liquidus temperatures of concentrated LiFSI, LiFTFSI and LiTFSI-based aqueous electrolytes determined by means of differential scanning calorimetry (DSC). The experimental details are described in the Supporting Information. The liquidus temperature describes the transition to a fully-liquid state and lies at 28 °C for 35m LiFSI, 18 °C for 35m LiFTFSI, and 47 °C for 35m LiTFSI. To investigate the supercooling behavior of these solutions, 35m LiFSI and 35m LiTFSI solutions were stored at ~25 °C below their respective liquidus temperatures (at 4 and 22 °C, respectively), and 35m LiFTFSI samples were stored at ~35 °C below their liquidus temperature (at –18 °C). As illustrated in **Figure 7-1c-e**, the LiFSI samples consistently crystallize after 2-3 days (fine precipitate) at 4 °C, while the LiTFSI samples crystallize within minutes after cooling below approximately 30 °C (rather large clear crystals). In contrast, supercooled LiFTFSI samples remain liquid after four weeks at −18 °C. These results clearly demonstrate the pronounced difference in supercooling behavior among the concentrated LiFSI, LiTFSI, and LiFTFSI solutions.

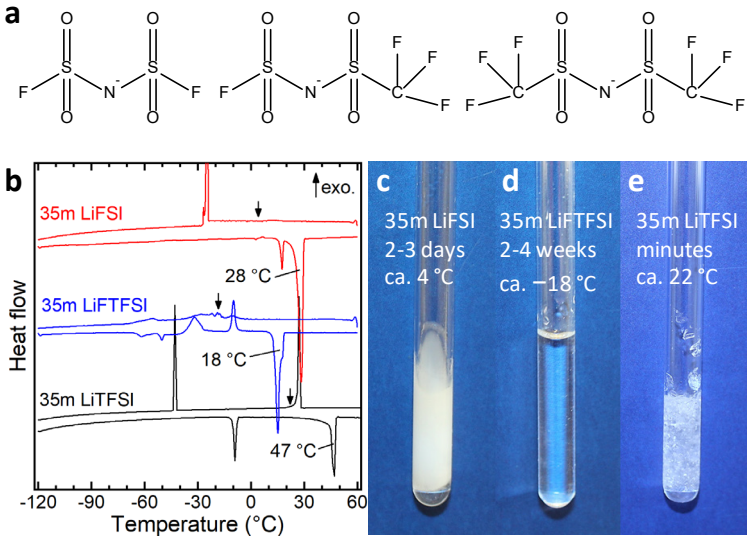

Figure 7-1 (a) Chemical structures of the FSI, FTFSI, and TFSI anions, (b) DSC cooling and heating curves with indicated liquidus temperatures for 35m LiFSI, LiFTFSI, and LiTFSI, respectively, and (c-e) photographs of these solutions after storage at (c) 4 °C, (d) −18 °C, and (e) 22 °C, respectively. These temperatures are indicated by arrows in (b).

To elucidate the origin for this difference in supercooling behavior, we investigated the local solution structures by means of Raman spectroscopy (samples heated to 60 °C and immediately measured at room temperature, see Supporting Information for experimental details). The Raman band at 730–760 cm^{-1}, corresponding to the expansion and contraction of the whole anion,[14-16] is observed at increasing wave numbers in the order of TFSI < FTFSI < FSI (**Figure 7-2a**). The increased peak broadening in the order of TFSI < FTFSI < FSI indicates an increase in the degree of structural disorder. This trend, as probed by the width of this Raman

band, however does not correlate with that in supercooling behavior: The less ordered LiFSI solution readily crystallizes below its liquidus temperature, whereas the more ordered LiFTFSI solution shows pronounced supercooling. Furthermore, there is no significant difference for the Raman band in the wavenumber region corresponding to the O-H vibrations of water[1-3] with a sharp peak at ~3550 cm^{-1} (**Figure 7-2b**), indicating that the cation-water binding is not responsible for the differences in crystallization kinetics.

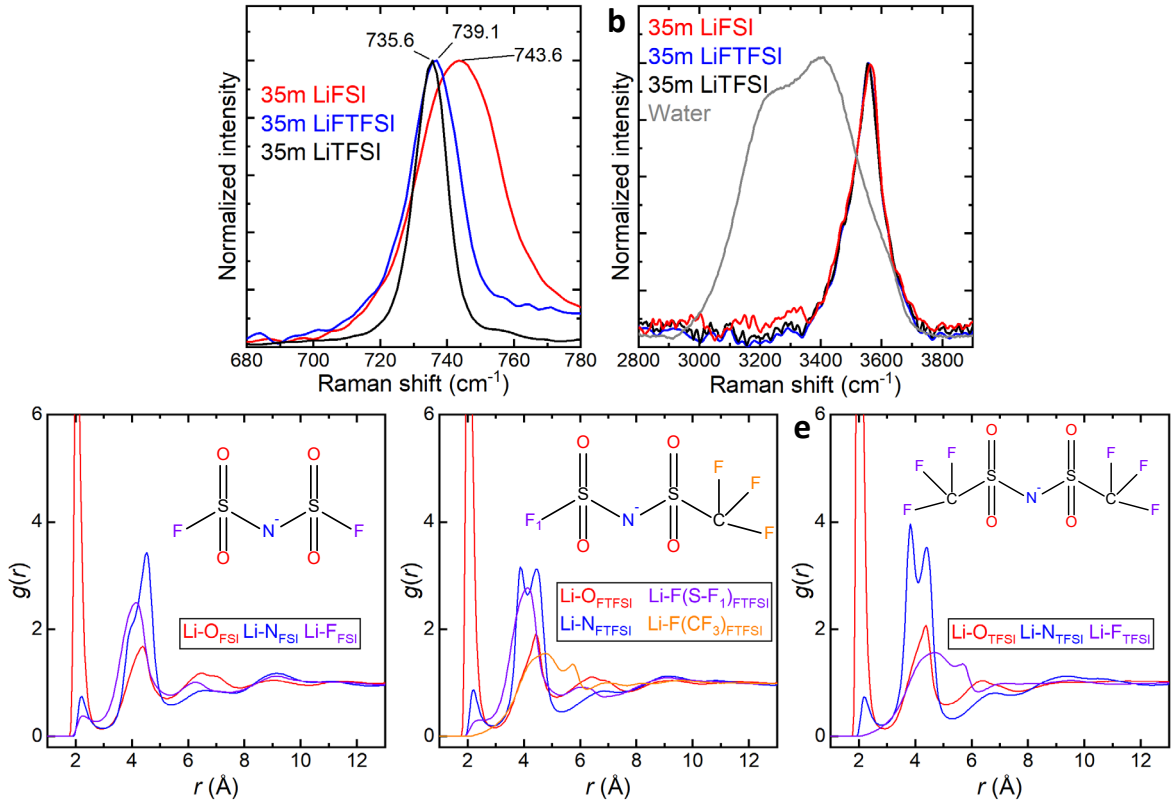

Figure 7-2 Raman spectra in the wavenumber region corresponding to the whole anion expansion and contraction modes of the anions in 35m LiFSI, LiFTFSI, and LiTFSI, respectively. (b) Raman spectra in the wavenumber region corresponding to O-H vibrations of water molecules of the same solutions and of pure water. (c-e) Radial distribution functions of lithium cations and oxygen, nitrogen, and fluorine atoms of the anions, respectively, for (c) 35m LiFSI, (d) 35m LiFTFSI, and (e) 35m LiTFSI. The molecular structures of the FSI, FTFSI, and TFSI anions are shown as color-coded insets in the respective subfigures.

For a better understanding of local solution structures, we conducted classical molecular dynamics (MD) simulations at 60 °C. At this temperature, all three investigated solutions are thermodynamically in the liquid state as can be seen from their liquidus temperatures that range from 18 to 47 °C (see again **Figure 7-1b**). The simulation details are described in the supporting information. We chose this temperature, as nucleation itself is a rare event typically occurring on a timescale much longer than what can be reached in a direct simulation.[17, 18] **Figure 7-2c-e** show radial distribution functions (RDFs) between the lithium cations and anions. The oxygen atoms of the anions are closest to the cations, which corresponds to coor-

dination mostly taking place through these atoms, as is common for the studied imide anions.[19-23] A small peak is observed in the lithium-fluorine RDF of 35m LiFSI and in the Li-F_1 RDF of 35m LiFTFSI at a similar distance of approximately 2 Å as the first peak in the lithium-oxygen RDF. In contrast, the Li-F_{CF3} RDF for the FTFSI solution clearly shows that the fluorine atoms of the CF_3 group are on average further away from the cation than the F_1 fluorine atom bound to sulfur. The CF_3 fluorine atoms in TFSI anion are also found to be pointing away from the cation. The cation-water, water-water, and cation-cation RDFs can be found together with brief discussions in the supporting information (**Figure 7-6** to **Figure 7-8**).

As shown in more detail in **Figure 7-3a**, the lithium-nitrogen RDFs show two distinct peaks at 3.9 Å (labeled B) and 4.5 Å (labeled M) corresponding to bidentate and monodentate coordination through oxygen atoms, respectively.[20, 23-25] **Figure 7-3b-d** show typical snapshots, highlighting the difference in the coordination structures around lithium cations between LiFSI, LiFTFSI and LiTFSI-based electrolytes. The labels M and B, respectively again indicate monodentate and bidentate coordination. For FSI, monodentate coordination is most prominent, whereas for FTFSI both monodentate and bidentate coordination are equally common. For TFSI, the bidentate geometry is dominating, causing both CF_3 groups to point away from the cation. This explains the absence of a Li-F peak around 2 Å in **Figure 7-2c**. We note that it would be interesting to study the influence of temperature on the relative occurrence of the anion conformers and mono- and bidentate Li^+ coordination in a follow-up study. Studies of ionic liquids have shown that the two minimum energy conformers with C_1 or C_2 symmetry are typically in equilibrium for both FSI and TFSI in the liquid state, and that specific interactions with the cation can influence the relative occurrence of the two conformers.[26, 27]

The first solvation shell of imide anions around a cation can be defined by using the minimum around 5.4 Å in the lithium-nitrogen RDFs.[20, 28] The radius of the first solvation shell slightly decreases with increasing anion size due to the decrease in the number of anions within the first solvation shell as extracted from the running integral of the RDF (**Figure 7-9**). The trend in size of the solvation shells (FSI > FTFSI > TFSI) anticorrelates with the trend in bidentate contribution (FSI < FTFSI < TFSI). Hence, the more bidendate coordination, the smaller the solvation shell. Furthermore, comparison with **Figure 7-2a** shows that the Raman peak width, indicating solution disorder, increases with decreasing bidentate coordination.

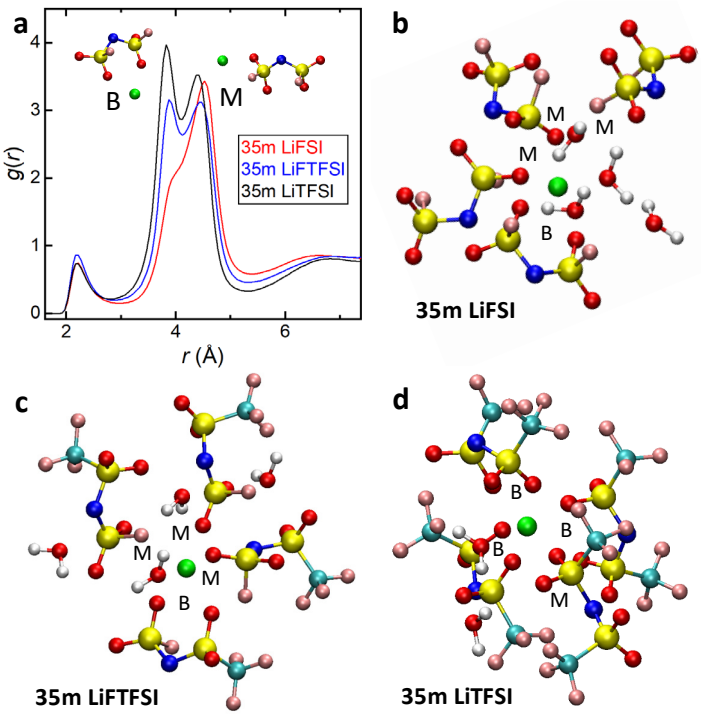

Figure 7-3 (a) Radial distribution functions between lithium cations and nitrogen atoms of anions and (b-d) MD simulation snapshots of solvation structures around a cation in 35m (b) LiFSI, (c) LiFTFSI, and (d) LiTFSI. The monodentate and bidentate coordination schemes are marked M and B, respectively. Hydrogen, carbon, nitrogen, oxygen, fluorine, and sulfur atoms are shown in white, cyan, blue, red, pink, and yellow, respectively. Lithium cations are shown in green. For visual simplification, other cations within the first solvation shell (~5.4 Å) have been omitted.

The analysis of the Raman spectra and RDFs clearly demonstrates significant differences in local solution structure among the FSI, FTFSI, and TFSI-based electrolytes. However, these variations are not enough to explain the differences in supercooling behavior. To investigate the effect of intramolecular bond rotations,[29] we compared the distributions of selected dihedral angles among these electrolytes (**Figure 7-4a-c**). In FSI and TFSI-based electrolytes (**Figure 7-4a** and **c**), the rotation around the sulfur-nitrogen bond is strongly confined to angles near 180°. In contrast, in the FTFSI-based electrolyte (**Figure 7-4b**), the rotation of the FSO_2 group is restricted near 90° due to the monodentate coordination of cations to the FSO_2 group. The SO_2CF_3 group however, can freely rotate without significant restriction as indicated by the homogeneous distribution of the dihedral angle. Furthermore, for FTFSI the rotation of the SO_2CF_3 group exhibits a relatively slow relaxation as indicated by prolonged oscillations of the dihedral angle autocorrelation function over the whole simulation time of 50 ns. In contrast, the autocorrelation for FSI and TFSI approaches zero after about half the simulation time (**Figure 7-10**). Combined with the results presented in **Figure 7-4**, these results suggest that the SO_2CF_3 group of FTFSI has higher rotational mobility than the corresponding groups for FSI and TFSI, leading to a lower probability for arrangements prone to crystallization and making it less likely for nuclei to form in FTFSI-based electrolytes. Lower energy barriers for rotation

around the SNSF and SNSC dihedral angles have also been found in ab-initio studies for FTFSI (and FSI) compared to the barriers for TFSI anions.[16, 30]

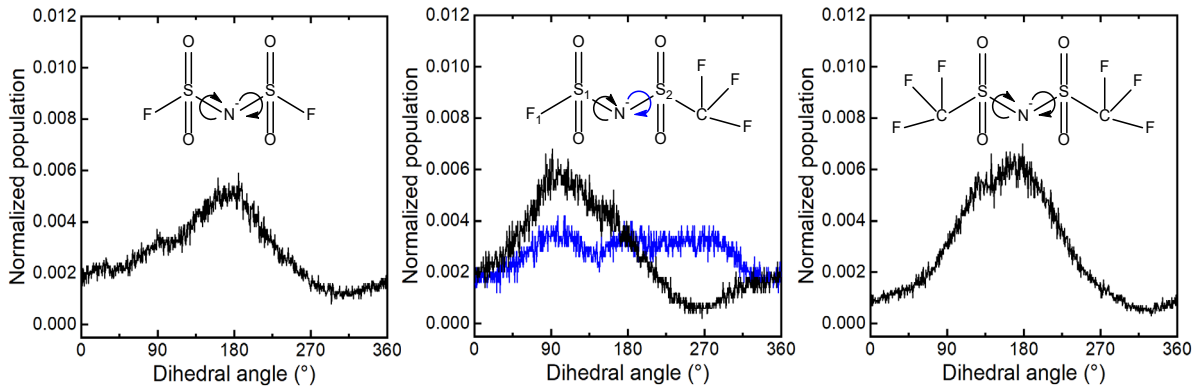

Figure 7-4 Normalized distribution of dihedral angles in 35m (a) LiFSI, (b) LiFTFSI, (c) LiTFSI. The colors correspond to the dihedral angles of (a) F-S-N-S (black) in FSI, (b) F_1-S_1-N-S_2 (black) and S_1-N-S_2-C (blue) in FTFSI, and (c) C-S-N-S (black) in TFSI.

We hypothesize that the high rotational mobility of the SO_2CF_3 group plays a crucial role in suppressing crystallization of FTFSI-based electrolytes by disturbing the surrounding electrolyte solvents and ions, impeding close packing of anions and cations, thus suppressing the crystallization processes, i.e. nucleation, subsequent growth, aggregation and intergrowth of crystals.[31] **Figure 7-5** schematically illustrates the local agitation resulting from asymmetric FTFSI anions.

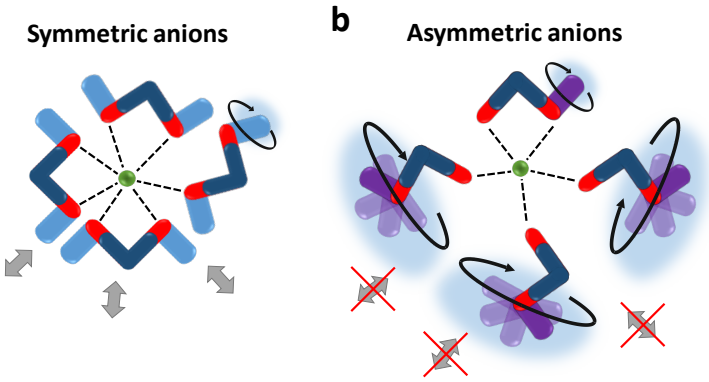

Figure 7-5 Schematic illustration of the difference in local coordination for (a) symmetric TFSI and (b) asymmetric FTFSI anions.

In addition, the asymmetry of the FTFSI anion itself might also play a role in the strong supercooling behavior of FTFSI-based electrolytes as it, in theory, reduces the probability for specific arrangements of the electrolyte species. In fact, the higher rotational mobility of the SO_2CF_3 group of FTFSI compared to TFSI is linked to the asymmetry of the FTFSI anion. To study

the effect of asymmetry per se on the supercooling behavior of highly concentrated electrolytes, one would have to identify a rigid asymmetric anion that does not possess the rotational degrees of freedom of FTFSI.

We note that for a quantitative understanding of the nucleation mechanism, advanced simulations with enhanced sampling methods should be conducted.[32] For example, the well-tempered metadynamics method[17, 18, 33] or constant chemical potential molecular dynamics[34] have proven successful in simulating nucleation of urea or sodium chloride from aqueous solution, respectively.

7.3 Conclusion

In summary, we investigated local solution structures in concentrated aqueous electrolytes based on LiFSI, LiFTFSI, and LiTFSI by means of Raman spectroscopy and MD simulations. The different coordination structures between cations and anions cause marked differences in the intramolecular rotational motion. Notably, the FTFSI anions coordinate lithium preferentially and asymmetrically through the SO_2F group, resulting in high mobility of the uncoordinated SO_2CF_3 group. This promoted bond rotation, enabled by the asymmetry of the FTFSI anion, should disturb the surrounding solvation structures, impeding close packing of anions and cations, thus leading to the enhanced supercooling behavior of FTFSI-containing electrolytes.

7.4 Supplementary Information

LiFSI (battery grade, Fluorochem), LiTFSI (99.9%, Solvionic), and LiFTFSI (≥98%, Provisco) were used as received. The electrolytes were prepared by dissolving the salts in high-purity water (prepared with a Millipore Milli-Q water purification system), which was previously degassed with argon.

Differential scanning calorimetry was carried out with a Netzsch STA 449 F3 simultaneous thermal analyzer. Approximately 30 mg of electrolyte sample were mixed with 1-2 mg of meso-carbon microbeads acting as crystallization agent and hermetically sealed in Al pans. The samples were equilibrated at 60 °C for 30 min before scanning to −120 °C followed by a scan back to 60 °C. The liquidus transitions were defined by their respective peak maxima. The scan rate for all measurements was set to 1 °C min^{-1}.

Raman spectra of electrolytes sealed in NMR tubes were collected on a Renishaw Ramascope using a 50 mW laser with a wavelength of 633 nm. The samples were heated to 60 °C in a water bath and immediately measured at room temperature.

Ionic conductivity was determined via impedance spectroscopy (Bio-Logic MCS 10) in sealed 2-electrode cells equipped with Pt electrodes (Bio-Logic HTCC). Viscosity was determined with an electromagnetically spinning viscometer (Kyoto Electronics Manufacturing EMS-1000) using 2 mm Al spheres. Sample volumes of 300 µL were used. The samples were equilibrated for 15 min at each temperature. Density at 60 °C was measured with an Anton Paar DMA 4100 M density meter.

Table 7-1 Physicochemical properties of the investigated electrolytes at 60 °C

Electrolyte	Liquidus temperature (°C)	Density (g/cm3)	Ionic conductivity (mS/cm)	Viscosity (mPa s)
35m LiFSI	28	1.788	33.6	19.7
35m LiFTFSI	18	1.769	13.4	37.7
35m LiTFSI	47	1.754	5.9	107

Classical molecular dynamics simulations were carried out using the *Amber16* software package. Periodic boundary conditions in all directions were applied. The particle-mesh Ewald procedure was used to calculate long-range electrostatic interactions. The General Amber Force Field (GAFF)[35] was used to describe the non-electrostatic interactions. Restrained electrostatic potential (RESP) charges were obtained by carrying out quantum chemical calculations at B3LYP/6-31+G(d,p) level of theory with the *Gaussian09* package. The partial charges of the atoms and Cartesian coordinates are listed in **Table 7-2** and **Table 7-3**, respectively. We note that determining the exact crystallization temperature or thermodynamic properties requires the use of a polarizable force field or scaled charges. However, as we here rather aim at identifying elements hindering molecular ordering, the limitations of the force field are not expected to affect our qualitative conclusion. All systems consist of 550 SPCF/Fw water molecules, 350 cations, and 350 anions to fit the experimental molecular ratio in 35m electrolytes (see **Table 7-4**). The systems were equilibrated at 333 K and 1 bar in the NPT ensemble (the mass densities and periodic box lengths are listed in **Table 7-4**). We then conducted 50 ns production runs at 333 K in the NVT ensemble with a time step of 0.2 fs. The *AmberTools* suite, *Cpptraj*, was used to analyze radial distribution functions (RDFs) and dihedral angles. *Visual Molecular Dynamics* (VMD) was used for the visualization of the MD trajectrories.[36]

Table 7-2 Partial charges of the atoms from the B3LYP/6-31+G(d,p) calculations.

Atom	Partial charge (e)
N (FSI)	-0.638319
S (FSI)	1.148009
O (FSI)	-0.523367
F (FSI)	-0.282116
N (FTFSI)	-0.662148
S1 (FTFSI)	1.170669
S2 (FTFSI)	1.046238
O1-2 (FTFSI)	-0.53147
O3-4 (FTFSI)	-0.542782
C (FTFSI)	0.337081
F1 (FTFSI)	-0.276493
F-CF3 (FTFSI)	-0.155614
N (TFSI)	-0.693373
S (TFSI)	1.074657
O (TFSI)	-0.551693
C (TFSI)	0.351583
F (TFSI)	-0.158723
O (Water)	-0.799231
H1 (Water)	0.399615
H2 (Water)	0.399615

Table 7-3 Cartesian coordinates for the optimized anions from the B3LYP/6-31+G(d,p) calculations.

FSI				FTFSI				TFSI			
N1	-0.001	0	-0.949	N1	-0.597	0.484	-0.008	N1	-0.024	-0.015	-1.309
S1	-0.049	1.48	-0.094	S1	0.168	1.757	0.84	S1	0.724	1.281	-0.482
S2	0.049	-1.48	-0.094	S2	-0.763	-1.053	0.724	S2	-0.742	-1.292	-0.427
O1	0.128	2.75	-1.164	O1	0.383	3.059	-0.183	O1	1.52	2.258	-1.579
O2	1.208	1.532	1.005	O2	1.665	1.249	1.377	O2	1.841	0.679	0.604
O3	-0.13	-2.749	-1.165	O3	-1.729	-2.024	-0.231	O3	-1.576	-2.292	-1.472
O4	-1.207	-1.532	1.006	O4	-1.49	-0.883	2.218	O4	-1.819	-0.666	0.685
F1	-1.439	1.603	0.667	F1	-0.736	2.183	2.077	C1	0.528	-2.215	0.412
F2	1.44	-1.603	0.665	C1	0.845	-1.793	0.912	F1	1.555	-2.44	-0.435
				F2	1.55	-1.633	-0.228	F2	0.024	-3.395	0.831
				F3	0.706	-3.11	1.175	F3	0.968	-1.51	1.476
				F4	1.497	-1.197	1.933	C2	-0.515	2.223	0.381
								F4	-1.572	2.429	-0.432
								F5	-0.916	1.543	1.476
								F6	0.004	3.412	0.756

Table 7-4 Simulation details of the investigated electrolytes.

Electrolyte	Molecules	Periodic box length (Å)	Density (g/cm^3)
35m LiFSI	550 Water, 350 Li^+ and 350 FSI^-	40.0045	1.9553
35m LiFTFSI	550 Water, 350 Li^+ and 350 $FTFSI^-$	43.6542	1.8541
35m LiTFSI	550 Water, 350 Li^+ and 350 $TFSI^-$	46.8046	1.7878

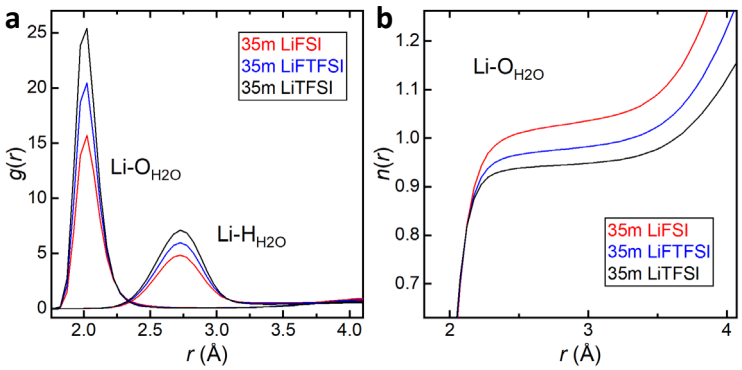

Figure 7-6 (a) Cation-water RDFs and (b) running integrals n(r) *of 35m LiFSI, LiFTFSI, and LiTFSI, respectively.*

The cation-water RDFs (**Figure 7-6** and **Table 7-5**) show that the first hydration shell extends to ca. 2.9 Å (defined by the first minimum in the cation-O_{water} RDF) for Li^+. The size of the first solvation shell and the hydration number, as extracted from the running integral of the RDF, *n*(*r*), at the distance corresponding to the first minimum in the RDF,[37, 38] marginally decrease with increasing anion size.

Table 7-5 Radius of solvation shells as determined by the first minimum in the cation-oxygen$_{water}$ RDFs and hydration numbers extracted from the corresponding running integrals n(r).

Radius (Å)	Hydration number
LiFSI: 2.91 LiFTFSI: 2.88 LiTFSI: 2.83	LiFSI: 1.03 LiFTFSI: 0.98 LiTFSI: 0.94

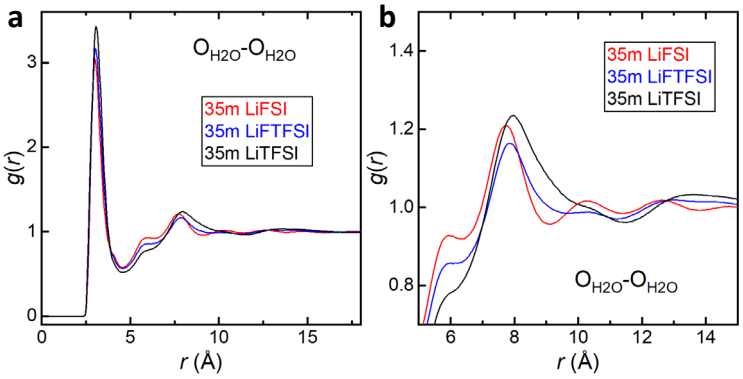

Figure 7-7 (a) Water-water RDFs of 35m LiFSI, LiFTFSI, and LiTFSI, respectively. Subfigure (b) is a magnification of (a).

In the water-water RDFs (**Figure 7-7**), the first peak around 3 Å corresponding to water molecules in the first solvation shell of a cation suggests slightly more water molecules are present in the first solvation shell with smaller anion size. We counted the number of water molecules within 3 Å from each other at an angle between $oxygen_{acceptor}$ - $hydrogen_{donor}$ - $oxygen_{donor}$ of at least 135 °, which is a common criterion for hydrogen-bonds.[39] We observe, in average, more hydrogen bonds between water molecules in electrolytes with smaller anions, see **Table 7-6**. We note that, as expected, the average number of hydrogen bonds is significantly lower than in bulk water, in agreement with previous reports.[39, 40] The peak around 6 Å, that we ascribe to the second solvation shell, decreases with increasing anion size (**Figure 7-7b**). It is intuitive that the distance between water molecules in the first and second solvation shell is larger when larger anions are located in between them.

Table 7-6 Hydrogen-bond analysis.

Electrolyte	Average number of hydrogen bonds
35m LiFSI	74
35m LiFTFSI	66
35m LiTFSI	60

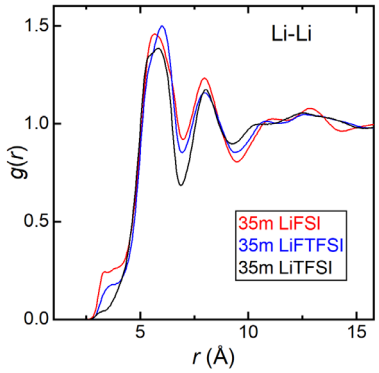

Figure 7-8 Cation-cation RDFs of 35m LiFSI, LiFTFSI, and LiTFSI, respectively.

In the cation-cation RDFs, the first peak around 3.5 Å decreases with increasing anion size (**Figure 7-8**). This trend corresponds to a higher chance of cations being this close to each other if separated by a smaller anion. The peak around 5.5 Å should be sensitive to the way the anions coordinate the cation as this influences the distance between two anion-separated cations. In fact, the peak is rather broad for all systems, suggesting that there are multiple cation-anion coordination schemes possible in all cases. In the case of 35m LiTFSI, the peak is slightly bifurcated, suggesting that there are two favored anion orientations.

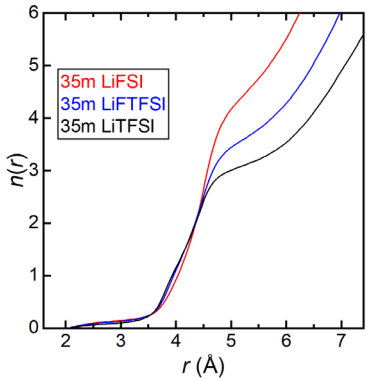

Figure 7-9 Running integral n(r) of the RDFs between lithium cations and nitrogen atoms of anions of 35m LiFSI, LiFTFSI, and LiTFSI, respectively.

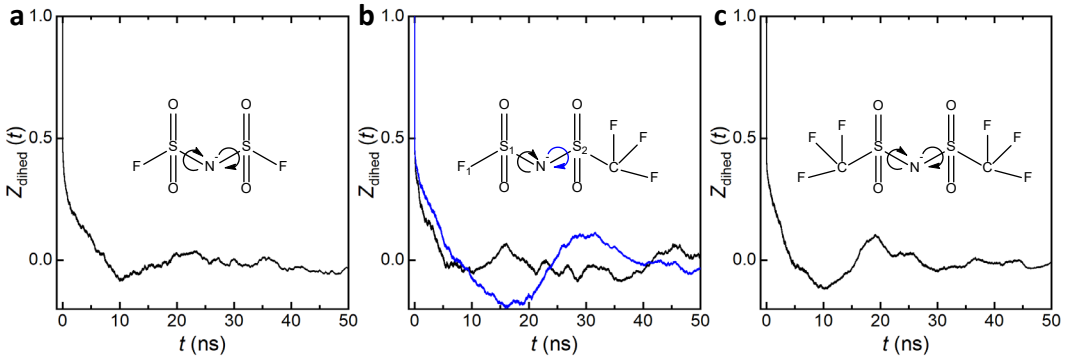

Figure 7-10 Autocorrelation functions (Z_{dihed}) of dihedral angles in 35m LiFSI, LiFTFSI, and LiTFSI respectively. The colors correspond to the dihedral angles of (a) F-S-N-S (black) in FSI, (b) F_1-S_1-N-S_2 (black) and S_1-N-S_2-C (blue) in FTFSI, and (c) C-S-N-S (black) in TFSI.

References

1. Suo, L., et al., *"Water-in-salt" electrolyte enables high-voltage aqueous lithium-ion chemistries.* Science, 2015. **350**(6263): p. 938-943.
2. Yamada, Y., et al., *Hydrate-melt electrolytes for high-energy-density aqueous batteries.* Nature Energy, 2016. **1**(10): p. 16129.
3. Kühnel, R.-S., D. Reber, and C. Battaglia, *A high-voltage aqueous electrolyte for sodium-ion batteries.* ACS Energy Letters, 2017. **2**(9): p. 2005-2006.
4. Suo, L., et al., *Advanced high-voltage aqueous lithium-ion battery enabled by "water-in-bisalt" electrolyte.* Angewandte Chemie International Edition, 2016. **55**(25): p. 7136-7141.
5. Suo, L., et al., *"Water-in-Salt" electrolytes enable green and safe Li-ion batteries for large scale electric energy storage applications.* Journal of Materials Chemistry A, 2016. **4**(17): p. 6639-6644.
6. Yang, C., et al., *4.0 V Aqueous Li-Ion Batteries.* Joule, 2017. **1**(1): p. 122-132.
7. Wang, F., et al., *Stabilizing high voltage LiCoO 2 cathode in aqueous electrolyte with interphase-forming additive.* Energy & Environmental Science, 2016. **9**(12): p. 3666-3673.
8. Leonard, D.P., et al., *Water-in-salt electrolyte for potassium-ion batteries.* ACS Energy Letters, 2018. **3**(2): p. 373-374.
9. Reber, D., R.-S. Kühnel, and C. Battaglia, *Suppressing Crystallization of Water-in-Salt Electrolytes by Asymmetric Anions Enables Low-Temperature Operation of High-Voltage Aqueous Batteries.* ACS Materials Letters, 2019. **1**: p. 44-51.
10. Zhang, N., et al., *Rechargeable aqueous zinc-manganese dioxide batteries with high energy and power densities.* Nature communications, 2017. **8**(1): p. 405.
11. Wang, F., et al., *Highly reversible zinc metal anode for aqueous batteries.* Nature materials, 2018. **17**(6): p. 543.
12. Kim, H., et al., *Aqueous rechargeable Li and Na ion batteries.* Chemical reviews, 2014. **114**(23): p. 11788-11827.

13. Reber, D., et al., *Stability of aqueous electrolytes based on LiFSI and NaFSI.* Electrochimica Acta, 2019. **321**: p. 134644.

14. Rey, I., et al., *Spectroscopic and theoretical study of (CF3SO2) 2N-(TFSI-) and (CF3SO2) 2NH (HTFSI).* The Journal of Physical Chemistry A, 1998. **102**(19): p. 3249-3258.

15. Umebayashi, Y., et al., *Lithium ion solvation in room-temperature ionic liquids involving bis (trifluoromethanesulfonyl) imide anion studied by Raman spectroscopy and DFT calculations.* The Journal of Physical Chemistry B, 2007. **111**(45): p. 13028-13032.

16. Giffin, G.A., et al., *Conformations and vibrational assignments of the (fluorosulfonyl)(trifluoromethanesulfonyl) imide anion in ionic liquids.* The Journal of Physical Chemistry C, 2013. **117**(46): p. 24206-24212.

17. Salvalaglio, M., et al., *Molecular-dynamics simulations of urea nucleation from aqueous solution.* Proceedings of the National Academy of Sciences, 2015. **112**(1): p. E6-E14.

18. Giberti, F., et al., *Insight into the nucleation of urea crystals from the melt.* Chemical Engineering Science, 2015. **121**: p. 51-59.

19. Bakker, A., et al., *Contact ion pair formation and ether oxygen coordination in the polymer electrolytes M [N (CF3SO2) 2] 2PEOn for M= Mg, Ca, Sr and Ba.* Polymer, 1995. **36**(23): p. 4371-4378.

20. Chen, F., P. Howlett, and M. Forsyth, *Na-ion solvation and high transference number in superconcentrated ionic liquid electrolytes: a theoretical approach.* The Journal of Physical Chemistry C, 2017. **122**(1): p. 105-114.

21. Ray, P., et al., *Structural investigations on lithium-doped protic and aprotic ionic liquids.* The Journal of Physical Chemistry B, 2017. **121**(20): p. 5279-5292.

22. Kerner, M., et al., *Ionic liquid based lithium battery electrolytes: fundamental benefits of utilising both TFSI and FSI anions?* Physical Chemistry Chemical Physics, 2015. **17**(29): p. 19569-19581.

23. Han, S.-D., et al., *Electrolyte solvation and ionic association V. Acetonitrile-lithium bis (fluorosulfonyl) imide (LiFSI) mixtures.* Journal of The Electrochemical Society, 2014. **161**(14): p. A2042-A2053.

24. Li, Z., G.D. Smith, and D. Bedrov, *Li+ Solvation and transport properties in ionic liquid/lithium salt mixtures: A molecular dynamics simulation study.* The Journal of Physical Chemistry B, 2012. **116**(42): p. 12801-12809.

25. Li, Z., et al., *Effect of organic solvents on Li+ ion solvation and transport in ionic liquid electrolytes: a molecular dynamics simulation study.* The Journal of Physical Chemistry B, 2015. **119**(7): p. 3085-3096.

26. Martinelli, A., et al., *Conformational evolution of TFSI− in protic and aprotic ionic liquids.* Journal of Raman Spectroscopy, 2011. **42**(3): p. 522-528.

27. Fujii, K., et al., *Anion conformation of low-viscosity room-temperature ionic liquid 1-ethyl-3-methylimidazolium bis (fluorosulfonyl) imide.* The Journal of Physical Chemistry B, 2007. **111**(44): p. 12829-12833.

28. Lesch, V., et al., *The influence of cations on lithium ion coordination and transport in ionic liquid electrolytes: a MD simulation study.* Physical Chemistry Chemical Physics, 2016. **18**(1): p. 382-392.

29. Kowsari, M., et al., *Molecular dynamics simulations of the structure and transport properties of tetra-butylphosphonium amino acid ionic liquids.* Physical Chemistry Chemical Physics, 2011. **13**(19): p. 8826-8837.
30. Canongia Lopes, J.N., et al., *Potential energy landscape of bis (fluorosulfonyl) amide.* The Journal of Physical Chemistry B, 2008. **112**(31): p. 9449-9455.
31. Linnikov, O., *Mechanism of precipitate formation during spontaneous crystallization from supersaturated aqueous solutions.* Russian Chemical Reviews, 2014. **83**(4): p. 343.
32. Sosso, G.C., et al., *Crystal nucleation in liquids: Open questions and future challenges in molecular dynamics simulations.* Chemical reviews, 2016. **116**(12): p. 7078-7116.
33. Barducci, A., G. Bussi, and M. Parrinello, *Well-tempered metadynamics: a smoothly converging and tunable free-energy method.* Physical review letters, 2008. **100**(2): p. 020603.
34. Karmakar, T., P.M. Piaggi, and M. Parrinello, *Molecular Dynamics Simulations of Crystal Nucleation from Solution at Constant Chemical Potential.* Journal of chemical theory and computation, 2019. **15**(12): p. 6923-6930.
35. Wang, J., et al., *Development and testing of a general amber force field.* Journal of computational chemistry, 2004. **25**(9): p. 1157-1174.
36. Humphrey, W., A. Dalke, and K. Schulten, *VMD: visual molecular dynamics.* Journal of molecular graphics, 1996. **14**(1): p. 33-38.
37. Impey, R., P. Madden, and I. McDonald, *Hydration and mobility of ions in solution.* The Journal of Physical Chemistry, 1983. **87**(25): p. 5071-5083.
38. Koneshan, S., et al., *Solvent structure, dynamics, and ion mobility in aqueous solutions at 25 C.* The Journal of Physical Chemistry B, 1998. **102**(21): p. 4193-4204.
39. Miyazaki, K., et al., *First-Principles Study on the Peculiar Water Environment in a Hydrate-Melt Electrolyte.* The journal of physical chemistry letters, 2019. **10**(20): p. 6301-6305.
40. Han, S., *Dynamic features of water molecules in superconcentrated aqueous electrolytes.* Scientific reports, 2018. **8**(1): p. 9347.

8 Anion Chaotropicity as Indicator for Water-in-Salt Electrolyte Stability

David Reber,[1,2] Ruben-Simon Kühnel,[1] and Corsin Battaglia[1]

[1]Laboratory Materials for Energy Conversion, Swiss Federal Laboratories for Materials Science and Technology, Empa, Überlandstrasse 129, 8600 Dübendorf, Switzerland

[2]Institut des Matériaux, École Polytechnique Fédérale de Lausanne, EPFL, Station 12, 1015 Lausanne, Switzerland

This chapter is submitted for publication in a peer-reviewed journal

Due to the limited solubility of most sodium-salts and the poor performance of the few reported highly soluble candidates, we systematically examine the role of the anion in highly concentrated electrolytes. We demonstrate that at high concentration, the anion has a crucial impact on solution structure and cell performance. We establish that high salt concentration alone does not guarantee desirable performance and recognize the low solubility of suitable salts as a major challenge. We discuss the need for alternative approaches like mixed organic/aqueous solvent electrolytes or the addition of ionic liquids to water-in-salt electrolytes, and demonstrate the latter approach in a preliminary cell chemistry. **Author contributions:** D.R. conceived the idea for this study. D.R. and R.-S.K. designed most experiments. D.R. carried out the experiments. D.R., R.-S.K., C.B. analyzed the data. D.R. prepared the figures and wrote the original draft of the manuscript. R.-S.K. and C.B. critically reviewed and edited the manuscript. All coauthors read and approved the final manuscript.

Abstract

Water-in-salt electrolytes have enabled the development of novel high-voltage aqueous lithium-ion batteries due to their wide electrochemical stability window. In this study, we explore why analogous sodium electrolytes have struggled to reach the same level of electrochemical stability. We compare solution structure and electrochemical stability for eleven different sodium salts, selected among the major classes of salts proposed for highly concentrated electrolytes. We relate the water environment established for each anion to its position in the Hofmeister series. We also discuss the importance of the solid-electrolyte interphase for stable battery performance and how it relates to the anion. We further show that the search for suitable sodium salts is complicated by the fact that higher salt concentrations are needed than for their lithium equivalents. Reaching such a high concentration of 25 to 30 mol/kg with one or a combination of multiple sodium salts that have the desired properties remains a major challenge. We conclude that alternative approaches such as mixed water/organic solvent or dual-cation electrolytes should be pursued to enable the development of high-voltage aqueous sodium-ion batteries. We demonstrate the potential of the mixed-solvent approach by showing that the water solubility of NaTFSI can be increased from 8 to 30 mol/kg in the presence of ionic liquids. Such a ternary electrolyte enables stable cycling of a 2 V-class sodium-ion battery based on the $NaTi_2(PO_4)_3$/$Na_2Mn[Fe(CN)_6]$ electrode couple for 300 cycles at 1C with a Coulombic efficiency of >99.5%.

8.1 Introduction

Highly concentrated aqueous electrolytes have attracted significant attention over the past five years due to their inherent non-flammability and relatively high electrochemical stability that enabled tremendous progress in terms of the energy density of aqueous batteries. The archetypal water-in-salt electrolytes offer electrochemical stability windows of ≥2.5 V compared to ca. 1.5 V for dilute aqueous electrolytes. This approach enabled the development of high-voltage aqueous lithium-ion batteries, narrowing the gap in voltage and energy density to state-of-the-art lithium-ion batteries based on flammable organic solvents that have a typical average cell voltage of 3.7 V.[1-3] Highly concentrated electrolytes with a wide electrochemical stability window are based on highly soluble perfluorinated sulfonylimide salts such as lithium bis(fluorosulfonyl)imide (FSI), (fluorosulfonyl)(trifluoromethanesulfonyl)imide (FTFSI), bis(trifluoromethanesulfonyl)imide (TFSI), (pentafluoroethanesulfonyl)(trifluoromethanesulfonyl)imide (PTFSI), or bis(pentafluoroethanesulfonyl)imide (BETI), sometimes in combination with related lithium trifluoromethanesulfonate (lithium triflate, LiOTf).[1-6] The best-performing electrolytes have high overall molalities of ≥20 moles of salt per kilogram of water (20 mol/kg, 20m).[1-10] Higher salt concentration is directly linked to increased electrochemical stability for these electrolytes as eventually almost all water molecules are "trapped" in the solvation shell of the cations. Additionally, incorporation of anions into the cation solvation shell at such high concentrations leads to an interphasial chemistry dominated by reduction of anions and the formation of an anion-derived solid-electrolyte interphase (SEI) on the anode surface that also contributes to the wide electrochemical stability window of water-in-salt electrolytes.[11-14]

Aqueous sodium, potassium, aluminum, or zinc chemistries based on the water-in-salt approach are also of great interest to the community, but their development is hindered by the relatively low solubility of the analogous imide and triflate salts at room temperature. Maximum concentrations at 25 °C are, e.g., 9m NaOTf, 8m NaTFSI, <2m KTFSI, <2m $Zn(TFSI)_2$, or <1m $Al(TFSI)_3$.[4, 15, 16] Due to the lower charge density of e.g. Na^+ compared to Li^+, sodium electrolytes need to have an even higher concentration than lithium electrolytes to achieve the same peculiar solution structure that enables high electrochemical stability, i.e. strong cation-water and cation-anion interactions.[17]

Consequently, highly concentrated electrolytes based on other types of salts with high solubilities, especially for sodium and potassium batteries, have been explored. In particular, nitrates, perchlorates, and acetates have been studied, and concentrations up to 40m have been achieved for eutectic mixtures of two different acetate salts.[18-24] Still, even at such high concentrations, most of these electrolytes do not nearly reach the electrochemical stability of

lithium imide/triflate electrolytes. In the case of sodium electrolytes, they are even outperformed by the much-lower-concentrated 9m NaOTf electrolyte.[4] This lack of electrochemical stability is often not immediately apparent in cells reported in literature due to the choice of low-voltage anode-cathode couples,[25-29] the use of high C-rates,[20-23, 25, 28-32] excess electrolyte that compensates low efficiencies,[22] overly optimistic electrochemical stability windows determined by high-scan-rate linear sweep voltammetry experiments,[21-23, 29-34] and/or by generally demonstrating only few cycles.[19, 20, 23, 26, 27, 31, 33-36]

Apparently, the anion plays a crucial role in solution structure as well as SEI-forming ability of highly concentrated electrolytes, with large consequences for electrochemical stability and battery performance. Molecular dynamics studies already revealed that in concentrated solutions water-cation, water-water, and cation-anion interactions, i.e. ion-pairing and agglomeration, are highly sensitive to the nature of the anion.[37] The influence of the anion on solution structure was recently also studied experimentally for saturated solutions of $NaClO_4$, NaOTf, LiTFSI, $NaNO_3$, and Na_2SO_4. However, the large range of saturation concentrations for these salts (1 to 17m) makes comparison of the results for the different anions difficult.[24]

Here, we systematically compare highly concentrated aqueous electrolytes based on eleven sodium salts and demonstrate the tremendous influence the anion has on solution structure and suitability for aqueous high-voltage batteries. We determine the minimum sodium salt concentration needed to support stable cycling of 2 V-class $NaTi_2(PO_4)_3/Na_3(VOPO_4)_2F$ and $NaTi_2(PO_4)_3/Na_2Mn[Fe(CN)_6]$ batteries and show that besides solubility, high chaotropicity according to the Hofmeister series is a key property of suitable sodium salts. The anion's ability to form a stable SEI is further discussed as a crucial factor for good cell performance. We also screen combinations of eleven anions, highlighting the difficulty of finding suitable sodium salt blends that enable effective water-in-salt electrolytes. Finally, we provide an overview over multiple alternative approaches towards high-voltage aqueous batteries and present excellent cycling data for a $NaTi_2(PO_4)_3/Na_2Mn[Fe(CN)_6]$ cell containing a highly concentrated electrolyte based on a mixed water/ionic liquid solvent system.

8.2 Results and Discussion

Raman spectra in the wavenumber region corresponding to the OH stretching vibrations of water molecules can be used to investigate the impact of solutes on the water environment and to assess the electrochemical stability of water-in-salt electrolytes.[1, 2, 5] Pure water displays broad bands in this region due to different hydrogen-bonding environments in bulk water,[38] whereas in highly concentrated electrolytes ideally all water molecules are coordinated to cations, resulting in a relatively narrow peak at ~3550 cm^{-1}. **Figure 8-1a** and **b** show the

normalized Raman spectra in this region for 10m sodium acetate (NaOAc), $NaNO_3$, NaSCN, and $NaClO_4$, or 8m NaOTf, NaFSI, NaFTFSI, NaTFSI, and NaPTFSI, respectively. Concentrations of 10m and 8m were chosen due to the maximum solubility of the least soluble salt in each series ($NaNO_3$ (10m) and NaTFSI (8m), respectively). In **Figure 8-1a**, we also show 10m NaPTFSI for easier comparison between **Figure 8-1a** and **b**. For comparison with the spectrum of an effective, i.e. electrochemically stable, water-in-salt electrolyte, we also included 21m LiTFSI in both figures.

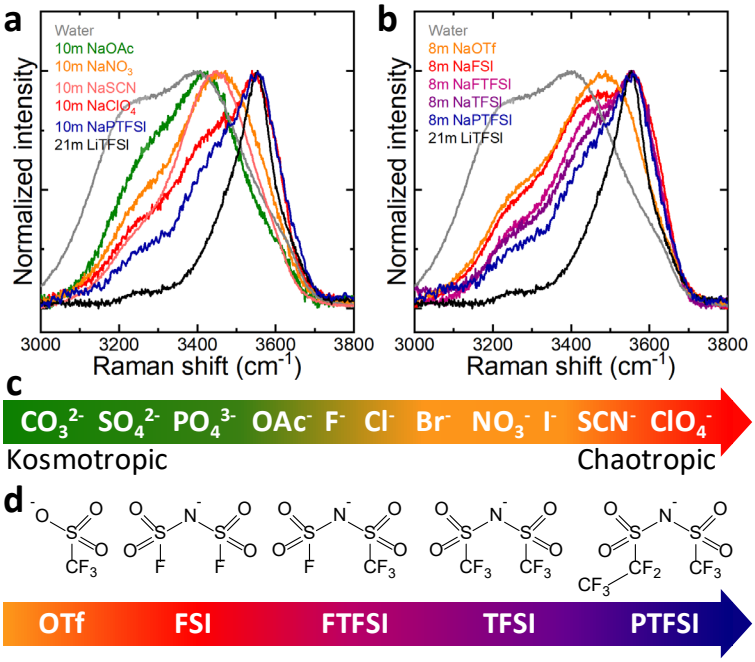

Figure 8-1 Normalized Raman spectra in the wavenumber region corresponding to O-H vibrations of water molecules for (a) 10m NaOAc, $NaNO_3$, NaSCN, $NaClO_4$, and NaPTFSI, (b) 8m NaOTf, NaFSI, NaFTFSI, NaTFSI, and NaPTFSI, and (a-b) 21m LiTFSI. (c) Typical Hofmeister series for anions in water with kosmotropes on the left and chaotropes on the right end of the series. (d) Chemical structures of the OTf, FSI, FTFSI, TFSI, and PTFSI anions with the colored bar indicating their position in the extended Hofmeister series according to (a-b).

Comparison at equimolar concentration reveals a significant dependence of this spectrum on the dissolved anion. 10m NaOAc shows a broad Raman signal resembling the one observed for pure water. For $NaNO_3$ and NaSCN, the spectrum starts to narrow and particularly the intensity of the shoulder around 3250 cm^{-1} decreases. For 10m $NaClO_4$ and NaPTFSI, the intensity of the peak around 3400 cm^{-1} further decreases and a prominent peak around 3550 cm^{-1} emerges. This peak is a typical feature of water-in-salt electrolytes and corresponds to water strongly coordinated to Li^+ (compare with spectrum for 21m LiTFSI also shown in Fig. 1a). These results show that for some anions such as acetate the solutions contain a relatively high fraction of bulk-like, i.e. pure-water-like, water molecules. In contrast, for anions such as perchlorate relatively more water is trapped in the cation solvation shell, indicating that water in these electrolytes is less prone to electrolysis. Interestingly, the trend in the water environment as indicated by the Raman spectra follows the empirical Hofmeister series, the typical

anion series is shown in **Figure 8-1c**, which originally described a trend in the minimum concentration of a salt needed to precipitate albumin protein from an aqueous solution.[39] Ions were later grouped into kosmotropes or structure makers with the ability to order the hydrogen-bonding network of water molecules beyond their first solvation shell, and chaotropes or structure breakers which lack this quality.[40] Thus, strongly hydrated kosmotropes, e.g. the acetate anion, form water-clusters, effectively removing water from the protein leading to its precipitation. Chaotropes like perchlorate on the other hand are only weakly hydrated.[41-44] A kosmotropic anion can therefore enhance ion pairing between cations and anions and influence, i.e. promote, the hydrogen-bonding network in bulk-like water domains.[37] This means that certain anions compete with water for a place in the cation solvation shell, thus freeing water molecules from this crucial trap which is at least in part responsible for the high overpotentials towards water electrolysis in water-in-salt electrolytes.[37] Note that at sufficiently high concentration, chaotropes are also incorporated into the cation solvation shell, which is considered a key requirement for the formation of an anion-derived SEI.[1, 2, 12] Charge density and polarizability as well as hydrophobicity of the ion are crucial factors governing its interaction with water and influencing overall solution structure.[45-48] Small variations such as reversal of the order of SCN and ClO_4 are common in the Hofmeister anion series shown in **Figure 8-1c**, depending on experimental parameters and on the criteria used to define the series. Therefore, it is more accurate to talk about ion-specific effects rather than insisting on a generally viable series with fixed values of kosmo-/chaotropicity.[41, 49, 50] We further note that these terms are heavily debated in macromolecular solution science as their definition typically ignores the crucial role of the protein surface.[51] However, we believe the concept presents a suitable basis for the discussion of the data presented here.

Figure 8-1d shows the chemical structures of the triflate and sulfonylimide anions considered for this study. Comparison with **Figure 8-1b** suggests higher chaotropicity with larger anion size and/or lower charge density, as indicated by the increasingly narrower signal around 3550 cm^{-1} in the order OTf>FSI>FTFSI>TFSI>PTFSI. The trend for the sulfonylimide anions could also be related to hydrophobicity as the number of hydrophobic fluorine atoms per anion increases in the same order.[52] Hydrophobic anions should push water into interaction with the cations, resulting in a narrower signal around 3550 cm^{-1}. In contrast to such chaotropic anions, kosmotropes gather bulk-like water in their solvation shell as indicated by the broad Raman signal around 3400 cm^{-1} for 10m NaOAc. Additionally, if the anion itself competes with water for a place in the cation solvation shell, the anions free water from the cation's sphere of influence thus contributing to the high fraction of bulk-like water visible in the Raman spectra. We therefore conclude that kosmotropic anions are not well suited for water-in-salt electrolytes as they promote bulk-like water, or free water, which reduces the electrochemical stability of the electrolyte.

To illustrate the effect of chaotropicity on the electrochemical stability of highly concentrated electrolytes, we prepared more concentrated solutions of $NaClO_4$ and NaOAc. These two salts have often been employed in concentrated electrolytes due to their high room temperature solubilities of 17 and 15m, respectively. **Figure 8-5a** compares linear sweep voltammetry data using gold electrodes for 15m NaOAc, 15m $NaClO_4$, and combinations of NaOAc and $NaClO_4$ of higher overall concentration as well as a 40-molal mixed NaOAc/KOAc electrolyte suggested in reference [31]. Even though 15m $NaClO_4$ has the lowest concentration among the investigated solutions, the linear sweep voltammetry data indicates that is has a higher oxidative stability than all the acetate-containing electrolytes. In fact, the oxidative stability of the acetate solutions appears to be hardly sensitive to concentration. **Figure 8-5b** shows the corresponding Raman spectra. As expected, the spectrum of 15m $NaClO_4$ narrows compared to the one of 10m NaClO4, resembling more and more the one of 21m LiTFSI (see again Fig. 1a). Interestingly, the spectra of the acetate-containing electrolytes do not converge to the typical narrow spectrum of water-in-salt electrolytes like 21m LiTFSI, not even at a concentration of 40m. In fact, when comparing the spectra for 15m NaOAc and 40m KOAc/NaOAc, the water environment as deduced from the spectra appears almost independent of the salt concentration, which might explain the modest performance of the reported battery employing this electrolyte.[31] Furthermore, when adding NaOAc to $NaClO_4$ electrolytes, the solution structure is negatively affected in the water-in-salt sense. This can be seen by the much higher signal intensity around 3400 cm^{-1}, representing bulk-like water, for 25m $Na(OAc)_{0.4}(ClO_4)_{0.6}$ or 25m $Na(Ac)_{0.6}(ClO_4)_{0.4}$ compared to 15m $NaClO_4$. This finding supports the hypothesis that the acetate anion not only gathers bulk-like water around itself due to its kosmotropic character but also frees water from the cation solvation shell. The Raman spectra for 10-molal solutions of other sodium salts of the carboxylate type like sodium formate (NaOFo) and sodium propionate (NaOPr) are very similar to the one for 10m NaOAc (**Figure 8-5c**). We conclude that carboxylates, although they have a high solubility, are not suitable for water-in-salt electrolytes, even in combination with other salts.

The high chaotropicity of $NaClO_4$ suggests that this anion is a promising candidate for water-in-salt electrolytes. However, besides its interaction with water, the ability of the anion to contribute to the formation of a stable SEI is also critically important to enable stable high-voltage operation. In this regard, it was recently shown that the perchlorate anion does not contribute to the formation of an SEI. [24] The reported formation of a hydroxide- and carbonate-containing SEI in perchlorate solutions, which appears to be not very effective, is rather the result of reduction of dissolved gases.[24] We suspect that this lack of an anion-derived SEI is a major factor in the poor performance of most aqueous high-voltage batteries and supercapacitors based on highly concentrated $NaClO_4$ electrolytes.[23, 26, 27, 33, 35, 36]

An electrolyte with a similar concentration of 18m but based on anions that are able to form an SEI was recently systematically developed in terms of maximizing salt concentration by Yamada et al.. In **Figure 8-2**, we compare 17m $NaClO_4$ with this 18-molal mixed NaPTFSI/NaTFSI/NaOTf electrolyte (mixed-imide electrolyte). The imide salts that the latter electrolyte contains are not only known to be able to form an SEI but and are also highly chaotropic in nature according to our Raman analysis (see again **Figure 8-1b**).[16] Despite the slightly higher concentration of the mixed-imide electrolyte, the linear sweep voltammetry and Raman spectroscopy data suggest better performance for the 17m $NaClO_4$ electrolyte as indicated by a wider stability window and a narrower Raman signal (see **Figure 8-2a** and **b**, respectively). However, the performance of full cells based on these two electrolytes shows a different picture. We compare their performance in 2 V-class $NaTi_2(PO_4)_3$ (NTP)/$Na_3(VOPO_4)_2F$ (NVPOF) (**Figure 8-2c-e**) as well as NTP/$Na_2Mn[Fe(CN)_6]$ (NaMnHCF) (**Figure 8-2f-h**) full cells cycled between 0.5 and 2.2 V at a rate of 1C. Surprisingly, the cells containing the mixed-imide electrolyte show higher capacity retention and Coulombic efficiency for both cell chemistries. Additionally, the voltage profiles in **Figure 8-2** show a faster increase in cell polarization upon cycling for the $NaClO_4$ compared to the mixed-imide electrolyte. These results highlight the importance of the electrolyte to form an SEI and exemplify that linear sweep voltammetry and Raman data should be carefully interpreted. We conclude that only full-cell cycling data can give reliable information on the practical electrochemical stability window of water-in-salt electrolytes.

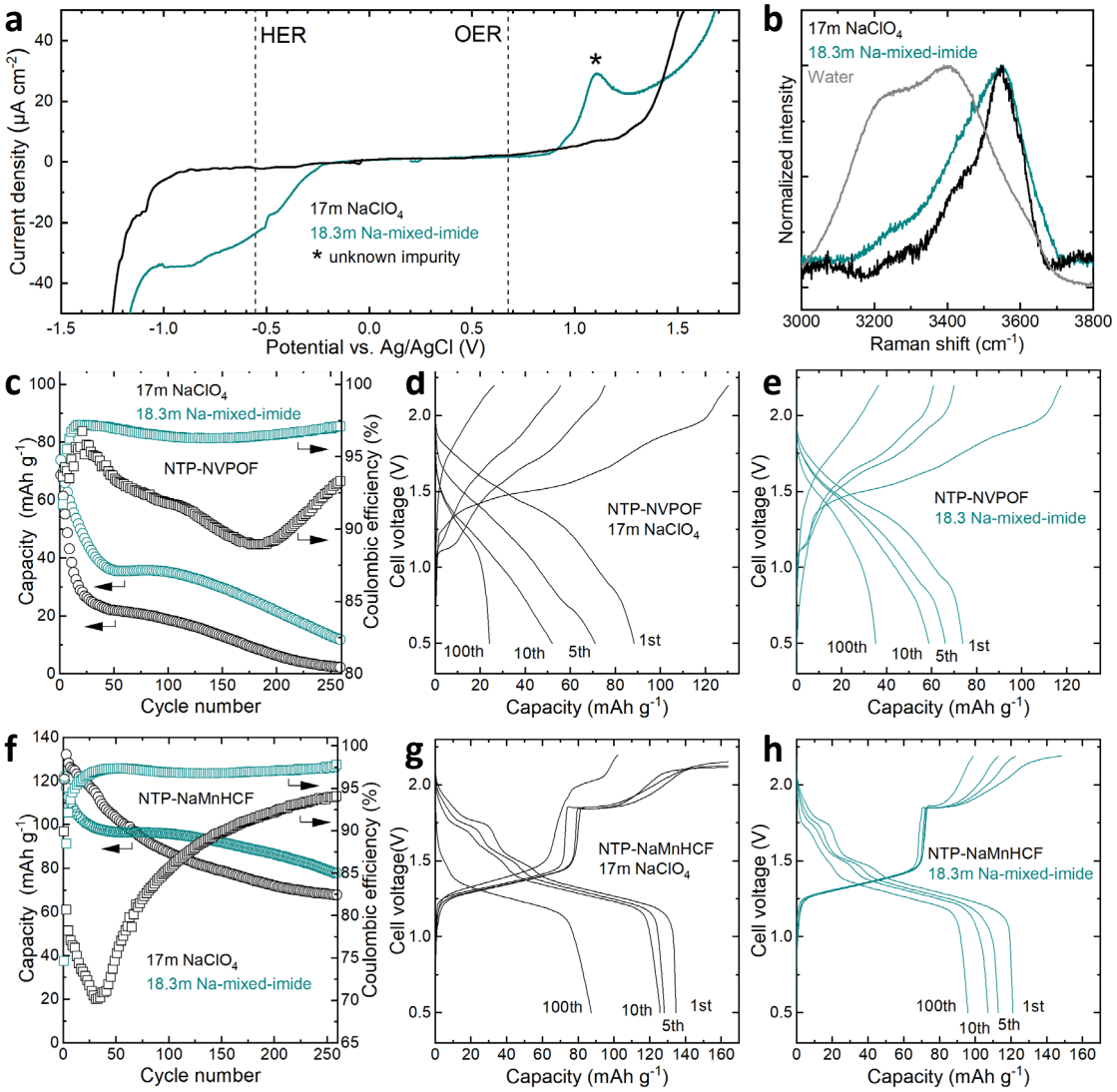

Figure 8-2 (a) Linear sweep voltammograms at a scan rate of 0.1 mV/s on gold electrodes and (b) normalized Raman spectra in the wavenumber region corresponding to O-H vibrations of water molecules for 17m $NaClO_4$ and 18.3m Na-mixed-imide electrolytes. In (a) the thermodynamic potentials for the hydrogen (HER) and oxygen evolution (OER) reactions at pH = 6 are indicated by dashed vertical lines. (c) Discharge capacity and Coulombic efficiency of NTP/NVPOF cells (mass ratio 1.2:1) cycled between 0.5 and 2.2 V at a rate of 1C (130 mA/g) in 17m $NaClO_4$ and 18.3m Na-mixed-imide electrolytes. (d-e) Corresponding voltage profiles. (f) Discharge capacity and Coulombic efficiency of NTP/NaMnHCF cells (mass ratio 2:1) cycled between 0.5 and 2.2 V at a rate of ca. 1C (140 mA/g). (g-h) Corresponding voltage profiles. Capacities and rates are based on the cathode active material mass.

Nevertheless, even with highly chaotropic anions capable of forming a stable SEI, the electrochemical stability of the 18-molal mixed-imide electrolyte is still insufficient for both these 2 V-class cell chemistries as demonstrated by Coulombic efficiencies of less than 97% and poor capacity retention. In fact, our recent study comparing highly concentrated aqueous electrolytes based on LiFSI and NaFSI indicated that sodium electrolytes need a higher concentration to reach the same level of stability than their lithium equivalents due to the lower charge density of Na^+ compared to Li^+.[17] The difference in stability is again demonstrated in **Figure 8-6** where we compare Raman spectra for 10 and 25m LiFSI and NaFSI electrolytes. At the same concentration, the LiFSI solutions show considerably smaller contributions from

bulk-like water compared to the NaFSI solutions, indicating that a higher Na- compared to Li-salt concentration is needed to reach the same level of electrochemical stability.

To identify the sodium salt concentration that enables the electrochemical stability of typical lithium water-in-salt electrolytes, we systematically studied the influence of sodium salt concentration on the cycling stability of 2 V-class full cells based on the electrode couples introduced with Figure 2. Stable cycling behavior has been demonstrated for comparable 2 V-class lithium-ion full cells employing e.g. the Mo_6S_8/$LiMn_2O_4$ or TiO_2/$LiMn_2O_4$ electrode couples in water-in-salt electrolytes with a concentration of 21 or 28m, respectively.[1, 3]

In **Figure 8-3**, we compare the cell performance of NTP/NVPOF and NTP/NaMnHCF full cells using 20, 25, 30, or 35m $Na(FSI)_{0.79}(FTFSI)_{0.29}$ as the electrolyte. Note that these electrolytes cannot be used for long-term operation due to the susceptibility of the fluorosulfonyl groups of the FSI and FTFSI anions towards hydrolysis.[17] Upon cycling, the cells containing the 20 or 25m electrolytes exhibit poor capacity retention and low Coulombic efficiencies of initially only 77-88% for both cell chemistries (see **Figure 8-3a-b** and **g-h**). Furthermore, the plateau-like features at high voltage visible in the voltage profiles clearly indicate extensive electrolyte decomposition at cell voltages above ca. 2 V (**Figure 8-3c-d** and **i-j**). In contrast, for 30 and 35m, the capacity retention is much better (**Figure 8-3a,g**). In addition, the Coulombic efficiencies of 98-99% (NTP-NVPOF) and 96-98% (NTP-NaMnHCF) are significantly higher (**Figure 8-3b,h**). There is also less polarization visible in the voltage profiles and the plateaus indicating electrolyte decomposition at high voltage are absent (**Figure 8-3e,f,k,l**). We assume that the lower initial capacity recorded for the cells containing the electrolytes with concentrations of ≥30m is related to the higher viscosity of these electrolytes (62 and 124 mPa s at 25 °C for 30 and 35m, respectively) compared to 20 and 25m (22 and 39 mPa s, respectively). Interestingly, the transition from poor performance to rather stable cycling behavior takes place at an electrolyte concentration between 25m and 30m. We note that a concentration of 27.5m corresponds to a water-to-cation ratio of 2 to 1.

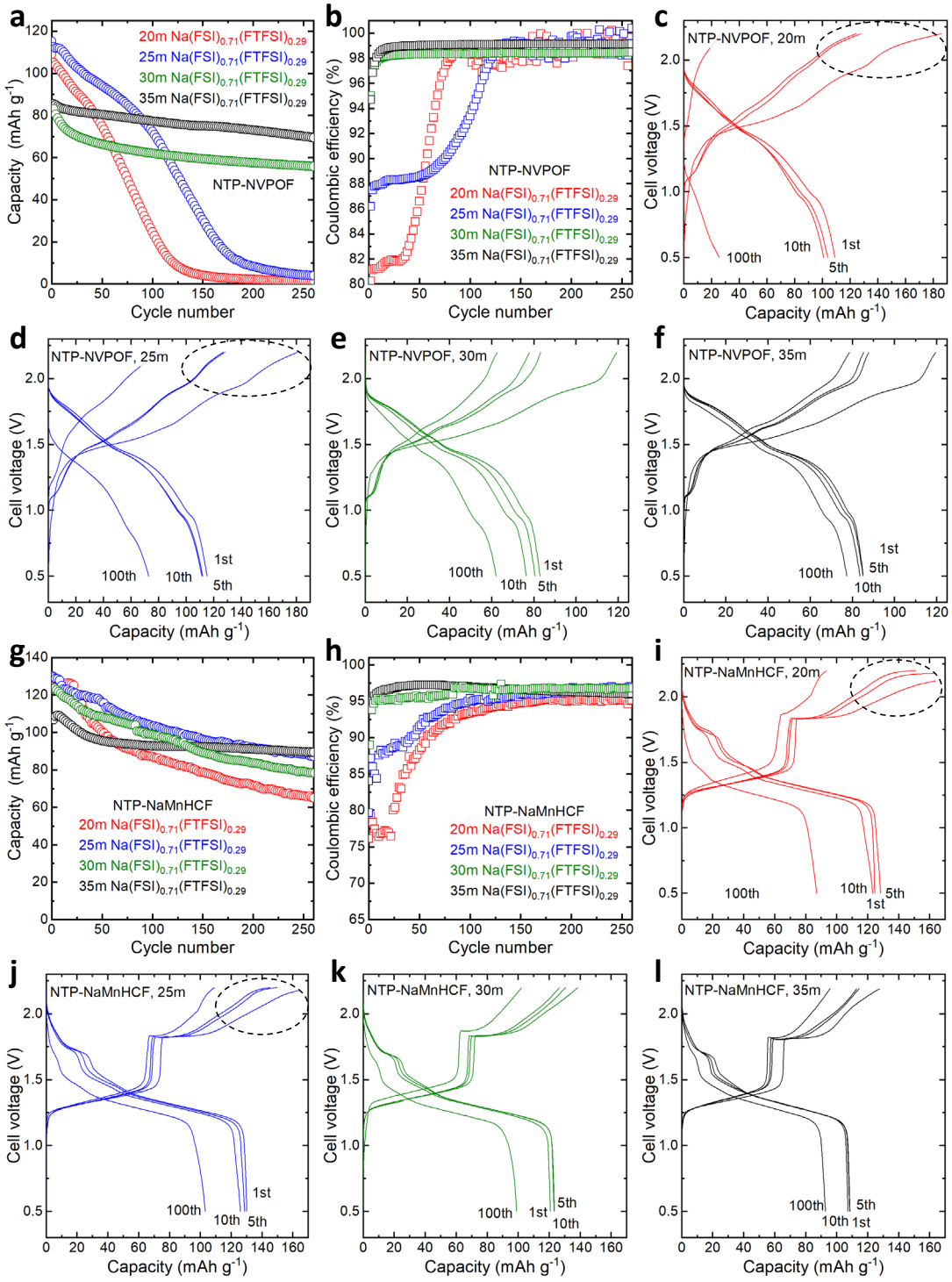

Figure 8-3 (a) Discharge capacity and (b) Coulombic efficiency of NTP/NVPOF cells (mass ratio 1.2:1) cycled between 0.5 and 2.2 V at a rate of 1C (130 mA/g) using 20m, 25m, 30m, or 35m $Na(FSI)_{0.79}(FTFSI)_{0.29}$ as the electrolyte. (c-f) Corresponding voltage profiles. (g) Discharge capacity and (h) Coulombic efficiency of NTP/NaMnHCF cells (mass ratio 2:1) cycled between 0.5 and 2.2 V at a rate of ca. 1C (140 mA/g) using 20m, 25m, 30m, or 35m $Na(FSI)_{0.79}(FTFSI)_{0.29}$ as the electrolyte. (c-f) Corresponding voltage profiles. Capacities and rates are based on the active material mass of the cathode.

The results of the cycling experiments show that even with anions with favorable properties, i.e. anions that are highly chaotropic and capable of forming a stable SEI, a concentration of >25m is needed for sodium electrolytes to enable stable cycling of 2 V-class batteries.

As both NaFSI and NaFTFSI are unsuitable for practical cells and no water-in-salt electrolyte with a concentration of >25m solely based on sodium salts is known to us, we investigated aqueous solutions containing multiple sodium salts. Combining two or more salts in one solution can enable a higher overall concentration due to e.g. a favorable gain in mixing entropy.[53, 54] We studied mixtures containing up to five sodium salts. The mixtures were principally investigated in terms of their liquidus temperature with the goal to maximize the salt concentration near room temperature. **Table 8-1** summarizes the more interesting combinations we identified. This work is complimentary to the systematic study recently conducted by Yamada et al. that resulted in the 18m mixed-imide electrolyte[16] presented in **Figure 8-2**.

With a respective liquidus temperature of 22 and 16 °C, 21m $Na(ClO_4)_{0.33}(PTFSI)_{0.33}(OTf)_{0.33}$ and 21m $Na(ClO_4)_{0.33}(PTFSI)_{0.24}(OTf)_{0.33}(TFSI)_{0.1}$ are among the most promising candidates that contain only suitable anions according to our previous analyses. However, in line with the results by Yamada et al., we found no combination rich in perfluorinated imide salt(s) with a concentration of >25m and a liquidus temperature of ≤20 °C. As a side note, several salt combinations with total concentrations of ≥20m where the anions differ significantly in size, e.g. perchlorate and PTFSI, result in biphasic systems. Such systems are potentially of interest for e.g. recycling applications or membrane-free flow batteries.[55, 56] We conclude that reaching a concentration of >25m at room temperature with one or multiple sodium salts that have the desired properties remains a major challenge.

These comprehensive studies show that other approaches are needed to improve the stability of high-voltage aqueous sodium-ion batteries. Several promising concepts have recently been introduced, particularly for lithium-ion batteries and electrolytes: Addition of acetonitrile as an organic co-solvent was shown to improve the SEI stability on the anode and thus enabled stable cycling of $Li_4Ti_5O_{12}/LiMn_2O_4$ and $Li_4Ti_5O_{12}/LiNi_{0.8}Co_{0.15}Al_{0.05}O_2$ full cells, while maintaining the non-flammability of aqueous electrolytes.[57] The presence of ionic liquids in water-in-salt electrolytes was recently shown to increase the solubility of suitable lithium salts such as LiTFSI. In this study, such a hybrid electrolyte with an ultra-high salt concentrations of 63m was proposed that enables stable cycling of the $Li_4Ti_5O_{12}/LiMn_2O_4$ electrode couple.[7] Another potential path forward is the development of new anions. Pseudo-delocalized sulfonate-amines are a promising candidate and have been recently incorporated in a 39-molal water-in-salt electrolyte.[9] Furthermore, instead of using mixed-anion electrolytes, combining multiple cations can also increase the overall concentration. Particularly if the second cation does not take place in the redox reactions of the battery, this approach can enable stable battery operation as recently demonstrated for a 31-molal electrolyte with the $NaTiOPO_4/Na_{1.88}Mn[Fe(CN)_6]_{0.97}\cdot 1.35H_2O$ electrode couple, which has a relatively high average

discharge voltage of 1.7 V.[8] Finally, water-containing deep eutectic solvents are another avenue that recently enabled high-voltage aqueous cell chemistries.[58]

To demonstrate the potential of these approaches, we here employ the concept of increasing the conducting salt solubility by using a mixed water/ionic liquid solvent system for the first time for sodium electrolytes. Remarkably, the solubility of both NaOTf and NaTFSI can be boosted from 9 and 8m, respectively, to 30m in the presence of 1-ethyl-3-methylimidazolium (EMIm)-based ionic liquids. We prepared four electrolytes with overall molalities of 50 and 80m. The 50-molal $NaOTf_{0.4}EMImOTf_{0.6}$ and $NaTFSI_{0.4}EMImTFSI_{0.6}$ electrolytes have remained liquid in our lab at room temperature for more than four weeks. Furthermore, differential scanning calorimetry (DSC) heating scans indicate liquidus temperatures below 20 °C for these electrolytes (see **Figure 8-7**). The ionic conductivity of the OTf electrolyte at 25 °C (16 mS cm^{-1}) is higher than for the TFSI mixture (8 mS cm^{-1}). This difference is in part due to the smaller size of the OTf compared to the TFSI anion. However, the lower chaotropicity of OTf compared to TFSI might also play a role by leading to a higher fraction of bulk-like water for the former anion (see difference in the Raman spectrum shown in **Figure 8-8**). Importantly, the conductivity of these electrolytes is significantly higher than that of a comparable 63-molal lithium electrolyte reported in literature (0.9 mS cm^{-1})[7] , in agreement with the higher charge density of Li^+ compared to Na^+. The 80-molal $NaOTf_{0.375}EMImOTf_{0.625}$ and $NaTFSI_{0.375}EMImTFSI_{0.625}$ mixtures form a translucent gel upon undisturbed storage over two weeks, although no corresponding thermal event is observed in DSC (see again **Fig. S3**). We note that gel formation in such highly concentrated electrolytes was recently predicted in a theoretical study.[59] We do not report conductivities for the 80-molal electrolytes as gelation is expected to be an important yet unexplored factor influencing ionic transport.

We then integrated these electrolytes into full cells based on the NTP/NaMnHCF electrode couple introduced above (**Figure 8-4**). At both concentrations, the TFSI-based electrolytes outperform their triflate analogues in terms of Coulombic efficiency and capacity retention; in agreement with the difference in chaotropicity between the two anions (see again **Figure 8-1b**). The cells containing the 50- and 80-molal NaTFSI/EMImTFSI electrolytes show a high initial Coulombic efficiency of 83.3% and 90.3%, respectively, and reach very high values of 99.4% and 99.8% after 300 cycles at 1C. The high efficiency obtained with the 80-molal TFSI electrolyte, results in an excellent capacity retention of 79% after 300 cycles. In comparison, the cells with the NaOTf/EMImOTf electrolytes have lower initial Coulombic efficiencies of 68.2% (50m) and 83.3% (80m), reaching 96.4% and 99.2% after 300 cycles at 1C, respectively. The later efficiency is still significantly higher than the steady-state value of 98% reached with the 35-molal NaFSI/NaFTFSI electrolyte (see again **Figure 8-3h**). The voltage profiles of the

cells containing the ionic liquid-based 50-molal electrolytes (**Figure 8-10a** and **c**) strongly resemble the one of the 20-molal NaFSI/NaFTFSI cell shown in **Figure 8-3i**, with plateaus at high voltage suggesting electrolyte decomposition in the first cycles. This feature is more pronounced for the triflate- compared to the TFSI-based electrolyte, again in agreement with the trend in chaotropicity. This result shows that even in solutions containing 30m of an imidazolium-based ionic liquid, a sodium concentration of 20m is again insufficient to enable high electrochemical stability. Hence, the ionic liquid plays only a negligible role in stabilizing the electrolyte and its main role is to increase the sodium salt solubility. In contrast, the voltage profiles of the cells containing the 80-molal electrolytes do not show a decomposition plateau at high voltage (**Figure 8-10b** and **d**), similar to the cells with the 30- and 35-molal NaFSI/NaFTFSI electrolytes (see again **Figure 8-3k** and **l**). These results demonstrate that mixed water/ionic liquid solvents systems are promising way to realize high-voltage aqueous sodium-ion batteries.

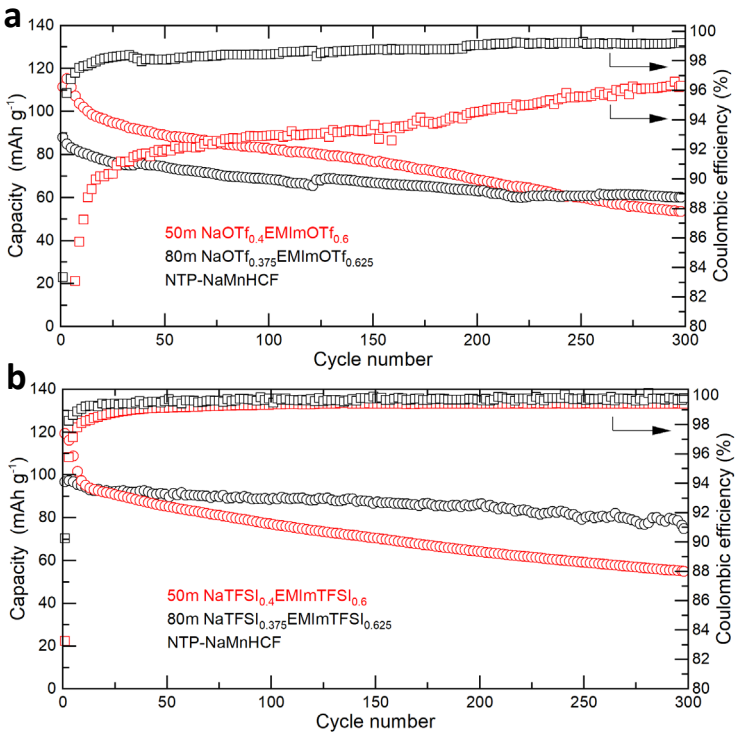

Figure 8-4 Discharge capacity and Coulombic efficiency of NTP/NaMnHCF fulls cells (mass ratio 2:1) cycled between 0.5 and 2.2 V at a rate of ca. 1C (140 mA/g) using (a) 50m NaOTf$_{0.4}$EmiOTf$_{0.6}$, (b) 80m NaOTf$_{0.375}$EmiOTf$_{0.625}$, (c) 50m NaTFSI$_{0.4}$EmiTFSI$_{0.6}$, and (d) 80m NaTFSI$_{0.375}$EmiTFSI$_{0.625}$ as the electrolyte. Capacities and rates are based on the active material mass of the cathode.

8.3 Conclusions

In summary, we investigated eleven sodium salts, chosen among the major classes of anions proposed for highly concentrated electrolytes, in terms of their suitability for water-in-salt electrolytes. Our results show that at high salt concentration the nature of the anion has

a crucial effect on solution structure and performance in aqueous high-voltage batteries. Following the classification into chaotropic and kosmotropic ions according to the Hofmeister series, we demonstrate that kosmotropes such as acetate are unsuitable for high-voltage applications as they promote the formation of bulk-like water clusters that are prone to hydrolysis. Suitable anions also need the ability to act as an SEI-former to further suppress the hydrogen evolution reaction. However, some common chaotropic anions such as perchlorate do not have this ability, which explains the relatively poor cycling stability of high-voltage cells based on such electrolytes.

While several highly soluble lithium salts based on chaotropic and SEI-forming anions such as LiTFSI are known, it remains a great challenge to identify suitable sodium salts or salt combinations. Further complicating this search is the fact that most sodium salts often have a lower solubility than their lithium equivalents. In addition, our results show that sodium electrolytes require a 5 to 10 mol/kg higher concentration than their lithium equivalents to reach comparable electrochemical stability. After conducting an intensive search combining up to five different sodium salts, we conclude that "classical" sodium water-in-salt electrolytes currently do not exist and alternative approaches should be further explored. The use of mixed water/organic solvent systems, dual-cation electrolytes, and non-electrolyte approaches like electrode coatings are all potential avenues to enable high-voltage aqueous sodium-ion batteries. For the example of a mixed water/ionic liquid solvent system, we demonstrate that the solubility of NaTFSI can be boosted from 8 to 30 mol/kg with respect to water, increasing the electrochemical stability of the solution to the level of common lithium water-in-salt electrolytes. This new hybrid electrolyte enables stable operation of a 2 V-class sodium-ion battery based on the $NaTi_2(PO_4)_3$/$Na_2Mn[Fe(CN)_6]$ electrode couple for 300 cycles at 1C with a Coulombic efficiency of >99.5%.

8.4 Methods

Sodium formate (NaOFo) (99%, Sigma-Aldrich), sodium acetate (NaOAc) (99%, Sigma-Aldrich), sodium propionate (NaOPr) (99%, Sigma-Aldrich), $NaNO_3$ (99.99%, Fluka), NaSCN (98%, Sigma-Aldrich), $NaClO_4$ (>98%, Sigma-Aldrich), sodium trifluoromethanesulfonate (sodium triflate, NaOTf) (98%, Thermo Fischer), NaFSI (99.7%, Solvionic), NaFTFSI (≥98%, Provisco), NaTFSI (99.5%, Solvionic), NaPTFSI (98%, Provisco), LiFSI (battery grade, Fluorochem), LiTFSI (99.9%, Solvionic), potassium acetate (KOAc) (99%, Sigma-Aldrich), EMImOTf (99.5%, Solvionic), and EMImTFSI (99.9%, Solvionic) were used as received. Electrolytes were prepared by dissolving the salt(s) in high-purity water (Millipore Milli-Q) which was previously purged with argon.

Raman spectra of electrolytes sealed in NMR tubes were collected at room temperature on a Renishaw Ramascope using a 50 mW laser with a wavelength of 633 nm.

Electrochemical stability windows at 25 °C were determined via linear sweep voltammetry on a gold working electrode (diameter of 1 mm, eDAQ), using a miniature Ag/AgCl reference electrode (eDAQ), and a Pt-coated Ti rod (eDAQ) counter electrode in a small volume glass cell (eDAQ) with a Bio-Logic VMP3 electrochemical workstation. The electrolyte volume was ca. 600 µL and the scan rate was set to 0.1 mV s^{-1}. Separate experiments were carried out to determine the cathodic and anodic stability. Ionic conductivity was determined via impedance spectroscopy (Bio-Logic MCS 10) in sealed 2-electrode cells equipped with Pt electrodes (Bio-Logic HTCC).

Differential scanning calorimetry was carried out with a Netzsch STA 449 F3 simultaneous thermal analyzer. Ca. 40 mg of electrolyte sample were mixed with 1-2 mg of meso-carbon microbeads acting as crystallization agent and hermetically sealed in Al pans. The samples were equilibrated at 60 °C for 30 min before scanning to −120 °C followed by a scan back to 60 °C. The liquidus transitions were defined by their respective peak maxima. The scan rate for all measurements was set to 1 °C min^{-1}.

$NaTi_2(PO_4)_3$ and $Na_3(VOPO_4)_2F$ were synthesized via solid-state routes according to reference[6]. $Na_2Mn[Fe(CN)_6]$ was synthesized via co-precipitation according to reference[60]. Powder X-ray diffractograms of the active materials were recorded with a Panalytical X- X'pert PRO MRD using Cu $K\alpha_1$ radiation. See **Fig. S6** for a diffractogram of the $Na_2Mn[Fe(CN)_6]$ powder prepared by us.

Electrodes with a diameter of 12 mm and an active material mass loading of 2 to 5 mg cm^{-2} were prepared from *N*-methyl-2-pyrrolidone (NMP)-based slurries on aluminum (NTP) and titanium (NVPOF, NaMnHCF) current collectors, respectively. The composition of the electrodes was 80% active material, 10% polyvinylidene difluoride binder (Arkema Kynar HSV900), and 10% carbon black (IMERYS Graphite & Carbon C-NERGY SUPER C65). 2-electrode coin cells were assembled using Whatman GF/D glass microfiber filters as separator and 100 µl of electrolyte. The cells were cycled at 25 °C.

8.5 Supplementary Information

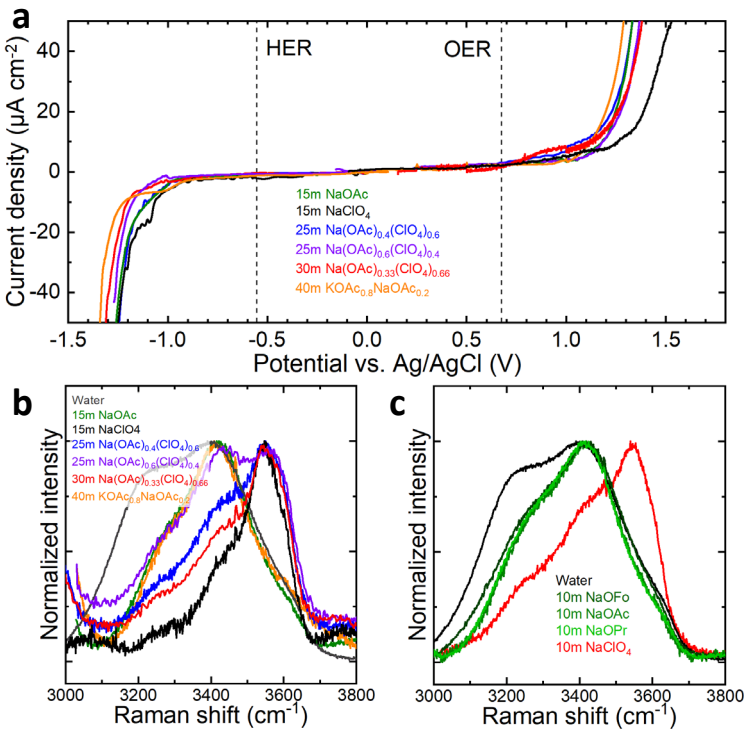

Figure 8-5 (a) Linear sweep voltammograms of 15m NaOAc, 15m $NaClO_4$, 25m $Na(OAc)_{0.4}(ClO_4)_{0.6}$, 25m $Na(OAc)_{0.6}(ClO_4)_{0.4}$, 30m $Na(OAc)_{0.33}(ClO_4)_{0.66}$, and 40m $KOAc_{0.8}NaOAc_{0.2}$ aqueous electrolytes on gold electrodes at a scan rate of 0.1 mV/s. The thermodynamic potentials for the hydrogen (HER) and oxygen evolution (OER) reactions at pH = 6 are indicated by dashed vertical lines. (b-c) Raman spectra in the wavenumber region corresponding to O-H vibrations of water molecules for (b) 15m NaOAc, 15m NaClO4, 25m $Na(OAc)_{0.4}(ClO_4)_{0.6}$, 25m $Na(OAc)_{0.6}(ClO_4)_{0.4}$, 30m $Na(OAc)_{0.33}(ClO_4)_{0.66}$, and 40m $KOAc_{0.8}NaOAc_{0.2}$, and (c) 10m NaOFo, NaOAc, NaOPr, and $NaClO_4$

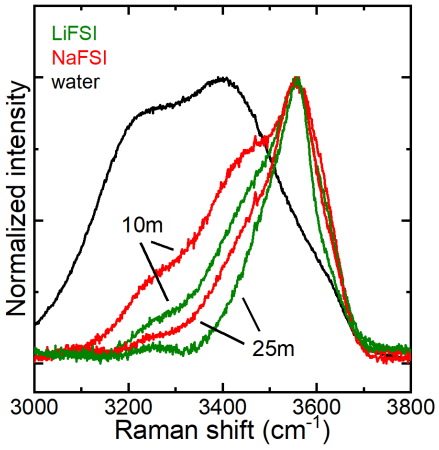

Figure 8-6 Raman spectra in the wavenumber region corresponding to O-H vibrations of water molecules for NaFSI and LiFSI electrolytes with concentrations of 10 and 25m.

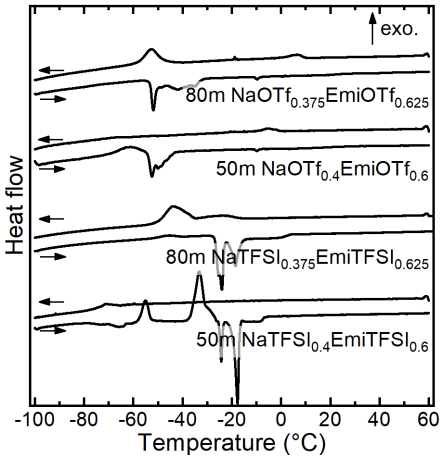

Figure 8-7 DSC cooling and heating curves of 50m $NaOTf_{0.4}EmiOTf_{0.6}$, 80m $NaOTf_{0.375}EmiOTf_{0.625}$, 50m $NaTFSI_{0.4}EmiTFSI_{0.6}$, and 80m $NaTFSI_{0.375}EmiTFSI_{0.625}$ recorded at a scan rate of 1 K min^{-1}.

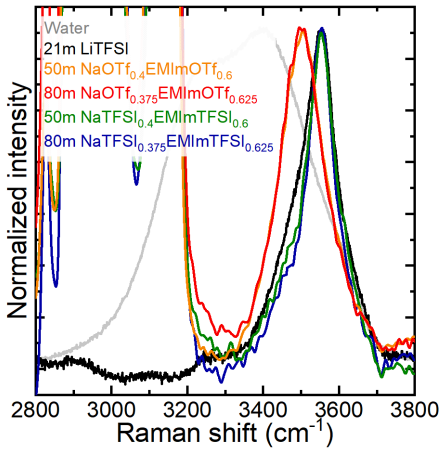

Figure 8-8 Normalized Raman spectra in the wavenumber region corresponding to O-H vibrations of water molecules for 21m LiTFSI, 50m $NaOTf_{0.4}EMImOTf_{0.6}$, 80m $NaOTf_{0.375}EMImOTf_{0.625}$, 50m $NaTFSI_{0.4}EMImTFSI_{0.6}$, and 80m $NaTFSI_{0.375}EMImTFSI_{0.625}$. The strong bands occurring between 2800 and 3200 cm^{-1} are assigned to C-H stretching modes of the cation.[61]

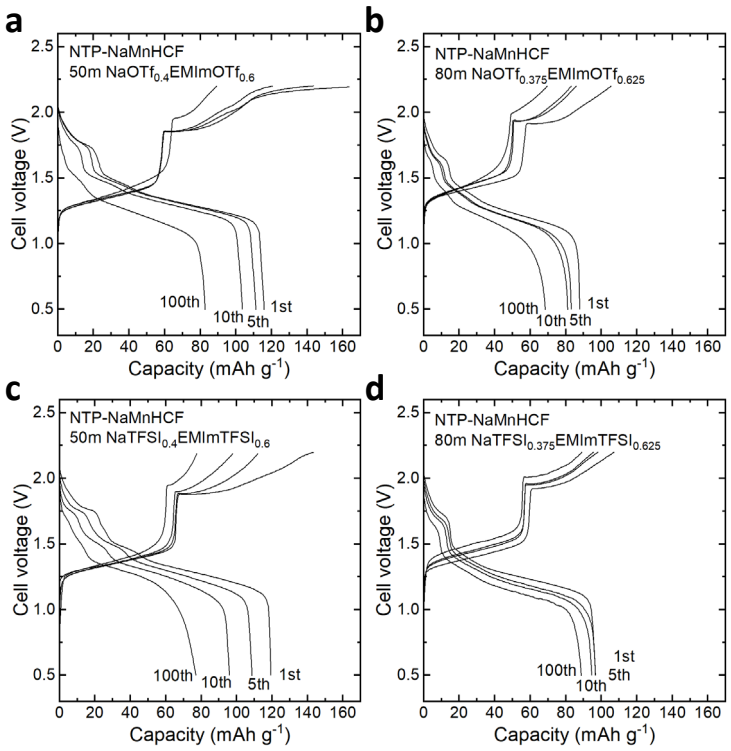

Figure 8-9 Voltage profiles of the NTP/NaMnHCF fulls cells shown in Fig. 4. The cells were cycled between 0.5 and 2.2 V at a rate of ca. 1C (140 mA/g) using (a) 50m $NaOTf_{0.4}EMImOTf_{0.6}$, (b) 80m $NaOTf_{0.375}EMImOTf_{0.625}$, (c) 50m $NaTFSI_{0.4}EMImTFSI_{0.6}$, and (d) 80m $NaTFSI_{0.375}EMImTFSI_{0.625}$ as the electrolyte. Capacities and rates are based on the active material mass of the cathode. The anode to cathode active material mass ratio was 2:1.

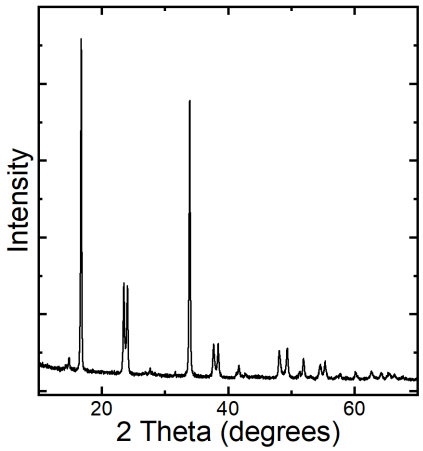

Figure 8-10 X-ray diffractogram of $Na_2Mn[Fe(CN)_6]$ (NaMnHCF) prepared by us. The pattern corresponds to the one reported in reference 60.

Table 8-1 Selected combinations of sodium salts and their approximate liquidus temperatures (T_L). (OFo = formate, OAc = acetate, OPr = proprionate, OTf = triflate)

Molality (mol/kg)													
OFo	**OAc**	**OPr**	**NO_3**	**ClO_4**	**SCN**	**OTf**	**FSI**	**FTFSI**	**TFSI**	**PTFSI**	**Total Conc.**	**T_L (°C)**	**Comments**
				7		7			2	5	21	16	
	15			10						5	30	18	
				6.3		6.3			2	6.3	21	18	
	15			5						10	30	19	
				10	15						25	21	SCN redox activity
				7		7				7	21	22	
				6.9		3.66			3.26	6.13	20	22	
						5		15		10	30	23	F-S bonds
	15									15	30	23	
				10		5				5	20	24	
	15			10							25	20-25	
								15		10	25	20-25	F-S bonds
							17.9	7.1			25	20-25	F-S bonds, supercooling
				15		5					20	20-25	
				10						10	20	20-25	biphasic, liquid
				15		2.5				2.5	20	20-25	biphasic, liquid
						4.6			3	14.3	22	27	
	12.5			5						12.5	30	29	
		10								15	25	25-30	
	20									10	30	25-30	
				5		5			5	5	20	25-30	
	12.5			12.5							25	25-30	
	10			15							25	25-30	
							5	15		10	30	25-30	F-S bonds
						5	5	15		10	35	25-30	F-S bonds
							21.4	8.6			30	25-30	F-S bonds, supercooling
	10			5						15	30	33	
	10			10						10	30	33	
	10			15						5	30	33	biphasic, part liquid at RT
				5						15	20	33.	
				12.5	12.5						25	34	SCN redox activity
	4.2					6.3				19.5	30	37	
						6.4		17.5		11.66	36	37	F-S bonds, supercooling
						5.8		17.5		11.66	35	38	F-S bonds, supercooling
							25	10			35	38	F-S bonds, supercooling
	7.5			2.5						20	30	39	SCN redox activity
				15	10						25	40	SCN redox activity
						6.3			4.2	19.5	30	41	
	10			20							30	44	
	5			5						20	30	46	
	20			10							30	>100	
	15					15					30	>100	
	15			15							30	>30	
				15		5				10	30	>30	
				15		7.5				7.5	30	>30	
				10		10				10	30	>30	
				15		10				5	30	>30	
				12		12			2.4	3.6	30	>30	
								10		15	25	>30	
							5	10		15	30	>30	F-S bonds
							10	10		15	35	>30	F-S bonds
						5		10		15	30	>30	F-S bonds
								18		12	30	>30	F-S bonds
								25		10	35	>30	F-S bonds
								21.4		8.6	30	>30	F-S bonds
								17.9		7.1	25	>30	F-S bonds
	20			5						5	30	>60	
	15					5				10	30	>60	
					9.5					9.5	19	>60	biphasic at 60, part liquid at RT
		5	5	5	5					5	25	>60	biphasic at 60, part liquid at RT
				10	10					5	25	>60	biphasic at 60, part liquid at RT
		5		5						15	25	>60	biphasic at 60, part liquid at RT

				15						5	20	>60	biphasic at 60, part liquid at RT
				17						3	20	>60	biphasic at 60, part liquid at RT
				10						20	30	>60	biphasic at 60, solid at RT
				20						10	30	>60	biphasic at 60, solid at RT
				15						10	25	>60	biphasic at 60, solid at RT
				15						15	30	>60	biphasic at 60, solid at RT
				10						15	25	>60	biphasic at 60, solid at RT
			10							10	20	>60	biphasic at 60, solid at RT
			8.3							12.5	21	>60	biphasic at 60, solid at RT
			5	5						10	20	>60	biphasic at 60, solid at RT
				5	10					15	30	>60	biphasic at 60, solid at RT
		10		5						10	25	>60	biphasic at 60, solid at RT
				13		4.2			2.8		20	>60	
	15					10				5	30	>80	
			10		15						25	>80	
			10	10	10						30	>80	
		5		10	10						25	>80	
	12.5	12.5									25	>80	
8.33	8.33	8.33									25	>80	
				15					5		20	>80	
				10		5			5		20	>80	biphasic
		10		15							25	>80	biphasic
		10			15						25	>80	

References

1. Suo, L., et al., *"Water-in-salt" electrolyte enables high-voltage aqueous lithium-ion chemistries.* Science, 2015. **350**(6263): p. 938-43.
2. Yamada, Y., et al., *Hydrate-melt electrolytes for high-energy-density aqueous batteries.* Nat. Energy, 2016. **1**: p. 16129.
3. Suo, L., et al., *Advanced High-Voltage Aqueous Lithium-Ion Battery Enabled by "Water-in-Bisalt" Electrolyte.* Angew. Chem., 2016. **55**(25): p. 7136-41.
4. Suo, L., et al., *"Water-in-Salt" Electrolyte Makes Aqueous Sodium-Ion Battery Safe, Green, and Long-Lasting.* Adv. Energy Mater., 2017. **7**(21): p. 1701189.
5. Kühnel, R.-S., D. Reber, and C. Battaglia, *A High-Voltage Aqueous Electrolyte for Sodium-Ion Batteries.* ACS Energy Lett., 2017. **2**(9): p. 2005-2006.
6. Reber, D., R.-S. Kühnel, and C. Battaglia, *Suppressing Crystallization of Water-in-Salt Electrolytes by Asymmetric Anions Enables Low-Temperature Operation of High-Voltage Aqueous Batteries.* ACS Materials Letters, 2019: p. 44-51.
7. Chen, L., et al., *A 63 m Super-concentrated Aqueous Electrolyte for High Energy Li-ion Batteries.* ACS Energy Letters, 2020.
8. Jiang, L., et al., *High-Voltage Aqueous Na-Ion Battery Enabled by Inert-Cation-Assisted Water-in-Salt Electrolyte.* Advanced Materials, 2019: p. 1904427.
9. Forero-Saboya, J., et al., *Water-in-Bisalt Electrolyte with Record Salt Concentration and Widened Electrochemical Stability Window.* The journal of physical chemistry letters, 2019. **10**(17): p. 4942-4946.
10. Ko, S., et al., *Lithium-salt monohydrate melt: A stable electrolyte for aqueous lithium-ion batteries.* Electrochemistry Communications, 2019. **104**: p. 106488.
11. Borodin, O., et al., *Uncharted Waters: Super-Concentrated Electrolytes.* Joule, 2020. **4**(1): p. 69-100.
12. Suo, L., et al., *How solid-electrolyte interphase forms in aqueous electrolytes.* J. Am. Chem. Soc., 2017. **139**(51): p. 18670-18680.
13. Dubouis, N., et al., *The role of the hydrogen evolution reaction in the solid–electrolyte interphase formation mechanism for "Water-in-Salt" electrolytes.* Energy & Environmental Science, 2018.
14. Ko, S., Y. Yamada, and A. Yamada, *Formation of a Solid Electrolyte Interphase in Hydrate-Melt Electrolytes.* ACS applied materials & interfaces, 2019. **11**(49): p. 45554-45560.
15. Reber, D., R.-S. Kühnel, and C. Battaglia, *High-voltage aqueous supercapacitors based on NaTFSI.* Sustainable Energy Fuels, 2017. **1**(10): p. 2155-2161.
16. Zheng, Q., et al., *Sodium-and potassium-hydrate melts containing asymmetric imide anions for high-voltage aqueous batteries.* Angewandte Chemie International Edition, 2019. **58**(40): p. 14202-14207.
17. Reber, D., et al., *Stability of aqueous electrolytes based on LiFSI and NaFSI.* Electrochimica Acta, 2019. **321**: p. 134644.
18. Hosseini-Bab-Anari, E., et al., *Fluorine-free salts for aqueous lithium-ion and sodium-ion battery electrolytes.* RSC Adv., 2016. **6**(88): p. 85194-85201.

19. Lukatskaya, M.R., et al., *Concentrated mixed cation acetate "water-in-salt" solutions as green and low-cost high voltage electrolytes for aqueous batteries.* Energy Environ. Sci., 2018. **11**(10): p. 2876-2883.

20. Qin, H., et al., *Aqueous rechargeable alkali-ion batteries with polyimide anode.* Journal of Power Sources, 2014. **249**: p. 367-372.

21. Leonard, D.P., et al., *Water-in-Salt Electrolyte for Potassium-Ion Batteries.* ACS Energy Lett., 2018. **3**(2): p. 373-374.

22. Guo, J., et al., *High-Performance and Ultra-Stable Aqueous Supercapacitors Based on a Green and Low-Cost Water-In-Salt Electrolyte.* ChemElectroChem, 2019. **6**(21): p. 5433-5438.

23. Nakamoto, K., et al., *Over 2 V Aqueous Sodium-Ion Battery with Prussian Blue-Type Electrodes.* Small Methods, 2019. **3**(4): p. 1800220.

24. Lee, M.H., et al., *Toward a low-cost high-voltage sodium aqueous rechargeable battery.* Materials Today, 2019. **29**: p. 26-36.

25. Qiu, S., et al., *NASICON-type Na3Fe2 (PO4) 3 as a low-cost and high-rate anode material for aqueous sodium-ion batteries.* Nano Energy, 2019. **64**: p. 103941.

26. Sharma, L., et al., *Na2FePO4F Fluorophosphate as Positive Insertion Material for Aqueous Sodium-Ion Batteries.* ChemElectroChem, 2019. **6**(2): p. 444-449.

27. Nakamoto, K., et al., *Electrolyte dependence of the performance of a Na2FeP2O7//NaTi2 (PO4) 3 rechargeable aqueous sodium-ion battery.* Journal of Power Sources, 2016. **327**: p. 327-332.

28. Zhang, H., et al., *Towards High-Performance Aqueous Sodium-Ion Batteries: Stabilizing the Solid/Liquid Interface for NASICON-Type Na2VTi (PO4) 3 using Concentrated Electrolytes.* ChemSusChem, 2018. **11**(8): p. 1382-1389.

29. Jiang, L., et al., *Building aqueous K-ion batteries for energy storage.* Nature Energy, 2019. **4**(6): p. 495-503.

30. Tomiyasu, H., et al., *An aqueous electrolyte of the widest potential window and its superior capability for capacitors.* Sci Rep, 2017. **7**: p. 45048.

31. Han, J., et al., *Fluorine-free water-in-salt electrolyte for green and low-cost aqueous sodium-ion batteries.* ChemSusChem, 2018. **11**(21): p. 3704-3707.

32. Chen, H., et al., *Use of a water-in-salt electrolyte to avoid organic material dissolution and enhance the kinetics of aqueous potassium ion batteries.* Sustainable Energy & Fuels, 2020. **4**(1): p. 128-131.

33. Nakamoto, K., et al., *Effect of concentrated electrolyte on aqueous sodium-ion battery with sodium manganese hexacyanoferrate cathode.* Electrochemistry, 2017. **85**(4): p. 179-185.

34. Liu, T., et al., *A promising water-in-salt electrolyte for aqueous based electrochemical energy storage cells with a wide potential window: highly concentrated HCOOK.* Chemical Communications, 2019. **55**(85): p. 12817-12820.

35. Liu, S., et al., *Na 3 V 2 (PO 4) 2 F 3–SWCNT: a high voltage cathode for non-aqueous and aqueous sodium-ion batteries.* Journal of Materials Chemistry A, 2019. **7**(1): p. 248-256.

36. Baowei, X., et al., *Cathode Properties of Na 3 FePO 4 CO 3 Prepared by the Mechanical Ball Milling Method for Na-ion Batteries.* Scientific Reports (Nature Publisher Group), 2020. **10**(1).

37. Han, S., *Anionic effects on the structure and dynamics of water in superconcentrated aqueous electrolytes.* RSC advances, 2019. **9**(2): p. 609-619.

38. Walrafen, G., *Raman spectral studies of water structure.* The Journal of Chemical Physics, 1964. **40**(11): p. 3249-3256.

39. Hofmeister, F., *Zur lehre von der wirkung der salze.* Archiv für experimentelle Pathologie und Pharmakologie, 1888. **25**(1): p. 1-30.

40. Cox, W. and J. Wolfenden, *The viscosity of strong electrolytes measured by a differential method.* Proceedings of the Royal Society of London. Series A, Containing Papers of a Mathematical and Physical Character, 1934. **145**(855): p. 475-488.

41. Marcus, Y., *Effect of ions on the structure of water: structure making and breaking.* Chem Rev, 2009. **109**(3): p. 1346-70.

42. Koga, Y., et al., *Toward understanding the Hofmeister series. 1. Effects of sodium salts of some anions on the molecular organization of H2O.* The Journal of Physical Chemistry A, 2004. **108**(40): p. 8533-8541.

43. Hribar, B., et al., *How ions affect the structure of water.* Journal of the American Chemical Society, 2002. **124**(41): p. 12302-12311.

44. Thomas, A.S. and A.H. Elcock, *Molecular dynamics simulations of hydrophobic associations in aqueous salt solutions indicate a connection between water hydrogen bonding and the Hofmeister effect.* Journal of the American Chemical Society, 2007. **129**(48): p. 14887-14898.

45. Kato, H., K. Nishikawa, and Y. Koga, *Relative hydrophobicity and hydrophilicity of some "Ionic liquid" Anions determined by the 1-propanol probing methodology: A differential thermodynamic approach.* The Journal of Physical Chemistry B, 2008. **112**(9): p. 2655-2660.

46. Morita, T., et al., *How much weaker are the effects of cations than those of anions? The effects of K+ and Cs+ on the molecular organization of liquid H2O.* The Journal of Physical Chemistry B, 2014. **118**(29): p. 8744-8749.

47. Hou, M., R. Lu, and A. Yu, *Polarizability series of aqueous polyatomic anions revealed by femtosecond Kerr effect spectroscopy.* RSC advances, 2014. **4**(44): p. 23078-23083.

48. Grossfield, A., P. Ren, and J.W. Ponder, *Ion solvation thermodynamics from simulation with a polarizable force field.* Journal of the American Chemical Society, 2003. **125**(50): p. 15671-15682.

49. Mazzini, V. and V.S. Craig, *What is the fundamental ion-specific series for anions and cations? Ion specificity in standard partial molar volumes of electrolytes and electrostriction in water and non-aqueous solvents.* Chemical science, 2017. **8**(10): p. 7052-7065.

50. Ball, P. and J.E. Hallsworth, *Water structure and chaotropicity: their uses, abuses and biological implications.* Physical Chemistry Chemical Physics, 2015. **17**(13): p. 8297-8305.

51. Jungwirth, P. and P.S. Cremer, *Beyond hofmeister.* Nature chemistry, 2014. **6**(4): p. 261-263.

52. Biffinger, J.C., H.W. Kim, and S.G. DiMagno, *The polar hydrophobicity of fluorinated compounds.* ChemBioChem, 2004. **5**(5): p. 622-627.

53. Murty, B.S., et al., *High-entropy alloys*. 2019: Elsevier.

54. Becker, M., R.-S. Kühnel, and C. Battaglia, *Water-in-salt electrolytes for aqueous lithium-ion batteries with liquidus temperatures below− 10° C.* Chemical Communications, 2019. **55**(80): p. 12032-12035.

55. Dubouis, N., et al., *Chasing Aqueous Biphasic Systems from simple salts by exploring the LiTFSI/LiCl/H2O phase diagram.* ACS central science, 2019. **5**(4): p. 640-643.

56. Navalpotro, P., et al., *Pioneering Use of Ionic Liquid-Based Aqueous Biphasic Systems as Membrane-Free Batteries.* Advanced Science, 2018. **5**(10): p. 1800576.

57. Chen, J., et al., *Improving Electrochemical Stability and Low-Temperature Performance with Water/Acetonitrile Hybrid Electrolytes.* Advanced Energy Materials, 2020. **10**(3): p. 1902654.

58. Jiang, P., et al., *Methylsulfonylmethane-Based Deep Eutectic Solvent as a New Type of Green Electrolyte for a High-Energy-Density Aqueous Lithium-Ion Battery.* ACS Energy Letters, 2019. **4**(6): p. 1419-1426.

59. McEldrew, M., et al., *Theory of Ion Aggregation and Gelation in Super-Concentrated Electrolytes.* arXiv preprint arXiv:2002.11825, 2020.

60. Song, J., et al., *Removal of interstitial H2O in hexacyanometallates for a superior cathode of a sodium-ion battery.* Journal of the American Chemical Society, 2015. **137**(7): p. 2658-2664.

61. Kiefer, J., J. Fries, and A. Leipertz, *Experimental vibrational study of imidazolium-based ionic liquids: Raman and infrared spectra of 1-ethyl-3-methylimidazolium bis (trifluoromethylsulfonyl) imide and 1-ethyl-3-methylimidazolium ethylsulfate.* Applied spectroscopy, 2007. **61**(12): p. 1306-1311.

9 A Perspective on the Electrochemical Stability of Water-in-Salt Electrolytes

Ruben-Simon Kühnel,[1] David Reber,[1,2] and Corsin Battaglia[1]

[1]Laboratory Materials for Energy Conversion, Swiss Federal Laboratories for Materials Science and Technology, Empa, Überlandstrasse 129, 8600 Dübendorf, Switzerland

[2]Institut des Matériaux, École Polytechnique Fédérale de Lausanne, EPFL, Station 12, 1015 Lausanne, Switzerland

Journal of The Electrochemical Society, 2020, 167, 070544

DOI: 10.1149/1945-7111/ab7c6f

https://iopscience.iop.org/article/10.1149/1945-7111/ab7c6f/pdf

In this invited perspective article we discuss the electrochemical stability of water-in-salt electrolytes. In literature we often find exaggerated stabilities and a disconnect between reported and practical electrochemical stability windows. Based on practical cells we discuss the issues in evaluating the stability window and provide guidance for future studies in the field. **Author contributions**: R.-S.K., D.R., C.B. conceived the idea for this study. D.R. and R.-S.K. designed the experiments. R.-S.K. calculated the examples given in the first part of the article. D.R. carried out the electrochemical experiments. D.R., R.-S.K., C.B. analyzed the data. R.-S.K and D.R. prepared the figures and wrote the original draft of the manuscript. R.-S.K. and C.B. critically reviewed and edited the manuscript. All coauthors read and approved the final manuscript.

Abstract

The water-in-salt approach has expanded the electrochemical stability window of aqueous electrolytes, enabling novel aqueous batteries with relatively high cell voltages and energy densities. However, the stability of these electrolytes tends to be overestimated. The instability of the electrolyte is typically masked by high rates and a large excess amount of electrolyte present in lab cells. Based on a discussion of practical cells, we revisit voltammetry data and offer guidelines for a more stringent evaluation of electrochemical stability window data.

9.1 Introduction

Water has many excellent properties as electrolyte solvent. It possesses a high dielectric constant, low viscosity, and is non-toxic, non-flammable, and inexpensive. However, its major drawback is its limited electrochemical stability window (ESW) of thermodynamically only 1.23 V at 25 °C. This has generally limited the voltage of aqueous batteries to ≤1.5 V with the exception of the lead-acid battery reaching 2.1 V when fully charged. Through a combination of bulk, interface, and interphase effects, highly concentrated aqueous solutions based on lithium perfluoroalkylsulfonylimide and related salts have wider ESWs than traditional aqueous electrolytes used in e.g. nickel-metal hydride or lead-acid batteries.[1-4] Molecular dynamics simulations indicate that particularly bis(trifluoromethanesulfonyl)imide (TFSI) anions accumulate at the electrode surface upon positive polarization, establishing a water-depletion zone that leads to higher oxidative stability of such electrolytes.[2] The increased reductive stability has been linked to the formation of a solid-electrolyte interphase on the anode side from decomposition of the lithium salt.[1, 3] In analogy to the solvent-in-salt approach,[5] these electrolytes are also called water-in-salt electrolytes as they contain more salt than water by weight and volume.[1]

The relatively wide ESW of water-in-salt electrolytes has enabled the development of novel, mostly intercalation-type, aqueous batteries with higher cell voltages than previously possible, narrowing the gap in voltage compared to cells based on organic electrolytes.[1, 6-9]

9.2 Current Status

The ESW of water-in-salt electrolytes such as 21 mol/kg (21m) LiTFSI has been reported to be as high as 3 V.[1, 7, 10] This has enabled stable cycling of high-voltage cathode materials such as $LiMn_2O_4$ and $Na_3(VOPO_4)_2F$ over several hundred cycles even at low charge/discharge rates.[1, 9, 11] In combination with anode protection strategies, e.g. carbon coatings or hydrophobic polymer coatings, stable cycling was also demonstrated with TiO_2, $Li_4Ti_5O_{12}$, $NaTi_2(PO_4)_3$, and even graphite anodes.[6, 8, 9, 12]

However, an increasing number of studies is proposing batteries and supercapacitors with increasingly higher cell voltages. In some cases, the cell voltage is obviously too high as in the case of >3 V supercapacitors.[13, 14] In other cases, stable cycling was achieved at high rates, but the low rate performance is not reported or relatively fast capacity fading is observed.[7, 10]

These high-voltage devices usually have in common a low active material mass loading (≤5 mg/cm^2) and a large amount of electrolyte (typically ~100 µL/cm^2 with respect to the electrode area). Together with the often-employed high rates of ≥5C, the stability of the electrolyte under more practical conditions is difficult to assess. When a cell is operated at high rates, the electrolyte is subjected to strongly reducing or oxidizing conditions for a much shorter time per cycle than at low rates. Hence, the current rate has a significant impact on the decomposition rate of the electrolyte per cycle. Realistic cells with high mass loadings (≥20 mg/cm^2) would potentially not be able to support such high rates due to transport limitations in the electrolyte. Finally, the onset of detrimental effects from water hydrolysis, e.g. salt precipitation or (local) pH change,[15, 16] can be delayed for a long time when using large amounts of electrolyte as the relative change in electrolyte composition is then small.

9.3 Future Needs

How much electrolyte would a realistic battery based on water-in-salt electrolytes contain? Considering that the lithium-ion conductivity of typical water-in-salt electrolytes at room temperature is on the order of 1-7 mS/cm,[7, 17] i.e. comparable to that of carbonate-based organic electrolytes,[18] the distance between current collectors composed of the thickness of anode, separator, and cathode should be similar to that in commercial lithium-ion batteries. **Figure 9-1a** shows the evolution of the overpotential stemming from the electrolyte resistance with increasing distance between current collectors for three hypothetical cells. The assumptions here are a lithium-ion conductivity of 3 mS/cm at room temperature and of 0.1 mS/cm for the low temperature scenario. For the high-energy and high-power batteries, we consider areal capacities and current rates of 5 and 2 mAh/cm^2 and C/5 and 10C, respectively.

For these three scenarios, Ohmic losses are negligible up to the considered maximum distance between current collectors (neglecting electrode tortuosity) of 1 mm for the high-energy battery operated at room temperature. For the other two scenarios, Ohmic losses stemming from the electrolyte already exceed 100 mV for a distance of 100 and 150 µm, respectively. Such an overpotential results in a loss in energy efficiency of 9.5% for a hypothetical cell with an average voltage of 2.0 V (see **Figure 9-1b**).[19] Hence, the electrode distance of practical cells based on water-in-salt electrolytes should be limited to enable high energy efficiency. This is in contrast to lead-acid batteries, whose sulfuric acid electrolyte has a room temperature conductivity that is three orders of magnitudes higher,[20] enabling larger electrode distance and thickness. Another argument for limiting the electrode distance in water-in-salt electrolyte-based cells, and hence the amount of electrolyte, is the high cost of most water-in-salt electrolytes that stems from the high price and concentration of the employed salts.

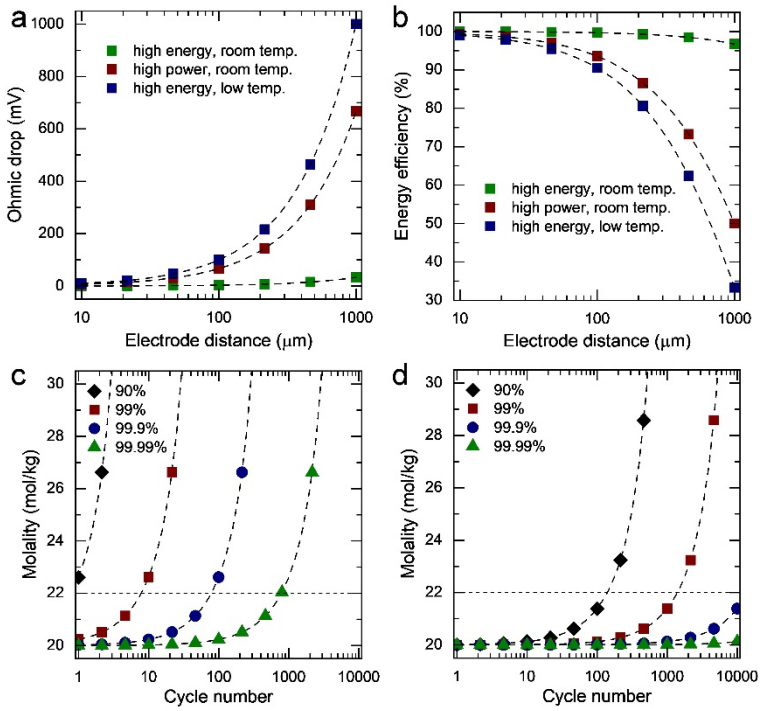

Figure 9-1 (a) Calculated dependence of the overpotential stemming from the bulk resistance of the electrolyte (Ohmic drop) on the electrode distance for three hypothetical cell scenarios. The assumptions are a conductivity of 3 mS/cm at room temperature (room temp.) and of 0.1 mS/cm at low temperature (low temp.). For the high-energy and high-power cells, areal capacities and current rates of 5 and 2 mAh/cm² and C/5 and 10C were considered, respectively. (b) The resulting effect of the Ohmic drop on the energy efficiency of a hypothetical 2.0 V cell. (c, d) Calculated change of the electrolyte concentration with cycle number for (c) a realistic cell and (d) a typical lab cell. The calculation was carried out for Coulombic efficiencies of 90%, 99%, 99.9%, and 99.99%. For the realistic cell and lab cell, areal capacities of 5 and 0.5 mAh/cm² were considered, respectively. The only other difference between the two cells is the amount of electrolyte: 5.6 µL/cm² for the realistic cell (based on 2x 100 µm thick electrodes with a porosity of 25% and a 15 µm thick separator with a porosity of 40%) and 100 µL/cm² for the lab cell. 20m LiTFSI was chosen as (initial) electrolyte. The dashed horizontal line in (c) and (d) marks the onset concentration for crystallization of 22 mol/kg considered for the discussion.

As water-in-salt electrolytes are typically operated near the solubility limit of the salt or salt combination, water loss can lead to salt crystallization in the cell.[9] Crystallization can lead to pore clogging, capacity loss, and an increase in cell resistance.[9, 15] **Figure 9-1c, d** compares the change in electrolyte concentration with cycle number for a realistic high-energy cell as established above and a typical lab cell under the assumption that the irreversible capacity is solely due to water hydrolysis.

For the realistic cell, we assume an areal capacity of 5 mAh/cm^2 and for the lab cell 0.5 mAh/cm^2. The only other difference between the two cells is the amount of electrolyte: 5.6 µL/cm^2 for the realistic cell (derived from 2x 100 µm thick electrodes with a porosity of 25% and a 15 µm thick separator with a porosity of 40%) and 100 µL/cm^2 for the lab cell. The value of 5.6 µL/cm^2 for a cell with a capacity of 5 mAh/cm^2 corresponds well to the range of 1.3 to 1.5 grams of electrolyte per Ampere hour of cell capacity reported in literature for commercial lithium-ion batteries, considering the higher density of water-in-salt electrolytes (our assumption in this study: 1.75 g/cm^3) compared to that of commercial liquid organic electrolytes (~1.3 g/cm^3): 5.6 µL/cm^2 x 1.75 g/cm^3 / 5 mAh/cm^2 = 1.96 g/Ah.[21, 22] In the example, we

consider a 20m LiTFSI solution as (initial) electrolyte. If the Coulombic efficiency is only ~90%, as is sometimes the case for slowly-cycled water-in-salt electrolyte-based cells reported in literature,[7, 10] the electrolyte concentration of a realistic cell rapidly increases and exceeds the assumed solubility limit of 22m after less than 1 cycle. Only cells displaying a Coulombic efficiency of ≥99.99% can be cycled for more than 500 cycles. In contrast, the lab cell can be cycled for more than 100 cycles even if the Coulombic efficiency is as low as 90 %. Hence, excess electrolyte clearly acts as cycle-life booster. This calculation ignores other detrimental effects of water hydrolysis such as local pH changes that can lead to active material degradation and current collector corrosion.[16, 23]

While the present study focuses on the electrochemical stability of the electrolyte and its effect on cycle life and energy efficiency, a comprehensive evaluation of new cell components in terms of all relevant performance metrics is desirable to assess their practical relevance.[24, 25] For example, the gravimetric energy density of batteries based on highly concentrated electrolytes is slightly lower, all else being equal, due to the higher density of such electrolytes compared to traditional more dilute electrolytes (e.g., 1M $LiPF_6$ in ethylene carbonate:dimethyl carbonate 1:1 (by weight) has a density of 1.30 g/cm^3 at 24 °C, whereas 27.8m $Li(TFSI)_{0.7}(LiBETI)_{0.3}$ has a density of 1.78 g/cm^3 at 25 °C)[7, 22].

Considering that practical cells based on water-in-salt electrolytes require Coulombic efficiencies of ≥99.9% at low rates to enable sufficient cycle life, rather strict criteria have to be used when determining the ESW of water-in-salt electrolytes to avoid a mismatch between reported ESW and cycling stability under realistic conditions. For this purpose, we revisited electrochemical stability data for the archetypical H_2O–LiTFSI system. The ESW of electrolytes is most commonly determined via voltammetry experiments using (inert) metal working electrodes.[18] A common criterion for the determination of the ESW from voltammetry data is a cut-off current density.[26] However, most water-in-salt electrolyte studies state a (wide) ESW without mentioning the criterion used to analyze the voltammetry data that the reported ESW is based on.

To study the effect of cut-off current density on the apparent ESW, we recorded voltammograms of aqueous LiTFSI solutions at a scan rate of 0.1 mV/s using stainless steel and gold working electrodes for the reductive and oxidative stability, respectively (**Figure 9-2a**). All measurements were carried out in three-electrode Swagelok cells with a Bio-Logic VMP3 electrochemical workstation. Activated carbon-based pellets were used as counter electrode, a miniature Ag/AgCl electrode (eDAQ) was used as reference electrode, and a Whatman type GF/D glass microfiber filter drenched with 150 µL of electrolyte was used as separator. 12 mm disks of stainless steel (grade 1.4310, Brütsch/Rüegger Werkzeuge AG) or a 1 mm gold disk electrode from eDAQ were used as reference electrode, respectively.

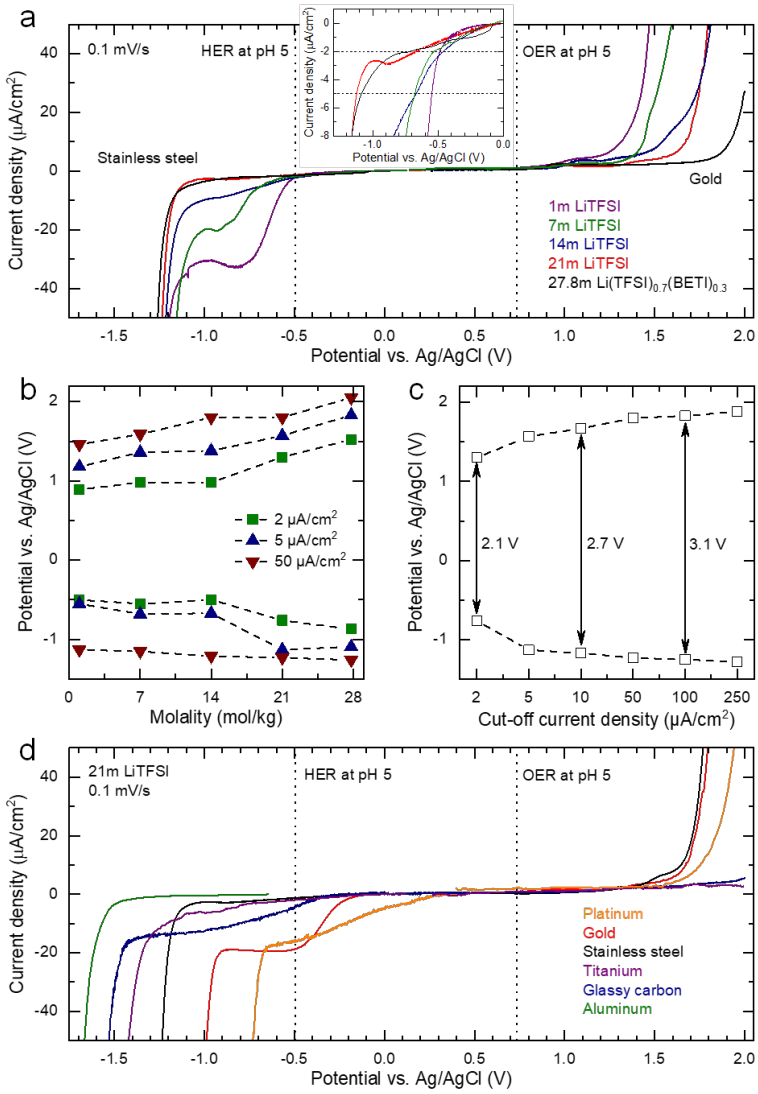

Figure 9-2 Electrochemical stability windows of degassed aqueous LiTFSI solutions of various concentrations. (a) Linear sweep voltammograms on stainless steel (for the reductive stability) and gold (for the oxidative stability), respectively. The thermodynamic onsets of the hydrogen and oxygen evolution reactions for a pH of 5 are shown as dashed vertical lines. The inset is a magnification of the low-current region of the cathodic scan. (b) Stability limits of the electrolytes as determined by applying three different threshold current densities to the voltammetry data shown in (a). (c) Stability window of 21m LiTFSI as a function of cut-off current density. (d) Linear sweep voltammograms for 21m LiTFSI on platinum, gold, stainless steel (SS), titanium, glassy carbon (GC), and aluminum. The pH of all solutions was adjusted to a value of ~5. All experiments were carried out at room temperature at a scan rate of 0.1 mV/s.

We then determined the cathodic and anodic stability limits for different LiTFSI concentrations using different cut-off current densities (see **Figure 9-2b**). For a cut-off current density of 50 µA/cm^2, which corresponds to the nearly vertical parts of the current density–potential curves, we obtain an unrealistically wide ESW of 2.6 V already for the lowest concentration of 1m. Hence, this criterion is clearly too loose. A much smaller cut-off current density of 2 µA/cm^2 results in more realistic ESWs of 1.4-1.5 V for the 1m, 7m, and 14m LiTFSI concentrations. For the 21m LiTFSI solution, we obtain an ESW of 2.1 V, while for the 27.8m Li(TFSI)$_{0.7}$(LiBETI)$_{0.3}$ (LiBETI = lithium bis(pentafluoroethanesulfonyl)imide) solution an ESW of 2.4 V is obtained.[7]

Figure 9-2c shows the evolution of the apparent ESW of 21m LiTFSI with increasing cut-off current density. Using a threshold of 100 µA/cm^2, our results confirm the reported ESW of 3 V. When lowering the cut-off from 100 to 5 µA/cm^2, the ESW slowly decreases from 3.1 to 2.7 V, while it drops to 2.1 V for a limit of 2 µA/cm^2. Tying this current density back to a Coulombic efficiency target of e.g. ≥99.9% is not straightforward as the measured current density of such a voltammetry experiment depends on the scan rate, type of working electrode, and to a certain extent the geometry of the employed cell. For a cell with an areal capacity of 5 mAh/cm^2 operated at a current rate of C/5, a Coulombic efficiency of 99.9% corresponds to an average irreversible current density of 1 µA/cm^2. As many applications involve keeping the battery at a state-of-charge of at least 50% and as even a Coulombic efficiency of 99.9% does not enable hundreds of cycles, a lower current density for water decomposition of <1 µA/cm^2 appears desirable, if refilling is no option. Nevertheless, the water-in-salt approach clearly improves the electrochemical stability of aqueous electrolytes. In particular, the oxidative stability of neutral-pH water-in-salt electrolytes appears to be (at least) on par with that of conventional carbonate-based electrolytes as demonstrated by the above-cited excellent cycling stability of several high-voltage cathode materials. These results are even more impressive considering that the onset of the oxygen evolution reaction shifts by 59 mV per pH unit to more negative potentials when increasing the pH from ≤0 (e.g. sulfuric acid used in lead-acid batteries) to the usually near-neutral pH of water-in-salt electrolytes. In addition, lithium-ion insertion/intercalation potentials are shifted by ≥200 mV to more positive potentials in water-in-salt electrolytes, further increasing the required oxidative stability.[1, 7]

For the cathodic scan, several studies suggest that the measured current density is the sum of several competing processes: hydrogen evolution reaction (HER), reduction of dissolved gases, and electrochemical anion reduction.[1, 3, 7] There is growing evidence that the latter process leads to the formation of a solid-electrolyte interphase (SEI) that consequently limits the HER.[3, 7] Recently, a different mechanism regarding the SEI formation process in water-in-salt electrolytes was proposed: According to this study, anion reduction is rather the result of nucleophilic attack by hydroxide anions that form as a byproduct of the HER.[4] More work is needed to better understand the formation process and effectiveness of the SEI forming in water-in-salt electrolytes.

The measured current densities are also highly dependent on the catalytic activity of the electrode material, as illustrated in **Figure 9-2d**. We observe significantly different current densities on platinum (1 mm disk electrode, eDAQ), gold, stainless steel, titanium (12 mm disk, >99.6%, Goodfellow), glassy carbon (1 mm disk electrode, eDAQ), and aluminum (12 mm disk, >99.3%, MTI). The differences in cathodic stability towards water reduction follow the reported trends for the catalytic activity of these materials.[27] For the anodic scan, the current

density decreases in the order stainless steel ≈ gold > platinum > glassy carbon > titanium. Comparable differences in current density between different working electrode materials were also reported in literature.[7, 28]

Finally, quantification of electrolyte oxidation and reduction products resulting from the competition of different processes on the anode (hydrogen evolution, reduction of dissolved gases, anion reduction) and cathode side (oxygen evolution, current collector corrosion, and potentially anion oxidation) provide valuable additional insights, especially if conducted using composite battery electrodes as working electrodes. In particular, gas evolution studies are needed to demonstrate the real practicality of batteries based on water-in-salt electrolytes. A first such study was published recently.[3]

9.4 Conclusions

The water-in-salt approach has enabled aqueous batteries and supercapacitors with significantly larger cell voltages. However, as shown above, the ESW can easily differ by 1-1.5 V depending on the cut-off current density that is chosen for evaluating the voltammetry data. This sensitivity to the cut-off criterion has contributed to the disconnect between reported ESWs and reported cycling stability/Coulombic efficiency of batteries and supercapacitors incorporating water-in-salt electrolytes. In addition, the ESW of water-in-salt electrolytes strongly depends on the electrode material, as the high stability is a result of kinetic stabilizations that depend on the electrocatalytic properties of the electrode material. To give a more application-relevant assessment of the ESW of water-in-salt electrolytes, more stringent criteria should be used when extracting ESWs from voltammetry data. Ideally, the electrodes chosen for the ESW experiments would have similar electrocatalytic properties as the electrodes of the target device. In addition, all relevant experimental details such as cell type, electrode material, mass loading (if applicable), scan rate, and cut-off current density/data analysis method should be provided to allow assessment and comparison of ESW data from voltammetry.

Finally, more realistic cell tests using small amounts of electrolyte, high mass loadings, and low current rates are highly desirable. Such cells should also be subjected to constant voltage at various states-of-charge and to different temperatures to study their stability under various real-life conditions.

References

1. Suo, L., et al., *"Water-in-salt" electrolyte enables high-voltage aqueous lithium-ion chemistries.* Science, 2015. **350**(6263): p. 938-43.
2. Vatamanu, J. and O. Borodin, *Ramifications of water-in-salt interfacial structure at charged electrodes for electrolyte electrochemical stability.* J. Phys. Chem. Lett., 2017. **8**(18): p. 4362-4367.
3. Suo, L., et al., *How solid-electrolyte interphase forms in aqueous electrolytes.* J. Am. Chem. Soc., 2017. **139**(51): p. 18670-18680.
4. Dubouis, N., et al., *The role of the hydrogen evolution reaction in the solid–electrolyte interphase formation mechanism for "Water-in-Salt" electrolytes.* Energy & Environmental Science, 2018. **11**(12): p. 3491-3499.
5. Suo, L., et al., *A new class of Solvent-in-Salt electrolyte for high-energy rechargeable metallic lithium batteries.* Nat. Commun., 2013. **4**(1): p. 1481.
6. Suo, L., et al., *Advanced High-Voltage Aqueous Lithium-Ion Battery Enabled by "Water-in-Bisalt" Electrolyte.* Angew. Chem. Int. Ed., 2016. **55**(25): p. 7136-7141.
7. Yamada, Y., et al., *Hydrate-melt electrolytes for high-energy-density aqueous batteries.* Nat. Energy, 2016. **1**: p. 16129.
8. Yang, C., et al., *4.0 V Aqueous Li-Ion Batteries.* Joule, 2017. **1**(1): p. 122-132.
9. Reber, D., R.-S. Kühnel, and C. Battaglia, *Suppressing Crystallization of Water-in-Salt Electrolytes by Asymmetric Anions Enables Low-Temperature Operation of High-Voltage Aqueous Batteries.* ACS Mater. Lett., 2019. **1**: p. 44-51.
10. Wang, F., et al., *Spinel $LiNi_{0.5}Mn_{1.5}O_4$ Cathode for High-Energy Aqueous Lithium-Ion Batteries.* Adv. Energy Mater., 2017. **7**(8): p. 1600922.
11. Wang, F., et al., *Stabilizing high voltage $LiCoO_2$ cathode in aqueous electrolyte with interphase-forming additive.* Energy Environ. Sci., 2016. **9**(12): p. 3666-3673.
12. Ko, S., et al., *Lithium-salt monohydrate melt: A stable electrolyte for aqueous lithium-ion batteries.* Electrochem. Commun., 2019. **104**: p. 106488.
13. Tomiyasu, H., et al., *An aqueous electrolyte of the widest potential window and its superior capability for capacitors.* Sci. Rep., 2017. **7**(1): p. 45048.
14. Liu, T., et al., *A promising water-in-salt electrolyte for aqueous based electrochemical energy storage cells with a wide potential window: highly concentrated HCOOK.* Chem. Commun., 2019. **55**(85): p. 12817-12820.
15. Becker, M., R.-S. Kühnel, and C. Battaglia, *Water-in-salt electrolytes for aqueous lithium-ion batteries with liquidus temperatures below −10 °C.* Chem. Commun., 2019. **55**(80): p. 12032-12035.
16. Mohamed, A.I. and J.F. Whitacre, *Capacity Fade of $NaTi_2(PO_4)_3$ in Aqueous Electrolyte Solutions: Relating pH Increases to Long Term Stability.* Electrochim. Acta, 2017. **235**: p. 730-739.
17. Borodin, O., et al., *Liquid structure with nano-heterogeneity promotes cationic transport in concentrated electrolytes.* ACS Nano, 2017. **11**(10): p. 10462-10471.
18. Xu, K., *Nonaqueous Liquid Electrolytes for Lithium-Based Rechargeable Batteries.* Chem. Rev., 2004. **104**(10): p. 4303-4418.

19. Meister, P., et al., *Best Practice: Performance and Cost Evaluation of Lithium Ion Battery Active Materials with Special Emphasis on Energy Efficiency.* Chem. Mater., 2016. **28**(20): p. 7203-7217.

20. Darling, H.E., *Conductivity of Sulfuric Acid Solutions.* J. Chem. Eng. Data, 1964. **9**(3): p. 421-426.

21. Liu, J., et al., *Pathways for practical high-energy long-cycling lithium metal batteries.* Nat. Energy, 2019. **4**(3): p. 180-186.

22. Fröhlich, K., et al., *Electrochemical Investigation of Thermodynamic and Transport Phenomena in LP30 Electrolyte with Various Concentrations of Conducting Salt.* ECS Trans., 2016. **73**(1): p. 83-93.

23. Wojciechowski, J., et al., *The influence of current collector corrosion on the performance of electrochemical capacitors.* Journal of Power Sources, 2017. **368**: p. 18-29.

24. Lin, Z., et al., *Aligning academia and industry for unified battery performance metrics.* Nat. Commun., 2018. **9**(1): p. 5262.

25. Betz, J., et al., *Theoretical versus Practical Energy: A Plea for More Transparency in the Energy Calculation of Different Rechargeable Battery Systems.* Adv. Energy Mater., 2019. **9**(6): p. 1803170.

26. Mousavi, M.P.S., et al., *Unbiased Quantification of the Electrochemical Stability Limits of Electrolytes and Ionic Liquids.* J. Electrochem. Soc., 2015. **162**(12): p. A2250-A2258.

27. Roger, I., M.A. Shipman, and M.D. Symes, *Earth-abundant catalysts for electrochemical and photoelectrochemical water splitting.* Nat. Rev. Chem., 2017. **1**(1): p. 0003.

28. Coustan, L., G. Shul, and D. Bélanger, *Electrochemical behavior of platinum, gold and glassy carbon electrodes in water-in-salt electrolyte.* Electrochem. Commun., 2017. **77**: p. 89-92.

10 Conclusion and Outlook

Large-scale batteries are becoming a key component of the energy transition, enabling widespread integration of renewables into the grid. However, state-of-the art lithium-ion batteries suffer from supply chain risks and safety issues due to the use of flammable organic electrolytes and reactive salts. Aqueous electrolytes are a promising alternative as they are inherently non-flammable, but due to their narrow electrochemical stability window did not deliver adequate energy density so far. At the start of this project, two major publications described the improved electrochemical stability of highly concentrated electrolytes, demonstrating aqueous lithium-ion batteries with unprecedented energy densities.[1, 2] This spurred renewed interest in aqueous batteries and motivated this thesis.

In this work, we studied highly concentrated aqueous electrolytes and evaluated their potential for application in sodium-ion batteries. We expanded the concept of so-called water-in-salt electrolytes to post-lithium chemistries and recognized salt solubility as a major limiting factor. Screening for highly soluble sodium salts, we developed the first sodium water-in-salt electrolyte based on NaFSI, almost doubling the electrochemical stability window compared to dilute solutions. We describe improved chemical stability of such electrolytes compared to their lithium analogues and find that the FSI anions susceptibility towards hydrolysis is highly cation- and concentration-dependent, making NaFSI electrolytes suitable model systems.

Water-in-salt electrolytes being nearly saturated salt solutions, we demonstrate crystallization at or below room temperature to be a crucial issue limiting the practicality of such electrolytes. Partially replacing FSI with asymmetric FTFSI anions, we demonstrated suppressed crystallization at temperatures as low as -10 °C, enabling stable cycling of a 2 V class aqueous sodium-ion battery over an unprecedented temperature range. We identified unique cation-anion coordination geometries and subsequent slow rotational relaxation of intramolecular bond rotations in FTFSI to disturb dense ion packing, thus enhancing the supercooling behavior of concentrated FTFSI based electrolytes.

With FSI and FTFSI only being model systems due to hydrolysis, and alternative sodium salts having too low solubility limits, we systematically studied the influence of the anion on solution structure, electrochemical stability, and cell performance in aqueous batteries. We develop suitability criteria for anions in water-in-salt electrolytes, establish minimum concentration limits for sodium-ion batteries, and provide guidelines for future work. Linked to the unsuitability of certain anions, we provide a perspective on the electrochemical stability of water-in-salt electrolytes and discuss the disconnect between reported and practical values.

The main contributions of this thesis to the field of aqueous batteries can be summarized as follows:

- We develop sodium water-in-salt model systems, enabling stable cycling of some of the highest-voltage sodium cathode materials in aqueous electrolytes
- We scrutinize measuring the electrochemical stability window of aqueous electrolytes and point out that it is often overestimated in literature
- We recognize crystallization of highly concentrated electrolytes as a crucial challenge that limits their applicability
- We find that local dynamics of asymmetric anions can influence macroscopic properties like supercooling and thereby suppress crystallization in water-in-salt electrolytes
- We describe strong anion-specific effects observed in concentrated electrolytes and derive guidelines for choosing suitable anions for water-in-salt applications
- We conclude that for suitable sodium salts and combinations thereof no high enough concentration can be achieved to enable desired electrochemical stability

Clearly, not all challenges for aqueous batteries have been resolved. The need for better sodium cathodes is evident and the gap towards lower voltage anodes, sometimes called the cathodic challenge[3], remains large: The oxidative stability of aqueous electrolytes was improved to high levels, enabling stable cycling of high-voltage cathodes. However, the reductive stability of concentrated aqueous electrolytes is still rather poor compared to their organic counterparts, allowing cycling of low-voltage anodes like lithium metal or graphite only with elaborate electrode coatings.[3-5] Furthermore, the ionic conductivity of some of the best performing aqueous electrolytes with concentrations above 55m has decreased to less than 1 mS cm^{-1}, limiting their rate capability.[6, 7]

We pointed out crucial factors like anion hydrolysis, which was rapidly taken up by the community by using the chemically more stable and still asymmetric PTFSI anion.[7-9] In addition we discussed electrolyte crystallization, and anion-specific effects, concepts that are valid beyond lithium- or sodium-ion batteries. For aqueous sodium-ion batteries in particular, we conclude that due to solubility limits, concepts other than dissolving large amounts of salt are needed. Promising approaches include the addition of organic co-solvents to water-in-salt electrolytes, which improves SEI stability on the anode while maintaining the non-flammability of aqueous electrolytes[10], using mixed cation systems, e.g. the addition of ionic liquids to water-in-salt electrolytes,[6, 11] or the development of new anions such as pseudo-delocalized sulfonate-amines.[12] Alternatively, or rather additionally, protective coatings and artificial solid-electrolyte interphases seem very promising concepts for upcoming studies.[3, 5]

References

1. Suo, L., et al., *"Water-in-salt" electrolyte enables high-voltage aqueous lithium-ion chemistries.* Science, 2015. **350**(6263): p. 938-43.
2. Yamada, Y., et al., *Hydrate-melt electrolytes for high-energy-density aqueous batteries.* Nat. Energy, 2016. **1**: p. 16129.
3. Yang, C., et al., *4.0 V Aqueous Li-Ion Batteries.* Joule, 2017. **1**(1): p. 122-132.
4. Borodin, O., et al., *Uncharted Waters: Super-Concentrated Electrolytes.* Joule, 2020. **4**(1): p. 69-100.
5. Yang, C., et al., *Aqueous Li-ion battery enabled by halogen conversion–intercalation chemistry in graphite.* Nature, 2019. **569**(7755): p. 245-250.
6. Chen, L., et al., *A 63 m Super-concentrated Aqueous Electrolyte for High Energy Li-ion Batteries.* ACS Energy Letters, 2020.
7. Ko, S., et al., *Lithium-salt monohydrate melt: A stable electrolyte for aqueous lithium-ion batteries.* Electrochemistry Communications, 2019. **104**: p. 106488.
8. Zheng, Q., et al., *Sodium-and potassium-hydrate melts containing asymmetric imide anions for high-voltage aqueous batteries.* Angewandte Chemie International Edition, 2019. **58**(40): p. 14202-14207.
9. Becker, M., R.-S. Kühnel, and C. Battaglia, *Water-in-salt electrolytes for aqueous lithium-ion batteries with liquidus temperatures below −10 °C.* Chem. Commun., 2019. **55**(80): p. 12032-12035.
10. Chen, J., et al., *Improving Electrochemical Stability and Low-Temperature Performance with Water/Acetonitrile Hybrid Electrolytes.* Advanced Energy Materials, 2020. **10**(3): p. 1902654.
11. Jiang, L., et al., *High-Voltage Aqueous Na-Ion Battery Enabled by Inert-Cation-Assisted Water-in-Salt Electrolyte.* Advanced Materials, 2019: p. 1904427.
12. Forero-Saboya, J., et al., *Water-in-Bisalt Electrolyte with Record Salt Concentration and Widened Electrochemical Stability Window.* The journal of physical chemistry letters, 2019. **10**(17): p. 4942-4946.

List of Figures

List of Tables

Curriculum vitae

David **Reber**

Chemist ▪ PhD Student in Materials Science and Engineering ▪ Swiss Nationality

(+41) 79 832 0209 | dreberp@gmail.com | Freiestrasse 63, 8406 Winterthur

Work Experience

Empa – Swiss Federal Laboratories for Materials Science and Technology — Zürich, CH

Research scientist – Development of aqueous electrolytes for high-voltage batteries — *Sept. 2016 - present*

- First author of five publications, four as second author
- Responsible for electrode coating and electrochemistry laboratories
- Supervision of bachelor and master theses

University of Tokyo — Tokyo, JP

Visiting researcher – Molecular dynamics simulation of aqueous electrolytes — *Mar. – Jun. 2019*

- Grant by the young researchers' exchange program between Japan and Switzerland

medi | Zentrum für medizinische Bildung — Bern, CH

Lecturer – Chemistry, Biochemistry, and Safety & Hygiene — *2012 - 2016*

- 6 lessons per week on the level of a College of Professional Education and Training
- Development of teaching script and lectures

University of Bern — Bern, CH

Junior researcher – Various organic synthesis projects — *Aug. – Dec. 2013*

Education

PhD in Materials Science and Engineering – EPFL Lausanne — Zürich, CH

Thesis conducted at Empa, supervised by Dr. Corsin Battaglia and Prof. Frank Nüesch. — *Sept. 2016 – Jun. 2020*

MSc in Chemistry and Molecular Sciences – University of Bern — Bern, CH

Summa Cum Laude. Thesis supervised by Prof. Peter Broekmann and Prof. Wenjing Hong — *2016*

BSc in Chemistry and Molecular Sciences – University of Bern — Bern, CH

Magna Cum Laude. Thesis supervised by Prof. Silvio Decurtins and Dr. Shi-Xia Liu — *2013*

Skills and Expertise

Characterization methods

- Electrochemical characterization of battery materials and cells (galvanostatic and voltammetric methods, impedance spectroscopy)
- Structural characterization using X-ray diffraction, Raman spectroscopy, and scanning electron microscopy
- Thermal characterization by thermogravimetric analysis and differential scanning calorimetry
- Molecular dynamics simulation of liquid electrolytes
- Electrochemical scanning tunneling microscopy on gold and HOPG

Materials preparation

- Synthesis of battery electrode materials (solid state, co-precipitation, hydrothermal, microwave)
- Aqueous and organic battery electrode processing (tape casting, calendering)
- Aqueous and organic electrolyte battery assembly (Swagelok, coin cells, three-electrode)
- Ion exchange chromatography

Informatics — MS Office, Origin, CorelDraw, EC-Lab, MT-Lab, APT-COM, AmberTools16, VMD, Gaussian9, Dreamweaver

Languages — German (native), English (full professional proficiency), French (limited working proficiency), Spanish (elementary proficiency)

Miscellaneous — Designer (founder) for a small climbing specific apparel brand

Awards and Achievements

Young researchers' exchange program between Japan and Switzerland (2019), JSPS-fellowship for a three month stay at the University of Tokyo hosted by Prof. Atsuo Yamada

Selected to represent Switzerland at the Global Young Scientists Summit in Singapore (2019), presenting my work and learning from Nobel Laureates

Winner of the Falling Walls Lab Zürich, selected to represent Switzerland at the global finale in Berlin (2018), presenting a three minute pitch about my work: http://tinyurl.com/david-reber

MDPI Technologies Travel Award (2018), contribution to my participation at the 233rd ECS meeting

5x best poster award, at various conferences (2017-2019)

Selected Publications

Anion Chaotropicity as Indicator for Water-in-Salt Electrolyte Stability
Reber, D., Kühnel, R.-S., Battaglia, C., submitted

Impact of anion asymmetry on local structure and supercooling behavior of water-in-salt electrolytes
Reber, D., Takenaka, N., Kühnel, R.-S., Yamada, A., Battaglia, C., *J. Phys. Chem. Lett.* **2020**, 11, 4720

A perspective on highly-concentrated aqueous electrolytes
Kühnel, R.-S. *, Reber, D.*, Battaglia, C., *J. Electrochem. Soc.* **2020**, 167, 070544

Suppressing crystallization of water-in-salt electrolytes by asymmetric anions enables low temperature operation of high-voltage aqueous batteries
Reber, D., Kühnel, R.-S., Battaglia, C., *ACS Materials Lett.* **2019**, 1, 44

Stability of aqueous electrolytes based on LiFSI and NaFSI
Reber, D., Figi, R., Kühnel, R.-S., Battaglia, C., *Electrochim. Acta* **2019**, 321, 134644

High-voltage aqueous supercapacitors based on NaTFSI
Reber, D., Kühnel, R.-S., Battaglia, C., *Sust. Energy Fuels* **2017**, 1, 2155

A high-voltage aqueous electrolyte for sodium-ion batteries
Kühnel, R.-S., Reber, D., Battaglia, C., *ACS Energy Lett.* **2017**, 2, 2005

Gating of Quantum Interference in Molecular Junctions by Heteroatom Substitution
Liu, X.*, Sangtarash, S.*, Reber, D.*, Zhang, D.*, Sadeghi, H., Shi, J., Xiao, Z. Y., Hong, W., Lambert, C. J., Liu, S.-X., *Angew. Chem. Int. Ed.* **2017**, 56, 173

"Water-in-salt" electrolytes enable the use of cost-effective aluminium current collectors for aqueous high-voltage batteries
Kühnel, R.-S., Reber, D., Remhof, A., Figi, R., Bleiner, D., Battaglia, C., *Chem. Commun.* **2016**, 52, 10435

Controlling Electrical Conductance through a π-Conjugated Cruciform Molecule by Selective Anchoring to Gold Electrodes
Huang, C., Chen, S., Baruël Ørnsø, K., Reber, D., Baghernejad, M., Fu, Y., Wandlowski, T., Decurtins, S., Hong, W., Sommer Thygesen, K., Liu, S.-X., *Angew. Chem. Int. Ed.* **2015**. 54, 14304-14307

Selected Presentations

Materials Research Society Fall Meeting (MRS) — Boston, MA, USA
Oral and poster presentations — *December 2019*

Electrochemical Conference on Energy and the Environment (ECS) — Glasgow, SCT, UK
Oral and poster presentations — *July 2019*

1st & 2nd Swiss & Surrounding Battery Days — Baden/Zürich, CH
Oral and poster presentations — *May 2018/August 2019*

233rd Electrochemical Society Meeting (ECS) — Seattle, WA, USA
Oral and poster presentations — *May 2018*

5th International Symposium on Enhanced Electrochemical Capacitors — Jena, DE
Poster presentation — *July 2017*

Personal Interests

Snowboarding, Rock climbing, Surfing, Design, Drums, Pyrotechnics